

Retinal Imaging: Acquisition, Processing, and Application of Mueller Matrix Confocal Scanning Laser Polarimetry

by

Christopher James Cookson

A thesis

presented to the University of Waterloo

in fulfilment of the

thesis requirement for the degree of

Master of Science

in

Vision Science

Waterloo, Ontario, Canada, 2013

© Christopher James Cookson 2013

Author's Declaration

I hereby declare that I am the sole author of this thesis except where otherwise noted. This is a true copy of the thesis, including any required final revisions, as accepted by my examiners. I understand that my thesis may be made electronically available to the public.

Abstract

The focus of this thesis is the improvement of acquisition and processing of Mueller matrix polarimetry using a confocal scanning laser ophthalmoscope (CSLO) and the application of Mueller matrix polarimetry to image the retina. Stepper motors were incorporated into a CSLO to semi-automate Mueller matrix polarimetry and were used in retinal image acquisition. Success rates of Fourier transform based edge detection filters, designed to improve the registration of retinal images, were compared. The acquired polarimetry images were used to reassess 2 image quality enhancement techniques, Mueller matrix reconstruction (MMR) and Stokes vector reconstruction (SVR), focusing on the role of auto-contrasting or normalization within the techniques and the degree to which auto-contrasting or normalization is responsible for image quality improvement of the resulting images. Mueller matrix polarimetry was also applied to find the retardance image of a malaria infected retinal blood vessel imaged in a confocal scanning laser microscope (CSLM) to visualize hemozoin within the vessel. Image quality enhancement techniques were also applied and image quality improvement was quantified for this blood vessel.

The semi-automation of Mueller matrix polarimetry yielded a significant reduction in experimental acquisition time (80%) and a non-significant reduction in registration time (44%). A larger sample size would give higher power and this result might become significant. The reduction in registration time was most likely due to less movement of the eye, particularly in terms of decreased rotation seen between registered images. Fourier transform edge detection methods increased the success rate of registration from 73.9% to 92.3%. Assessment of the 2 MMR images (max entropy and max signal-to-noise ratio (SNR)) showed that comparison to the best CSLO images (not auto-contrasted) yielded significant average image quality improvements of 158% and 4% when quantified with entropy and SNR, respectively. When compared to best auto-contrasted CSLO images, significant image quality improvements were 11% and 5% for entropy and SNR, respectively. Images constructed from auto-contrasted input images were of significantly higher quality than images reconstructed from original images. Of the 2 other images assessed (modified degree of polarization (DOP_M) and the first element of the Stokes vector (S_0)), DOP_M and S_0 yielded significant average image quality improvements quantified by entropy except for the DOP_M image of the RNFL. SNR was not improved significantly when

either SVR image was compared to the best CSLO images. Compared to the best auto-contrasted CSLO images, neither DOP_M nor S_0 improved average image quality significantly. This result might change with a larger number of participants. When MMR were applied to images of malaria infected retinal slides, image quality was improved by 19.7% and 15.3% in terms of entropy and SNR, respectively, when compared to the best CSLO image. The DOP_M image yielded image quality improvements of 8.6% and -24.3% and the S_0 image gave improvements of 9.5% and 9.4% in entropy and SNR, respectively. Although percent increase in image quality was reduced when images were compared to initial auto-contrasted CSLO images, the final image quality was improved when auto-contrasting occurred prior to polarimetry calculations for max SNR and max entropy images. Quantitative values of retardance could not be found due to physical constraints in the CSLM that did not allow for characterization of its polarization properties and vibrational noise. Mueller matrix polarimetry used to find the retardance image of a malaria infected retina sample did yield visualization of hemozoin within the vessel but only qualitatively.

In conclusion, improvements in the acquisition and registration of CSLO images were successful in leading to considerably shorter experimentation and processing times. In terms of polarimetric image quality improvement techniques, when compared to the best CSLO image. A large proportion of the improvement was in fact due to partially or completely stretching the pixel values across the dynamic range of the images within the algorithm of each technique. However, in general the image quality was still improved by the Mueller matrix reconstruction techniques using both entropy and SNR to generate the CSLO retinal images and the CSLM imaged malaria infected sample. In the malaria sample, retinal blood vessel visualization was also qualitatively improved. The images yielded from Mueller matrix polarimetry applied to a malaria infected retinal sample localized hemozoin within the blood vessel, but a quantitative image of the phase retardance could not be achieved.

Acknowledgments

I would like to thank my supervisor, Dr. Melanie Campbell, for her support, encouragement, guidance, and patience during this project. I would also like to thank my committee members, Dr. Sue Leat and Dr. Natalie Hutchings for their support and constructive discussions.

I would also like to acknowledge my fellow lab mates, Dr. Jennifer Hunter and Marsha Ksilak for their guidance and assistance during acquisition and processing of data for this thesis as well as their advice on statistical analysis. Additionally, I would like to thank Aden Seaman for his advice in programming the control system for automation of polarizing optics within the Waterloo CSLO as well assistance with code optimization. I would like to thank Kaitlin Bunghardt and Laura Emptage for their assistance with experiments and for helping me use the library resources of the University of Waterloo from my office in Victoria, BC.

I would like to thank Ted Dixon, Savvas Damaskinos, and Paul Constantinou at Biomedical Photometrics for allowing me to use their impressive imaging system, for their assistance in incorporation of polarizing optics into their system, and for their guidance during image acquisition.

I would like to acknowledge the support of this work by NSERC, Canada and support during my M.Sc. from the University of Waterloo.

Finally I'd like to thank and my friends, family and my partner Stefanie Gillett. I could not have done this without her love and support.

Dedication

To my Dad, who taught me that happiness is the best way to measure success. His guidance and wisdom made me the man I am today and I would not be here without him. He is dearly missed.

Table of Contents

List of Figures	x
List of Tables	xv
Chapter 1 - Introduction	1
1.1 Polarized Light	2
1.2 Wave Representation of Polarized Light	3
1.3 Polarizing Optics	5
1.3.1 Linear Polarizers	5
1.3.2 Phase Retarders	7
1.4 Stokes Vector	8
1.5 The Poincaré Sphere	11
1.6 The Mueller Matrix	12
1.6.1 Calculating the Retardance	13
Chapter 2 - Polarimetry Imaging and Enhancement for Malaria Retinal Samples	14
2.1 Retinal Imaging with a CSLO	14
2.2 Retinal CSLO Imaging with Polarimetry	15
2.3 Determination of Metric Improvement	20
2.4 Malaria and Polarimetry	20
Chapter 3 - Improvements in image acquisition and image processing	23
3.1 Overview	23
3.2 Introduction	24
3.3 The Waterloo CSLO	24
3.4 Methods	27
3.4.1 Analyzer and Generator Automation	31
3.4.2 Illumination variance	32
3.4.3 Image Filters	33
3.4.4 Application of Filters	36
3.4.5 Registration	38
3.4.6 Judging Successful Registration	39
3.5 Results	40
3.5.1 Analyzer and Generator Automation	40
3.5.2 Frame Averaging	43

3.5.3 Illumination variance	44
3.5.4 Influence of Controlled Variables on ONH Images.....	46
3.5.5 Sobel Filter.....	50
3.5.6 High Pass Filter.....	53
3.5.7 Canny Filter	55
3.5.8 Registration Results for ONH Images as a Function of Depth	57
3.5.9 Registration Results for Fovea Images	60
3.5.10 Registration Results for Variable Analyzer ONH Images	61
3.6 Conclusions.....	63
Chapter 4 - Reassessment of Mueller-matrix Image Quality Enhancement Methods	64
4.1 Overview.....	64
4.2 Introduction.....	64
4.3 Methods.....	65
4.3.1 Auto-contrasting.....	67
4.3.2 Mueller Matrix Reconstruction.....	68
4.3.3 Stokes Vector Reconstruction.....	72
4.3.4 Image Quality Metrics	74
4.4 Results.....	76
4.4.1 Mueller Matrix Reconstruction VS Best CSLO Image.....	76
4.4.2 Mueller matrix reconstruction VS Linear CSLO Image.....	82
4.4.3 DOP_M VS CSLO Images.....	86
4.4.4 S_0 VS CSLO Images	89
4.4.5 Auto-Contrasted MMR Inputs Increase max SNR and Entropy Values.....	94
4.4.6 Average Image Quality Improvement.....	95
4.4.7 Correlation between Auto-contrasting and Entropy Image Quality Improvement	99
4.4.8 $DOP \cdot S_0$ and DOP_M Comparison.....	105
4.5 Conclusions.....	105
Chapter 5 - Polarimetric Imaging of a Malaria Infected In Vitro Retina.....	109
5.1 Overview.....	109
5.2 Introduction.....	109
5.3 The Malaria Life Cycle.....	110
5.4 Diagnosis.....	112
5.5 Methods.....	113

5.5.1 The MACROscope.....	113
5.5.2 Polarimetry.....	115
5.5.3 Registration.....	116
5.6 Results.....	116
5.6.1 Mueller Matrix.....	119
5.6.2 Crossed Polarizer Results.....	120
5.6.3 Image Quality Improvement.....	121
5.7 Discussion.....	124
5.8 Conclusion.....	126
Chapter 6 - Conclusions.....	128
6.2 Mueller Matrix Polarimetry.....	128
References.....	132

List of Figures

Figure 1.1: Propagation of light (public domain image courtesy of NASA - http://missionscience.nasa.gov/ems/02_anatomy.html).....	3
Figure 1.2: The polarization ellipse (public domain wikipedia image - http://en.wikipedia.org/wiki/File:Polarisation_ellipse2.svg).	4
Figure 1.3: Unpolarized light incident on a linear polarizer with a vertical transmission axis (Image created by Bob Mellish. Permission to use this image is granted under the GNU Free Documentatoin License - https://en.wikipedia.org/wiki/File:Wire-grid-polarizer.svg)	6
Figure 1.4: Light incident on a half wave-plate (Image modified from image created by Bob Mellish. Permission to use this image is granted under the GNU Free Documentatoin License - https://en.wikipedia.org/wiki/File:Wire-grid-polarizer.svg).	7
Figure 1.5: Geometrical representation of Stokes vector, the Poincaré sphere (Public domain wikipedia image - http://en.wikipedia.org/wiki/File:Poincaré_sphere.svg).	11
Figure 2.1: CSLO containing x- and y-scanning units and a confocal pinhole.	14
Figure 2.2: Light outside of the focal plane is blocked by the confocal pinhole.	15
Figure 2.3: Typical CSLO containing x- and y-scanning units and a confocal pinhole with generator and analyzer units in place.....	17
Figure 3.1: CLSO with a generator incorporated into the system.....	26
Figure 3.2: The ONH (right white square), fovea of the human eye (left white square), and 15° imaging window (black square).	27
Figure 3.3: RNFL of a participant taken with incident polarized light produced by the 4 different positions of the generator unit	28
Figure 3.4: Stepper motor GUI used to control positions of quarter wave plates in both the analyzer and generator unit within the CSLO.	31
Figure 3.5: Original image Pf (r) (left) and the corresponding image following histogram equalization T(r) (right).	33
Figure 3.6: A Gaussian high-pass filter removes low frequencies in the frequency domain enhancing edges and noise.	34
Figure 3.7: A Gaussian low-pass filter removes high frequencies in the frequency domain smoothing the image.....	35
Figure 3.8: Flowchart demonstrating method for testing filter chains in the competition for highest registration success rate.	37
Figure 3.9: Reference image with five chosen landmarks..	39
Figure 3.10: Acquisition times were reduced significantly with automated rotation of the polarizing.	40
Figure 3.11: Registration times were reduced with automated rotation of the polarizing optics. Averages are taken across the three images registered for each of 3 participants.	41
Figure 3.12: Average translation misalignment using automated and manually driven polarizing optics.	42
Figure 3.13: Average rotation misalignment using automated and manually driven polarizing optics.....	42
Figure 3.14: Average of 8 images (right) shows a marked improvement in the signal-to-noise over original image (left) ratio.	43
Figure 3.15: 400μ pinhole CSLO image (left) and image with illumination correction using homomorphic techniques (right).	44

Figure 3.16: Original 100 μ pinhole image (top left), original 400 μ pinhole image (top right), histogram equalized 100 μ pinhole image (bottom left), and histogram equalized 400 μ pinhole image (bottom right).....	45
Figure 3.17: Histogram equalized image (left) and histogram equalized image followed by a low pass filter (right).....	46
Figure 3.18: 4 images corresponding to the 4 settings on the polarization state analyzer.....	47
Figure 3.19: 4 images corresponding to the 4 settings on the polarization state generator with no analyzer.	48
Figure 3.20: Images of different depths of the same ONH taken with the CSLO.....	49
Figure 3.21: No filter image (left) and Sobel filter image (right)..	50
Figure 3.22: No filter image (left) and image resulting from an histogram equalization followed by a Sobel filter (right)..	51
Figure 3.23: No filter image (left) and image resulting from an histogram equalization followed by a low pass filter followed by a Sobel filter (right).....	52
Figure 3.24: No filter image (left) and image with low pass filter followed Sobel Filter (right) with no illumination correction.....	52
Figure 3.25: No filter image (left) and the image resulting from an illumination variance correction followed by a high pass filter (right).....	53
Figure 3.26: No filter image (left) and the image resulting from a low pass filter followed by a high pass filter (right).....	54
Figure 3.27: No filter image (left) and high pass filter image (right)..	54
Figure 3.28: No filter image (left) and image with Canny filter (right).....	55
Figure 3.29: No filter image (left) and image resulting from a low pass filter followed by a Canny filter (right)	26
Figure 3.30: No filter image (left) and image resulting from histogram equalization followed by a low pass filter and then followed by a Canny filter (right).....	56
Figure 3.31: Image without filtering (left) and image resulting from a low pass filter followed by a Sobel filter (right).....	58
Figure 3.32: Image without filtering (left) and high pass filter image (right).....	59
Figure 3.33: Image without filtering (left) and image resulting from an histogram equalization followed by a low pass filter followed by a Canny filter (right).....	60
Figure 3.34: Image without filtering (top left), the same image with best Sobel filter (top right), with best high pass filter (bottom left), and with best Canny filter (bottom right).....	61
Figure 3.35: Image without filtering (top left), the same image filtered with best Sobel filter (top right), with best high pass filter (bottom left), and with best Canny filter (bottom right)..	62
Figure 4.1: Waterloo CSLO schematic with removable generator and analyzer units in place.....	66
Figure 4.2: Original low contrast and dim image (left) and an image after auto-contrasting the original (right).	68
Figure 4.3: A convenient geometrical representation of all possible polarization states (Public domain wikipedia image - http://en.wikipedia.org/wiki/File:Poincaré_sphere.svg).....	71
Figure 4.4: Percent improvement of MMR images over the best CSLO images as measured by entropy at the LC (left) and RNFL (right) depths. The fit on the left (LC) is significant while that on the right is not (RNFL).....	77

Figure 4.5: Percent improvement of MMR images over the best CSLO images as measured by SNR at the LC (left) and RNFL (right) depths. Fits shown are not significant.....	78
Figure 4.6: Percent improvement of MMR images over CSLO images as measured by entropy using auto-contrasted inputs at the LC (left) and RNFL (right) depths. Fits shown are not significant.	79
Figure 4.7: Percent improvement of MMR images over CSLO images as measured by SNR using auto-contrasted inputs at the LC (left) and RNFL (right) depths. Fits shown are not significant.	80
Figure 4.8: Best SNR CSLO image (top left), best entropy CSLO image (top right), Best auto-contrasted SNR CSLO image (bottom left), and best auto-contrasted entropy CSLO image (bottom right).	81
Figure 4.9: MMR max SNR image calculated from CSLO images (top left), MMR max entropy image calculated from the original CSLO inputs (top right), MMR max SNR image with auto-contrasted CSLO inputs (bottom left), MMR max entropy image with auto-contrasted CSLO inputs (bottom right).....	82
Figure 4.10: Percent improvement of MMR images over the CSLO image formed by linearly polarized light as measured by entropy at the LC (left) and RNFL (right) depths. The fit on the left is significant ($p=0.0833$) and that on the right is insignificant ($p=0.0573$).	83
Figure 4.11: Percent improvement of MMR images over CSLO images formed by linearly polarized light as measured by SNR at the LC (left) and RNFL (right) depths. The fits shown are insignificant.	84
Figure 4.12: Percent improvement of MMR images over the CSLO images formed by linearly polarized light as measured by entropy at the LC (left) and RNFL (right) depths. Fits shown are not significant....	84
Figure 4.13: Percent improvement of MMR images over the CSLO images formed by linearly polarized light as measured by entropy at the LC (left) and RNFL (right) depths. Fits shown are not significant....	85
Figure 4.14: Original CSLO image formed by linearly polarized light (left), auto-contrasted CSLO image formed by linearly polarized light (right).	86
Figure 4.15: Percent improvement of DOP_M images over the best CSLO images as measured by entropy at the LC (left) and RNFL (right) depths. The fit shown on the left is not significant and that on the right is significant.	87
Figure 4.16: Percent improvement of DOP_M images over the best CSLO images as measured by SNR at the LC (left) and RNFL (right) depths. Fits shown are not significant.....	87
Figure 4.17: Percent improvement of DOP_M images over the best auto-contrasted CSLO images as measured by entropy at the LC (left) and RNFL (right) depths. Fits shown are not significant.....	88
Figure 4.18: Percent improvement of DOP_M images over the best auto-contrasted CSLO images as measured by SNR at the LC (left) and RNFL (right) depths. The fit shown on the left is not significant and the one on the right is significant.	89
Figure 4.19: Percent improvement of S_0 images over the best CSLO images as measured by entropy at the LC (left) and RNFL (right) depths. The fit shown on the left is not significant and the one on the right is significant.....	90
Figure 4.20: Percent improvement of S_0 images over the best CSLO images as measured by SNR at the LC (left) and RNFL (right) depths. The fit shown on the left is not significant and the one on the right is significant.....	91
Figure 4.21: Percent improvement of S_0 images over the best auto-contrasted CSLO images as measured by entropy at the LC (left) and RNFL (right) depths. Fits shown are not significant.....	92
Figure 4.22: Percent improvement of S_0 images over the best auto-contrasted CSLO images as measured by SNR at the LC (left) and RNFL (right) depths. Both fits shown are significant.	93
Figure 4.23: DOP_M image (left), and S_0 image (right).....	93

Figure 4.24: Performance increase of the max entropy image produced by MMR when inputting auto-contrasted CSLO images instead of original CSLO images. The increase in performance was not significantly greater than zero ($p = 0.061$).....	94
Figure 4.25: Performance increase of the max SNR image produced by MMR when inputting auto-contrasted CSLO images instead of original CSLO images. The increase in performance was significantly greater than zero ($p < 0.0001$).....	95
Figure 4.26: Average percent increase in entropy value of MMR images when using original (black) and auto-contrasted (grey) CSLO images. Error bars shown are standard deviations of the percent increase in entropy value across all participants.	96
Figure 4.27: Average percent increase or decrease in entropy value of SVR images when compared to original (black) and auto-contrasted (grey) CSLO images. Error bars shown are standard deviations of the percent change in entropy value across all participants.	97
Figure 4.28: Average percent increase in SNR value of MMR images when using original (black) and auto-contrasted (grey) CSLO images. Error bars shown are standard deviations of the percent increase in SNR value across all participants.....	98
Figure 4.29: Average percent increase in SNR value of SVR images when compared to original (black) and auto-contrasted (grey) CSLO images. Error bars shown are standard deviations of the percent increase in SNR value across all participants.	99
Figure 4.30: Correlation between percent increase in entropy of an image versus the percent increase in max pixel value of the same image when that image is auto-contrasted. A significant cubic fit is shown ($p < 0.0001$, $R^2 = 0.9762$).....	100
Figure 4.31: Difference seen in entropy value versus the difference in pixel value of an image when it is auto-contrasted. The fit shown is significant.	101
Figure 4.32: Mean maximum pixel value taken across each participant's 16 CSLO images as a function of age. The fit shown is significant.	102
Figure 4.33: Increase in mean maximum pixel value when an image is auto-contrasted as a function of age. The fit shown is significant.	103
Figure 4.34: Increase in mean maximum pixel value when an image is auto-contrasted as a function of age. The fit shown is not significant.	104
Figure 4.35: DOP_M image compared to $DOP \cdot S_0$ image with SNR and entropy values.	105
Figure 5.1: Life cycle of malaria (image was released into the public domain by Center for Disease Control - http://phil.cdc.gov/phil/details.asp).	112
Figure 5.2: Image of a malaria infected retina taken on a Macroscope (left). Small ROI taken after acquisition (right).....	114
Figure 5.3: Small section (0.25 mm^2) of vessel from the retinal sample taken at 1μ resolution.	117
Figure 5.4: Mueller matrix maps of a small section (0.25 mm^2) of vessel from the retinal sample taken at 1μ resolution.	119
Figure 5.5: Total retardance map calculated from the Mueller matrix.	120
Figure 5.6: Malaria retinal sample in a near crossed polarizer setup.	121
Figure 5.7: Original best auto-contrasted MACROscope image (top), MMR SNR image (bottom left), and MMR entropy image (bottom right).	122
Figure 5.8: Original auto-contrasted MACROscope image (top), SVR DOP_M image (bottom left), and SVR S_0 image (bottom right).	123

Figure 5.9: Thresholded crossed polarization map (left) compared to thresholded retardance map (right).
..... 124

Figure 5.10: Hemozoin deposits left behind in a malaria infected red blood cell (public domain wikipedia
image - http://en.wikipedia.org/wiki/File:P.falciparum_schizont.jpg) 125

Figure 5.11: Improvement in blood vessel visualization for smaller (above) and larger (below) vessels.
From left to right – Best auto-contrasted MACROscope image, MMR best SNR image, MMR best
entropy image, SVR best DOP_M image, and best SVR S_0 image. 126

List of Tables

Table 3.1: Participant source and imaging conditions.	29
Table 3.2: Average translation and rotation over 3 images for polarizing optics.	41

Chapter 1 - Introduction

The need for high quality retinal images and new imaging techniques for imaging retinal diseases has never been greater as a high percentage of the population moves into old age. The ability of clinicians to quickly diagnose many diseases relies heavily on the image quality of fundus imaging systems. Many diseases, such as diabetes, age-related macular degeneration and glaucoma result in physical and visible changes on the retina such as retinal bleeding and drusen deposits [Quillen, 1999]. Detection of diabetic retinopathy in the early stages of diabetes can play a major role in early disease diagnosis and management [Simandjuntak, 2005]. The onset of glaucoma leads to irregular changes in the shape of the optic nerve head (ONH) [Burke, 2006]. To complicate matters, fundus imaging may be confounded by ocular aberrations [Fujikado, 2004] and scattering [Kuroda, 2002] that increase with age, reducing the quality of retinal imaging.

The central topic of this thesis is retinal image acquisition and improvement using Mueller matrix polarimetry and confocal scanning laser ophthalmoscope (CSLO) imaging. I describe improvements made that increased the efficiency of acquisition and image processing of polarimetric retinal images. I show how the addition of stepper motor driven mounts semi-automate the rotating quarter-wave plates in our polarization imaging setup. This significantly reduced overall experiment time. Faster acquisitions also showed potential for faster alignment of images (registration) as fewer eye movements were observed. Image processing time was also reduced substantially by the incorporation of Fourier-space edge detection techniques that improved the success rate of image registration substantially (chapter 3). I then reassess the performance of two image quality enhancement techniques based on Mueller matrix polarimetry developed by Bueno et al. [Bueno, 2002] Images were compared by the authors to CSLO images when their performance was quantified by image quality metrics. In these methods, pixel values were stretched partially or completely across the dynamic range of the image in addition to polarization enhancement techniques, but are then compared to original CSLO images which have not been stretched (chapter 4). In my work I quantify the improvement due to the stretching as well as to the polarimetry method of Bueno et al. [Bueno, 2007]. Finally, I apply Mueller matrix polarimetry to try to isolate hemozoin in the images of a cerebral malaria infected retinal

sample. Using polarization imaging techniques, retinal samples are imaged which contain the malaria parasite to exploit the known birefringence of hemozoin deposits left behind by the parasite in the human retina. Image quality enhancement techniques are applied to malaria infected images and visualization of retinal blood vessels which are important for diagnosis of retinopathy is improved (chapter 5).

Before discussing current methods of Mueller matrix polarimetry for fundus imaging, it is important to understand the background terminology and mathematical theory of polarization as described by the polarization ellipse, Stokes vector, and Mueller matrix.

1.1 Polarized Light

In the early 19th century the wave theory of light, developed by Augustin Jean Fresnel and others, was the dominant theory governing the main understanding of optics. Specifically, polarization was explained through wave amplitudes and this yielded descriptions of elliptical, circular, and linear polarization states. However, a significant hole in the theory emerged in the mid-1800s. The theory could not mathematically explain depolarized light or partially polarized light.

In 1952, Sir George Gabriel Stokes solved this predicament. His success was realized by his novel approach to the subject. Earlier works had all followed the same line of thinking as Fresnel's wave theory of light, which described light by its wave amplitudes. Stokes took a unique approach, describing light in terms of an observable measure, its intensity. This introduced optics to today's description of polarization, the Stokes vector [Quillen, 1999].

Before discussing the theory of polarized light described by the Stokes vector, we will first examine the physical nature of polarized and unpolarized light to help lay the ground work for understanding polarized light and polarizing optics. The way light interacts with matter is important to polarization because light can become depolarized through absorption, reflection and scattering [Nee, 1999]. Some materials can also cause a phase shift in polarized light along a given orientation, changing the polarization state. These physical phenomena will aid in the overall understanding of polarized light, polarizing optics and subsequent chapters in this thesis.

1.2 Wave Representation of Polarized Light

Light can be represented by the propagation of an electromagnetic wave (EM) through space, where the oscillations of the electric and magnetic waves are orthogonal to each other and perpendicular to the direction of propagation (figure 1.1).

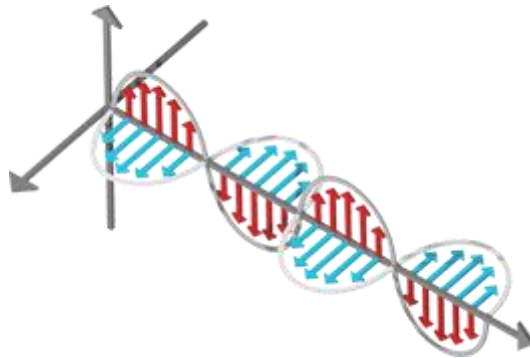


Figure 1.1: Propagation of light (public domain image courtesy of NASA - http://missionscience.nasa.gov/ems/02_anatomy.html).

When unpolarized light is emitted from a source like the sun, the electromagnetic wave oscillates randomly in all directions. However, if the light becomes linearly polarized, the EM wave oscillates in a fixed direction in space [Pedrotti, 1998].

If the light is linearly polarized, the E-vector will oscillate in a fixed orientation. This will occur when the E_x and E_y components are in phase or 180° out of phase. In this circumstance, the relative amplitudes of E_x and E_y will determine the specific orientation of the linearly polarized light. If the phase difference between the E_x and E_y components is between 0 and 180° , the light will be circularly or elliptically polarized. As the E_x and E_y components become out of phase, the E-vector will begin to trace out an ellipse. At phase differences of 90° and 270° , the ellipse forms a perfect circle in the form of right circularly and left circularly polarized light, respectively [Hecht, 2002]. The states are easiest to picture by imagining a pendulum's x and y components, where the pendulum bob itself represents the position of the tip of the E-vector. When in phase, the x and y positions of the pendulum would reach maximum values of displacement and cross the origin of the pendulum at the same time, tracing out a line. If they were out of phase, the pendulum bob would trace out an ellipse.

This is well described by the polarization ellipse equation [Collett, 1992]:

$$\frac{E_x^2}{E_{0x}^2} + \frac{E_y^2}{E_{0y}^2} - \frac{2E_xE_y\cos\delta}{E_{0x}E_{0y}} = \sin^2\delta \quad (1.1)$$

Where δ is the phase difference between E_y and E_x , $\delta = \delta_x - \delta_y$, E_{0x} and E_{0y} are constants representing maximum amplitude of the waves and E_x and E_y represent the instantaneous components of the wave as a function of time. Equation 1.1 is already in the form of an ellipse rotated about the center of the Cartesian coordinate system (figure 1.2). The generality of this rotation is necessary, because in practice, the major and minor axes of the polarization ellipse are rarely parallel to the axis of the coordinate system used to describe it.

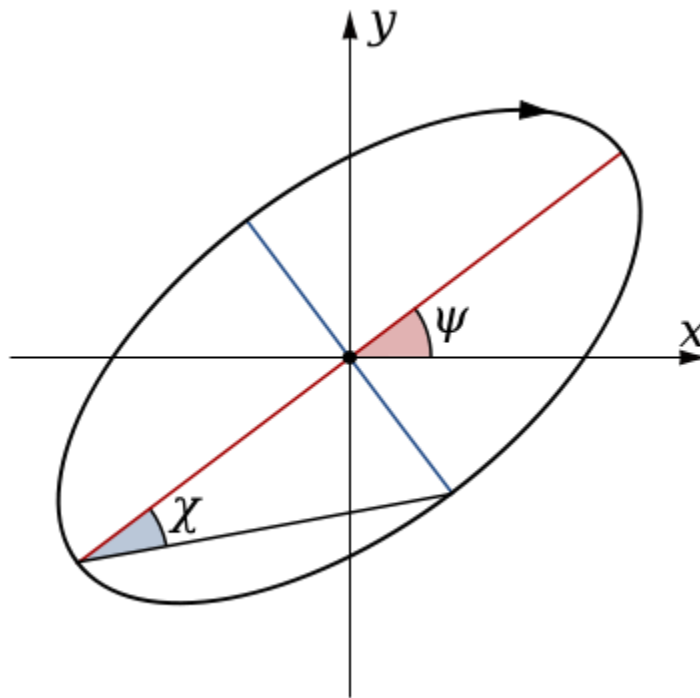


Figure 1.2: The polarization ellipse (public domain wikipedia image - http://en.wikipedia.org/wiki/File:Polarisation_ellipse2.svg).

Of particular importance for this work are two angular values that are used to describe the polarization ellipse, the orientation angle ψ which determines the angle relative to the x axis and the ellipticity angle χ . These angles ultimately describe the ratio between the major and minor

axes of the ellipse through trigonometry and are related to the Poincaré sphere, discussed in a later section. Defining these in terms of the polarization ellipse we see that [Collett, 1992]:

$$\tan 2\psi = \frac{2E_{0x}E_{0y}}{E_{0x}^2 - E_{0y}^2} \cos \delta \quad \text{where,} \quad 0 \leq \psi \leq \pi \quad (1.2)$$

$$\sin 2\chi = \frac{2E_{0x}E_{0y}}{E_{0x}^2 + E_{0y}^2} \sin \delta \quad \text{where,} \quad -\frac{\pi}{4} < \chi \leq \frac{\pi}{4} \quad (1.3)$$

These parameters are defined to work well with the Stokes vector formulation and with the geometrical representation of all polarization states in the Poincare sphere. Before delving into these mathematical representations, in an attempt to gain a higher understanding for polarization and to understand the polarizing optics used in this thesis, we will explore how polarized light physically interacts with optical elements and matter in general.

1.3 Polarizing Optics

Polarizing optics were developed to control polarized light for specific applications, be they for research and development or for commercial purposes. Two important tools which can be used to produce any possible state of polarization of light are the linear polarizer and the retarder. While many types of materials and varying physical designs have been developed to produce these tools for different demands of quality and cost, the rudimentary purpose remains the same. For the purpose of this thesis, only designs for polarizing optics used in experiments for this work will be discussed in detail.

1.3.1 Linear Polarizers

Generally speaking, materials that absorb light differently based on the direction of polarization or differing frequencies of the incident light are considered dichroic. Ideal linear polarizers transmit electric fields oscillating in a certain direction, eliminating electric fields that

oscillate in all other directions. The emitted light is therefore linearly polarized in the direction allowed by the linear polarizer, known as the transmission axis (figure 1.3).

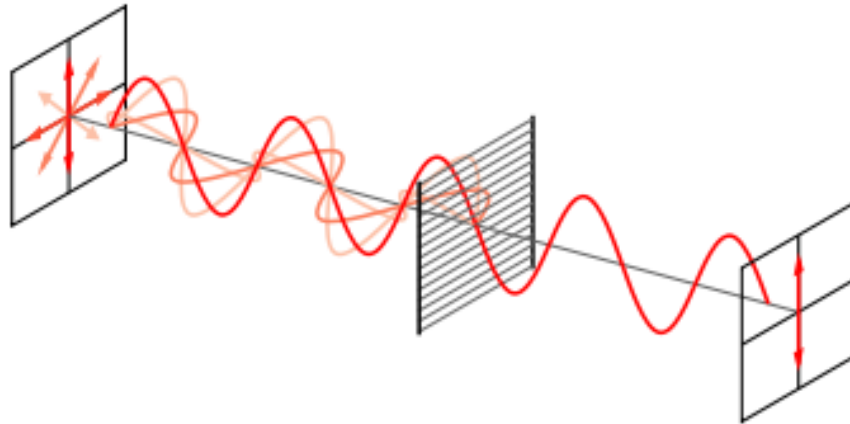


Figure 1.3: Unpolarized light incident on a linear polarizer with a vertical transmission axis (Image created by Bob Mellish. Permission to use this image is granted under the GNU Free Documentatoin License - <https://en.wikipedia.org/wiki/File:Wire-grid-polarizer.svg>).

There are two basic types of linear polarizers; those that reflect and those that absorb. Absorbing polarizers (as used in experiments in this thesis), work by absorbing light along polymer or crystal chains running parallel to the oscillation of the wave. This allows perpendicularly oscillating light to be transmitted through as linearly polarized light.

Reflecting polarizers exploit the fact that light incident on a transparent media where there is a change in the index of refraction will be reflected or transmitted depending on its polarization state. Incident light that is polarized parallel to the plane of incidence will transmit and light perpendicular to the plane will reflect at an angle of incidence known as Brewster's angle.

Polarization through birefringence occurs because light will see a different change in refractive index that is dependent on the orientation of the oscillation of the electromagnetic waves. Horizontal and vertical polarization states can be separated and then, using total internal reflection, the unwanted ray can be reflected out one side of the optic while the other is allowed to transmit as linearly polarized light [Hecht, 2002].

The result of light incident on an ideal polarizer (which does not absorb any of the transmitted polarization) is well described by Malus' Law [Hecht, 2002]:

$$I(\theta) = I(0)\cos^2\theta \quad (1.4)$$

Where θ is the angle between the linearly polarized light and the transmission axis and $I(0)$ is the irradiance arriving at the linear polarizer.

1.3.2 Phase Retarders

Phase retarders do not eliminate either the x or y component of the electric field. The component parallel to the fast axis is allowed through without being affected, while the component parallel to the slow axis is slowed to introduce a phase difference between the two orthogonal components. When the x and y components are out of phase, the light becomes elliptically polarized (figure 1.4).

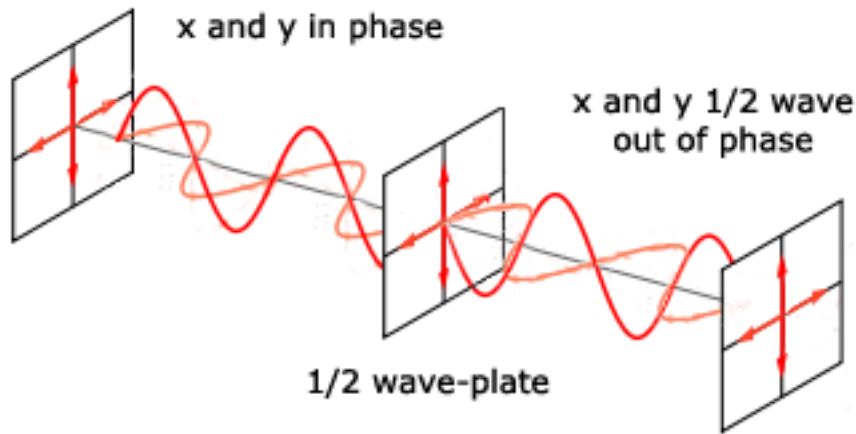


Figure 1.4: Light incident on a half wave-plate (Image modified from image created by Bob Mellish. Permission to use this image is granted under the GNU Free Documentatoin License - <https://en.wikipedia.org/wiki/File:Wire-grid-polarizer.svg>).

Therefore, phase retarders are used to create elliptically (or circularly) polarized light and are often referred to by how much they put the two components out of phase with each other. For example, a retarder that put the two components 90° out of phase with each other is called a quarter-wave plate.

1.4 Stokes Vector

Every possible polarization state can be represented by the Stokes vector, $[S_0 \ S_1 \ S_2 \ S_3]$, composed of four parameters defined as [Collett, 1992]:

$$S_0 = E_x^2 + E_y^2 \quad (1.5)$$

$$S_1 = E_x^2 - E_y^2 \quad (1.6)$$

$$S_2 = E_x^2 E_y^2 \cos \delta \quad (1.7)$$

$$S_3 = 2E_x^2 E_y^2 \sin \delta \quad (1.8)$$

For polarized light, it can be shown that equation 1.5 can be expressed in terms of 1.6 – 1.8 so that:

$$S_0^2 = S_1^2 + S_2^2 + S_3^2 \quad (1.9)$$

For any degree of polarization, the Stokes parameter S_0 is equal to the intensity of light:

$$S_0 = I \quad (1.10)$$

Again, E_x and E_y are the magnitudes of the x and y components and δ is the phase difference between the x and y components measured in radians. S_1 , S_2 , and S_3 are linearly independent vectors. Each Stokes parameter has a significant physical meaning; S_0 yields the intensity of the light while S_1 to S_3 represent the polarization state of the field with S_1 showing the amount of horizontal and vertical linear polarization, S_2 the amount of -45° and 45° polarization, and finally S_3 , describing right and left circular polarization [Collett, 1992]. From these vectors all polarization states can be found since all the information about polarization is present. All of the Stokes parameters are real quantities with units of intensity. In equation 1.10, S_0 resembles the distance vector r on a Poincare sphere in Cartesian coordinates [Bour, 1991] (figure 1.5).

There are two main advantages of this formulation over simply using the polarization ellipse to describe polarized light. Firstly, one cannot observe the polarization ellipse. The ellipse is physically traced out in the time it takes light to travel one wavelength, which is on the order of

10^{-15} seconds, making it impossible to observe. The Stokes vector is derived directly from observables, making it verifiable and easy to measure. Second, the polarization ellipse can only be used to describe completely polarized states. This is extremely inconvenient as in real situations, light is almost never 100% polarized due to the fact that many light sources do not emit polarized light and also because of the depolarizing effects from light's interaction with matter.

Recalling the equations for the angle of orientation ψ and the ellipticity angle χ for a polarization ellipse [Collett, 1992]:

$$\tan 2\psi = \frac{2E_{0x}E_{0y}}{E_{0x}^2 - E_{0y}^2} \cos \delta \quad \text{where,} \quad 0 \leq \psi \leq \pi \quad (1.11)$$

$$\sin 2\chi = \frac{2E_{0x}E_{0y}}{E_{0x}^2 + E_{0y}^2} \sin \delta \quad \text{where,} \quad -\frac{\pi}{4} < \chi \leq \frac{\pi}{4} \quad (1.12)$$

It becomes clear that the polarization ellipse equations can be expressed by the Stokes parameters, so that:

$$\tan 2\psi = \frac{S_2}{S_1} \quad \text{where,} \quad 0 \leq \psi \leq \pi \quad (1.13)$$

$$\sin 2\chi = \frac{S_3}{S_0} \quad \text{where,} \quad -\frac{\pi}{4} < \chi \leq \frac{\pi}{4} \quad (1.14)$$

This leads to the conclusion that, once measured, the Stokes parameters can be used to describe the shape of the polarization ellipse.

It is also useful to define the degree of polarization (DOP) for an electromagnetic wave. This is done easily through the Stokes parameters. Since S_1 , S_2 , and S_3 represent all the possible

intensities for orthogonally polarized light in an optical field and S_0 describes the total intensity of the beam, we can simply define our DOP as:

$$DOP = \frac{(S_1^2 + S_2^2 + S_3^2)^{\frac{1}{2}}}{S_0} \quad \text{where,} \quad 0 \leq DOP \leq 1 \quad (1.15)$$

A DOP value of 1 will exist for completely polarized light, while a DOP value of 0 represents completely depolarized light with all other values being some degree of partially polarized light [Collett, 1992]. It can also be convenient to express the Stokes vector elements in terms of ψ and χ . If we rearrange equations 1.13 and 1.15:

$$S_2 = S_1 \tan 2\psi \quad (1.16)$$

$$S_3 = S_0 \sin 2\chi \quad (1.17)$$

Combining these with equation 1.9 and incorporating the DOP yields:

$$S_1 = (DOP)S_0 \cos 2\chi \cos 2\psi \quad (1.18)$$

$$S_2 = (DOP)S_0 \cos 2\chi \sin 2\psi \quad (1.19)$$

$$S_3 = (DOP)S_0 \sin 2\chi \quad (1.20)$$

This formulation bears a striking resemblance to spherical coordinates having the form:

$$x = r \sin \theta \cos \phi \quad (1.21)$$

$$y = r \sin \theta \sin \phi \quad (1.22)$$

$$z = r \cos \theta \quad (1.23)$$

You may notice that the equations are not identical, but $\sin \theta$ and $\cos \theta$ only differ by a phase factor of 90° . By defining θ and ϕ in terms of ψ and χ , we see the exact analogous relationships using:

$$\theta = 90^\circ - 2\chi \quad (1.24)$$

$$\phi = 2\psi \quad (1.25)$$

This leads to a visual geometrical representation of the Stokes parameters called the Poincaré sphere.

1.5 The Poincaré Sphere

All points on the surface of the Poincaré sphere represent a different polarization of light and every possible polarization state can be represented this way [Bour, 1991] (figure 1.5).

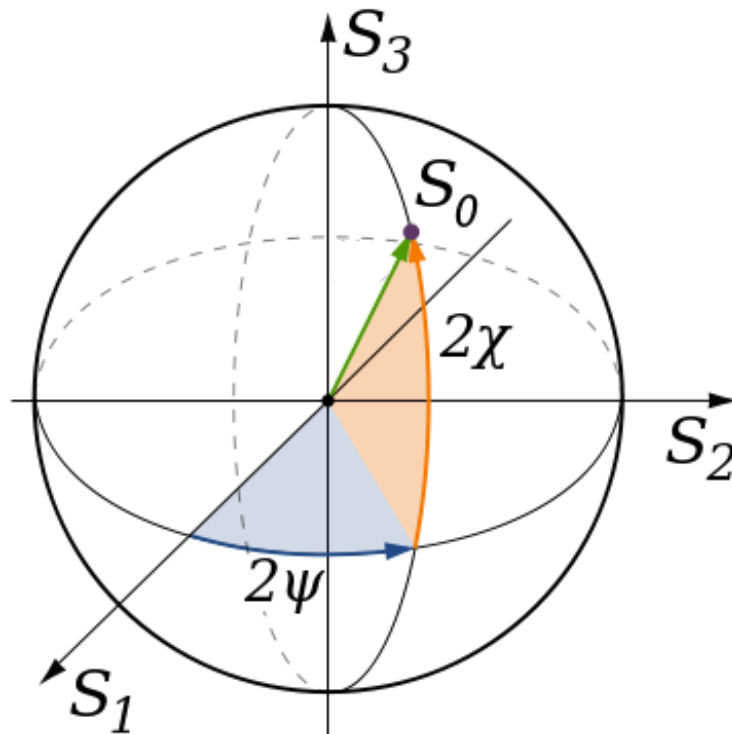


Figure 1.5: Geometrical representation of Stokes vector, the Poincaré sphere (Public domain wikipedia image - http://en.wikipedia.org/wiki/File:Poincaré_sphere.svg).

S_1 , S_2 , and S_3 are the axes of the three dimensional system, where S_0 is the radius of the sphere. The angles of S_0 with respect to the axes, can be used alone to find the polarization of any given vector from the origin to the surface of the sphere, where ψ is the orientation of the ellipse and χ is the ellipticity [Bour, 1991].

An ellipticity of 0 yields linear polarization. Using figure 1.5, this corresponds to any point along the equator of the sphere and therefore, all potential linear polarizations of light. As χ is increased, the ellipse becomes apparent until it becomes the special case of circularly polarized light at the north and south poles of the sphere. The Poincaré sphere was developed to simplify applications which involved many different polarizing elements. Originally, this could only be done through extensive and tedious algebra. It can be used to determine the Stokes vector of light after propagating through elements but this treatment will not be discussed at length in this thesis. An extensive account of the use of the Poincaré sphere for this purpose can be found in [Collett, 1992]. In this thesis however, we will be focusing on using the Mueller matrix and matrix calculus to explore the interaction of polarized light with matter.

1.6 The Mueller Matrix

Mueller matrices describe the change in polarization state when polarized light interacts with matter. It is defined as the transform matrix (M) which yields the exiting Stokes vector (S_{OUT}) for any incident Stokes vector (S_{IN}).

$$\begin{bmatrix} S^{OUT} \\ S_1^{OUT} \\ S_2^{OUT} \\ S_3^{OUT} \end{bmatrix} \equiv \begin{bmatrix} M_{00} & M_{01} & M_{02} & M_{03} \\ M_{10} & M_{11} & M_{12} & M_{13} \\ M_{20} & M_{21} & M_{22} & M_{23} \\ M_{30} & M_{31} & M_{32} & M_{33} \end{bmatrix} \begin{bmatrix} S^{IN} \\ S_1^{IN} \\ S_2^{IN} \\ S_3^{IN} \end{bmatrix} \quad (1.26)$$

The Mueller matrix also gives a complete mathematical description of the polarization properties of any sample. When the Mueller matrix is fully or even partially known, images and the resultant Stokes vector, S_{OUT} , can now be obtained mathematically for *any* incoming polarization state. Measuring the Mueller matrix of a sample allows one to calculate the polarization properties retardance, diattenuation, and polarizance which give quantifiable knowledge of how a sample will affect incident polarized light. Retardance is a measure of the phase change observed between orthogonal axes as polarized light interacts with an optical element where the phase along one axis is changed relative to the corresponding orthogonal axis. Diattenuation is the property of an optical element (a diattenuator, such as a linear polarizer) where the intensity of an exiting beam is a maximum along one axis and a minimum for the corresponding

orthogonal axis. Finally, polarizance is the degree of polarization (DOP) produced by an optical element when the light incident on the element is randomly polarized.

1.6.1 Calculating the Retardance

Lu and Chipman [1996] found that after the Mueller matrix of the sample has been calculated, the retardance, diattenuation, and polarizance of a sample could be found.

The first step is to obtain the diattenuation and polarizance vectors from the Mueller matrix. If we have a Mueller matrix M , we can break it up using polar decomposition. For a depolarization Mueller matrix, we have:

$$M = M_{\Delta}M_R M_D \quad (1.27)$$

Once the retardance matrix M_R is found, the value of retardance can be found for any sample at each pixel location (equation 1.33).

$$R = \cos^{-1} \left[\frac{\text{tr}(M_R)}{2} - 1 \right] \quad (1.28)$$

This yields an image which describes the retardation value, derived from the Mueller matrix, for any sample. For a complete derivation of equation 1.28 and the calculation of DOP, please refer to work by Lu and Chipman [Lu, 1996].

The descriptions in this chapter have given the necessary background for the understanding of polarization and simple polarizing optics. We can now extend this knowledge to the application of Mueller matrix polarimetry in imaging systems, in particular, in the confocal scanning laser ophthalmoscope (CSLO).

Chapter 2 - Polarimetry Imaging and Enhancement for Malaria Retinal Samples

2.1 Retinal Imaging with a CSLO

The confocal scanning laser ophthalmoscope is a laser based imaging system which relies fundamentally on a raster scan pattern. The CSLO was first introduced by Webb et al in 1987 [Webb, 1987] and was based on earlier work by Webb et al who developed a scanning laser ophthalmoscope (SLO) in 1981 [Webb, 1981]. The system uses two scanning units to scan the back of the eye en face in the x- and y-direction, respectively. This concept is similar to that of a raster scan in a CRT television or monitor, sweeping out a square on the retina. Typically, this is done with a rotating mirror and stepper motor mounted mirror or a pair of resonant galvometers.

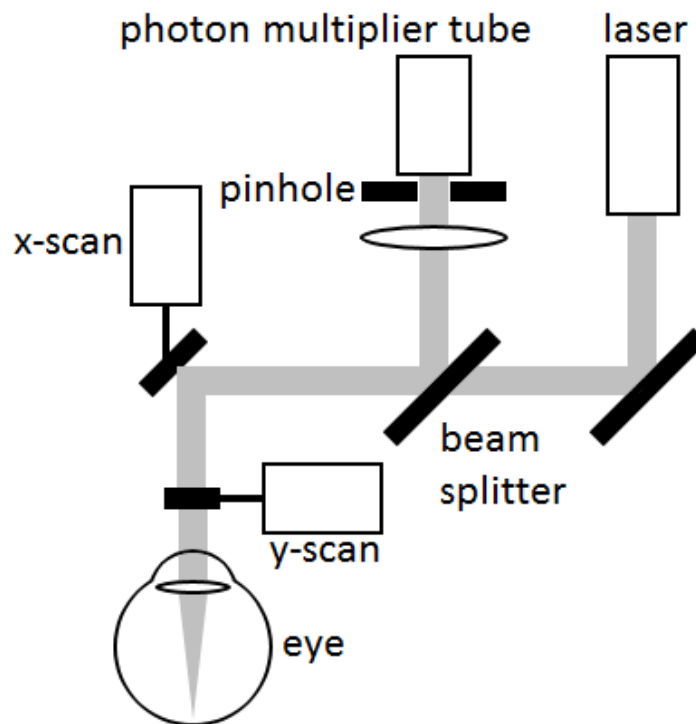


Figure 2.1: CSLO containing x- and y-scanning units and a confocal pinhole.

After the light reflects off the retina, it is de-scanned and passes through a small confocal pinhole. The light then passes into a photomultiplier tube where it is reassembled into a 2D image of the fundus and saved to disk.

The confocal pinhole greatly reduces the amount of out of focus and scattered light captured which in turn increases the depth resolution and contrast for the planar image of the focal plane created on the retina.

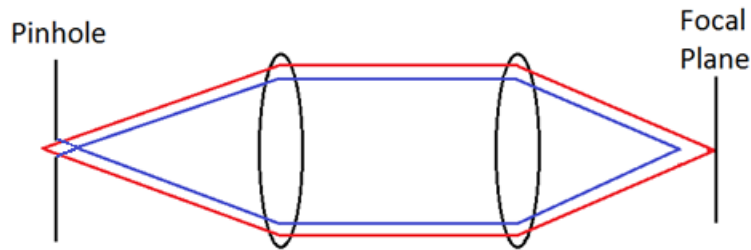


Figure 2.2: Light outside of the focal plane is blocked by the confocal pinhole.

The increased depth resolution allows the CSLO to capture thin slices of the sample at the focal plane. By adjusting the pinhole diameter, the thickness of the slice may be changed; the larger the pinhole, the larger the depth of field [Semwogerere, 2005].

2.2 Retinal CSLO Imaging with Polarimetry

Mueller matrix ellipsometry was first applied to the *in vivo* human retina by van Blokland [van Blokland, 1985] who studied the changes in polarization state and degree of polarization in double pass imaging based on an ellipsometer design by Hauge [Hauge, 1978] allowing for the use of non-ideal retarders. Polarization properties were further studied by Weinreb et al. who incorporated a polarimeter into a SLO to compare the nerve fibre layer of participants with both normal and glaucomatous eyes (eyes which have suffered characteristic damage to the optic nerve head) [Weinreb, 1995]. Bueno and Artal then were able to obtain 16 images corresponding to the Mueller matrix values for each pixel in the images. This is the spatially resolved Mueller matrix (figure 5.4 in Chapter 5). The degree of polarization was also calculated for each pixel in images reflected off both retinal and pupil planes of the human eye [Bueno, 1999].

Since its application to the human eye, polarimetry has been used to assess the retinal nerve fibre layer in the diagnosis of the early stages of glaucoma by measuring the retardance and inferring the thickness of the tissue [Burke, 2006], [Cense, 2004]. VanNasdale et al. showed that the birefringence of Henle's nerve fiber layer could be exploited to localize the fovea even in the presence of severe AMD [VanNasdale, 2012]. VanNasdale et al. also used polarimetry to study changes in photoreceptor axons by assessing the retardance of the central macula as a function of age for 120 participants [VanNasdale, 2011]. Bueno et al. assessed the degree of polarization (DOP) as a function of age by assessing the average DOP along a peripapillary annulus around the optic nerve head [Bueno, 2009]. Twietmeyer et al. incorporated Mueller matrix ellipsometry into the well established GDx scanning laser polarimeter for use in a clinical setting to assess polarization properties of the human eye's retinal nerve fiber layer..

The quality of CSLO images has also been improved through polarimetry by increasing contrast and brightness, enhancing visibility of features on the retina. Miura et al. used polarimetry to reveal retinal leakage from central serous chorioretinopathy in 30 patients, greatly enhancing contrast and visibility for all participants [Miura, 2005]. Bueno and Jaronski first used Mueller matrix polarimetry to determine polarization properties for *in vitro* corneas [Bueno, 2001]. In 2002, Bueno and Campbell extended this method to *in vivo* retinal measurements [Bueno, 2002] to improve image quality of fundus images. By incorporating a polarized light generator into the entrance beam and analyzer unit into the exit beam of a CSLO, the Mueller matrix of the sample was found. Images were captured using a 633-nm HeNe laser with a 600 μm diameter confocal pinhole placed at the detector. A positive percent change in the image quality metric signal-to-noise ratio (SNR) of 45% was found for their fundus image of a blood vessel when compared to the original CSLO image that yielded the highest SNR and as much as a 30% increase in contrast across blood vessels.

To find the Mueller matrix, a generator and an analyzer were incorporated into a CSLO. The generator consists of a linear polarizer followed by a rotating quarter-wave plate while the analyzer is the opposite, a rotating quarter-wave plate followed by a linear polarizer. The generator allows control over the input Stokes vectors while the analyzer allows one to measure the Stokes vectors after reflection of the input light out of the eye. Properly used with the CSLO (figure 2.3), the Mueller matrix of the eye may be determined.

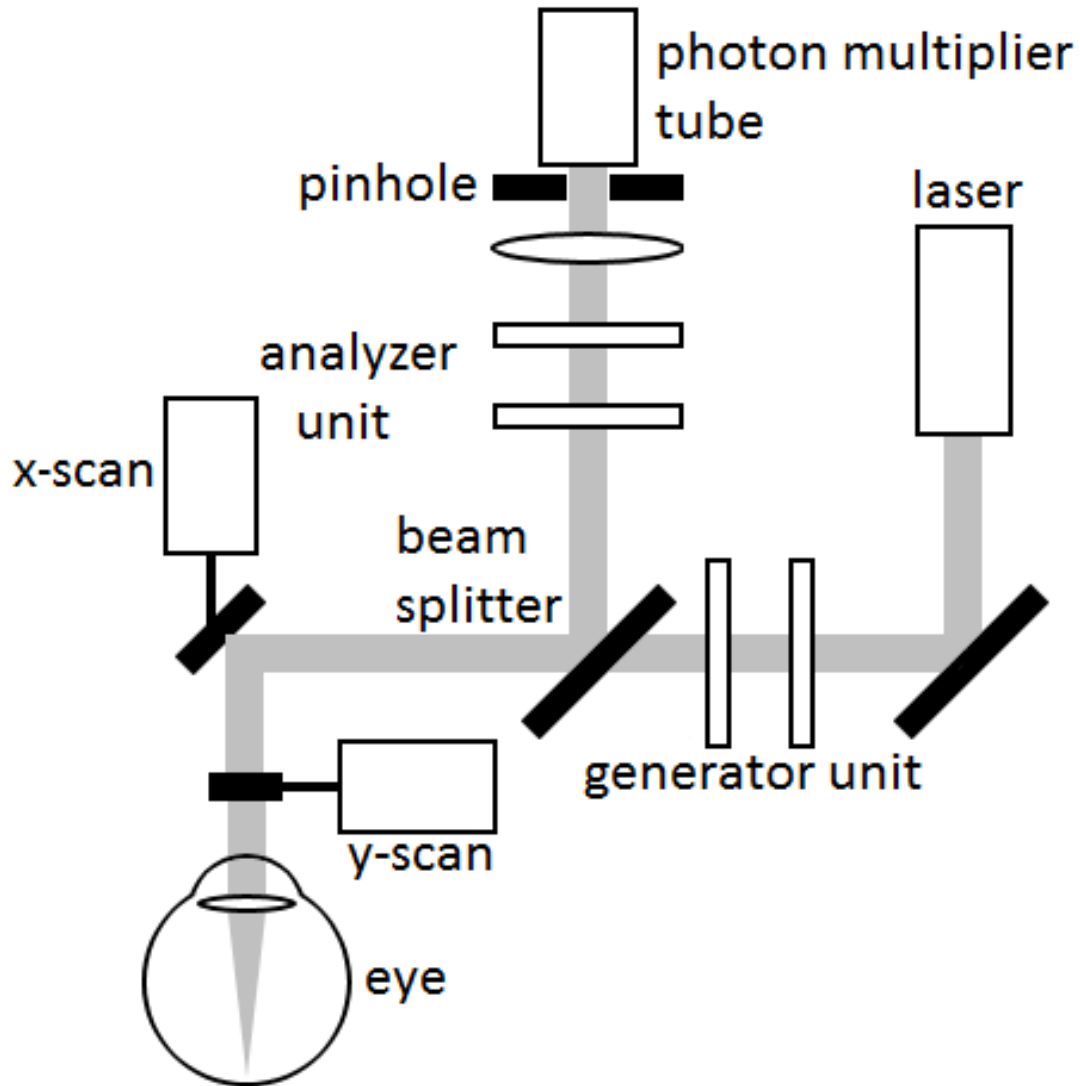


Figure 2.3: Typical CSLO containing x- and y-scanning units and a confocal pinhole with generator and analyzer units in place.

In the first implementation of their method, Bueno and Campbell (2002) took 16 recordings of the optic nerve head, each corresponding to different pairs of settings on the generator and analyzer. The rotating quarter-wave plate on both the generator and analyzer are rotated through -45° , 0° , 30° , and 60° with respect to the vertical axis of the linear polarizer, yielding 16 different possible configurations. These 4 positions lead to one circular, one linear, and two elliptical polarization states for the rotations of the quarter wave plate, respectively, from which the Mueller matrix and improved images were calculated.

These settings are based on work by Ambirajan and Look [Ambirajan, 1995] who employed Stokes vector measurement techniques by Pezzaniti and Chipman [Pezzaniti, 1990], mathematically finding the optimal angles for the quarter-wave plate within the generator and analyzer units.

Bueno et al. then simplified their method of improving image quality to only find the top row of the Mueller matrix, requiring only 4 images to be captured and registered instead of 16, reducing acquisition and processing time [Bueno, 2005], [Bueno, 2007]. This setup only requires a generator to be incorporated into a CSLO. Since the generator produces known polarization states, the Stokes vector for each of the 4 configurations of the generator unit are known. Additionally, the spatially resolved intensity image produced by each generator setting is captured by the CSLO. Using these, the top row of the Mueller matrix can be determined (see section 4.3.3 for a complete derivation).

Once the top row of the Mueller matrix is known, the output intensity image (S_0^{OUT}) that would be the result of *any* polarization state incident on the sample may be constructed by varying χ and φ .

$$S_0^{OUT} = [m_{00} \quad m_{01} \quad m_{02} \quad m_{03}] \cdot \begin{bmatrix} 1 \\ S_0 \cos 2\chi \cos 2\psi \\ \cos 2\chi \sin 2\psi \\ \sin 2\chi \end{bmatrix} \quad (2.1)$$

The variables χ and φ are swept through in 5° steps producing the output images resulting from the many possible input polarization states. Image quality is quantified for each output image by calculating the image quality metrics, entropy and SNR. The images yielding the highest values of these image quality metrics are labeled 'best' image and then quantitatively compared to the original CSLO images for which the metrics, SNR and entropy, are calculated. Bueno et al. found positive percent changes of SNR of about 5% and up to approximately 75% in terms of entropy for constructed images and image quality improvement was shown for each subject in both SNR and entropy [Bueno, 2007].

Using a similar method with an analyzer unit incorporated in front of a photon multiplier tube, Bueno and Vohnsen maximized the value of a contrast measurement (as opposed to SNR and entropy) across retinal blood vessels in an adaptive optics corrected CSLO [Bueno, 2005].

Bueno et al. also presented a second method that incorporated both a generator and analyzer into a CSLO, as seen in figure 2.3 [Bueno, 2009b]. The method still utilizes only 4 images, with the generator unit being set to generate circularly polarized light, corresponding to an angle of -45° on the quarter-wave plate, and the analyzer rotating through -45° , 0° , 30° , and 60° . From this, the output Stokes vector can be found and the DOP calculated using:

$$DOP = \frac{\sqrt{(S_1^2 + S_2^2 + S_3^2)}}{S_0} \quad (0 \leq DOP \leq 1) \quad (2.2)$$

Bueno et al. showed that both the DOP and S_0 images of the anterior retina show an increase in metric value over original images when assessed using entropy and SNR. When applied to retinal images, positive improvement was always shown and improvements as high as 25% for SNR and 240% for entropy were presented [Bueno, 2008]. As well as overall improvement in image quality, Bueno et al. also found that the quantitative improvement of image quality increased with age.

Using a commercially available GDx Nerve Fiber Analyzer with additional polarizing optics, and image post processing Burns et al. showed contrast improvements of subretinal features over linearly polarized images [Burns, 2003]. A half-wave plate was incorporated in front of the linearly polarized 780 nm (infrared) laser beam to act as a rotator. This allows control over the orientation of the linearly polarized beam, making it possible to sweep through all angles. 20 different images were taken through an input polarization from 0° to 90° . Two detectors were used, one with a linear polarizer set parallel to the orientation of the polarization of the system's laser and another with a linear polarizer set perpendicular to the polarization of the laser. From the crossed polarized images, a depolarized light image was constructed that improved contrast of subretinal features by 240%. The depolarized light image was created by choosing the minimum intensity at each pixel across all input polarization states for all pixels. This technique reveals a distribution map of multiply scattered light from the retina by capturing only light that has been depolarized through multiple scattering.

2.3 Determination of Metric Improvement

While all image enhancement techniques showed improvement through some image quality metric, care should be taken to make a clear definition of the reference image in techniques put forward by Bueno et al and Burns et al. Burns et al. provide specifications for their reference grayscale image, stating that all images were corrected by using offset and gain calibrations on the GDx system [Bueno, 2008], [Burns, 2003]. This implies that the reference images were stretched across the entire dynamic range of the system so that the pixel intensities ranged fully from black (0) to white (255) but is not explicitly defined. Bueno et al. do not compare their reconstructed images to reference images that had their dynamic range stretched. Within the algorithm to construct their enhanced images, images were auto-contrasted or normalized before comparison. This creates a comparison between enhanced images and reference images, resulting in an unknown amount of improvement being due to well established and simple auto-contrasting or normalization techniques as opposed to being a result of exclusively polarimetry. The two techniques put forward by Bueno et al. are revisited in chapter 4, where 11 participants are imaged using the same methods. Then, the procedure is employed a second time where the polarization images are auto-contrasted before being used with the two image enhancement techniques. The resulting images are compared to the same auto-contrasted images. This will give a true value of image quality improvement due exclusively to polarization imaging and potentially has further implications regarding age dependence.

2.4 Malaria and Polarimetry

Although the malaria parasite by-product hemozoin has been shown to be birefringent [Lawrence, 1986] and it is well known that the parasite leaves hemozoin after it consumes hemoglobin within the red blood cell [Goldberg, 1990], hemozoin has not been successfully imaged *in vivo* in the human retina.

Many groups have used polarimetry to image hemozoin in *ex-vivo* biological tissue. In 1986, Lawrence and Olson proposed the use of crossed polarization to exploit the birefringence of hemozoin found in blood smears [Lawrence, 1986]. Romagosa increased the sensitivity of malaria parasite detection from 50% to 98.1% in placenta samples when comparing standard

white light microscopy to polarization microscopy [Romagosa, 2004]. Wilson et al. combined dark-field microscopy with polarimetry using crossed-polarizers to image blood smears with the potential for automated detection [Wilson, 2011] improving hemozoin contrast in images. Dark-field microscopy, which only images the light that has scattered from the sample, has previously demonstrated its usefulness in hemozoin detection. Wood et al. combined resonance Raman microscopy with dark-field microscopy in a similar search for an automated malarial detection technique in blood smears [Wood, 2009] to exploit the Raman signal of hemozoin, which is known to be strong [Frosch, 2007]. Padial et al. have shown that depolarized light may be used as a malarial detection method in blood smears [Padial, 2005]. Hidayat et al. used polarimetry to show the presence of hemozoin within the blood vessels and at hemorrhage locations in an *in vitro* retina sample and determined that adhesion of red blood cells in blood vessels is a significant cause of retinal hemorrhage [Hidayat, 1993].

While crossed-polarization has demonstrated its ability to localize hemozoin in biological samples, the Mueller matrix of samples known to be infected with the malaria parasite has not been well studied and most polarimetry based studies have been confined to the liver, placenta, and red blood cells via blood smears. By revealing the exact polarization properties of hemozoin, better imaging techniques may be uncovered. Campbell et al. used Mueller matrix polarimetry to image human spleen samples from a malaria infected patient, determining the degree of polarization, diattenuation, and depolarization of the tissue which could lead to future imaging applications and understanding of the disease [Campbell, 2007]. The examination of hemozoin content has proven to be a useful marker for parasitization [McGready, 2002], [Sullivan, 2000]. Additionally, the number of hemozoin observed in patients has been shown to correlate well with the severity of infection [Hanschied, 2007] and is linked to micro-vascular clogging, as demonstrated through polarization spectral imaging of rectal mucosa tissue by Dondorp et al. [Dondorp, 2008]. Furthermore, as the technology inevitably becomes more compact, *In vivo* hemozoin measurement could lead to a quick and non-invasive method for detection of medium to late stage cerebral malaria infection if detected using scanning laser polarimetry in the retinal blood vessels.

The retina provides a window into the vasculature of the nervous system. Observation of pathologies of the retina has also recently been reported as a useful diagnostic tool for severe

cerebral malaria infections. Retinopathy due to severe malaria has a unique set of abnormalities that may be observed using ophthalmoscopy [Beare, 2006] White et al. found that for children with malaria, the severity of retinal hemorrhages was a good indication of the severity of hemorrhage within the brain [White, 2001], which may be the root cause of coma and death although this has not been conclusively determined [White, 2009]. Beare et al. showed significant correlation between malaria related changes in the retina and coma resulting in death in children [Beare, 2004] White et al also state that knowing the severity of the cerebral infection may lead to better, more personalized treatment plans [White, 2001]. Careful retinal imaging of pathology has provided evidence for retinal ischemia in cerebral malaria patients and has led to the suggestion to apply known treatments to decrease perfusion of tissue to combat the effects of the disease [Beare, 2009]. Diagnosing retinopathy can also play a role in reducing the misdiagnosis of coma. Taylor et al. found that 23% of 31 clinically diagnosed cerebral malaria related deaths were actually due to other causes [Taylor, 2004]. Retinopathy observation provided the only differentiating features between malarial and non-malarial deaths. While retinopathy related to malaria has been researched extensively in children in the above studies, it has not been studied very thoroughly for adults [Maude, 2009].

The need for further study of the properties and role of hemozoin in malaria infection as well as improvement in imaging techniques is evident. Since image quality enhancements have also been demonstrated using polarization (as discussed in section 2.2), polarimetry may be a valuable tool for not only the examination of hemozoin, but the diagnosis of cerebral malaria from the point of view of better visualization of the associated retinopathy.

Chapter 3 - Improvements in image acquisition and image processing

3.1 Overview

Images were captured using a CSLO. Image acquisition speed was increased by the incorporation of stepper motors to semi-automate the rotation of polarizing optics within a CSLO imaging system. Fourier transform based edge detection filters were applied to images to improve the success rate of registration. With the semi-automated optics, the acquisition time was greatly reduced and the displacement and rotation of images relative to each other was also reduced but not significantly, decreasing time for registration for some participants but not significantly across participants. Translation was only reduced for 2 of 3 participants while rotation was reduced for all 3. Edge detection filters greatly increased registration success rate. This increase in success rate not only reduces the time it takes to register sets of images because fewer errors need to be corrected, but also could help registration algorithms register images that previously could not be registered and allow polarimetry to be performed on previously unusable samples.

Some of the images (see Table 1) used to develop the improved image registration techniques described in this chapter, were originally acquired for the purpose of characterizing image quality, and used by Hunter for her PhD thesis [Hunter, 2006] and in the following paper [Hunter 2007] which was written by Hunter in collaboration with myself, Marsha Kisilak, Juan Bueno, and Melanie Campbell. Other images were acquired for the purpose of improving image quality and a subset of the participants' results were published in Bueno (2007). A third set of foveal images were taken as a function of pinhole size and are unpublished. These images are used exclusively in this chapter for the purpose of testing registration methods. For all image acquisition, I operated the recording computer and provided guidance for the positioning of imaging on the retina. I also operated the analyzer unit on the CSLO when used. Once acquired, I processed (averaged and registered) the images and organized the data and images for the published analysis. In this thesis, I outline for the first time, the improvements given in that data by automation of the polarimetric acquisition. The edge detection filters are used for the first time in this thesis and were not used in the study performed by Hunter et al (2007).

3.2 Introduction

Registration of images is a crucial step in polarimetric imaging of the retina because images of varying polarization must be aligned to produce the Mueller matrix. A variety of approaches have been used in an attempt to improve success rates of registration for polarized and low quality images. Zheng et al. used a feature-based approach to register poor quality images from diseased retinas, isolating large features and registering them together using a local transformation algorithm [Zheng, 2005]. Guyot et al. used gradient-based techniques to correct for distortion in Mueller matrix polarimetry created by unavoidable motions, like seen in *in vivo* imaging of the human eye [Guyot, 2006].

Registration of polarimetric images can be particularly difficult because the different visible features of the retina change uniquely under the many possible states of polarized light causing the images to correlate poorly. Polarimetric images also no longer have constant brightness from image to image. The success rate for registration of our polarized images using a cross-correlation algorithm depends on the participant and polarization settings but is well below 100%. In this chapter, I will show how the success rate for registration of polarized retinal images can be greatly improved using Canny edge detection maps and other Fourier transform techniques. This can significantly reduce image processing time because images that fail to register must be replaced and re-registered.

The acquisition of polarization images in our CSLO is time consuming because the polarizing optics must be manually set and changed for up to 16 image sets. This increases participant discomfort due to longer imaging sessions. Reduced imaging times are also desirable because they may also decrease registration times by reducing eye drift and rotation. Cherici et al demonstrated that it is difficult for humans to achieve accurate, prolonged fixation [Cherici, 2012]. I will show how the introduction of automated polarizers can greatly speed up the acquisition process of *in vivo* imaging using a CSLO and also reduce registration time due to faster image acquisition potentially decreasing drift and rotation of the eye.

3.3 The Waterloo CSLO

The instrument used to obtain images of the optic nerve head and surrounding tissue is the Waterloo CSLO (figure 3.1). A spinning polygon mirror is used to scan in the horizontal

direction, while a galvanometer is used to scan in the vertical direction. The scan is similar to that of a cathode ray tube television or monitor and sweeps out a square corresponding to the area being imaged (known as a raster scan). The laser enters the eye's optics and at its focal point, scans the back of the eye. The plane imaged can be adjusted optically. After the laser light reflects from the retina, the de-scanned light passes through a confocal pinhole and into a photomultiplier tube where it is digitally recorded via the CSLO console at 28.5 frames per second. The best frames may be chosen from the resulting video and used for analysis.

The confocal pinhole in the CSLO excludes out scattered and defocused light, ensuring that the image is mostly formed by the light that originates from the image point on the retina. This is known as optical slicing because this effectively makes the CSLO image a two dimensional slice that is perpendicular to the incoming beam.

When imaging using polarized light, the beam first passes through a generator. The generator is an optical element consisting of a linear polarizer followed by a quarter-wave plate. By rotating the quarter wave plate, the generator allows control over the input Stokes vector incident on the eye. An analyzer may also be placed into the exit path of the laser after it reflects off the retina. The analyzer consists of a quarter-wave plate followed by a linear polarizer. By rotating the quarter wave plate, the analyzer reads a particular output Stokes vector after interaction of the light with the human eye. Analyzer and generator quarter wave plate angles were precisely controlled using a stepper motor system controlled through a GUI.

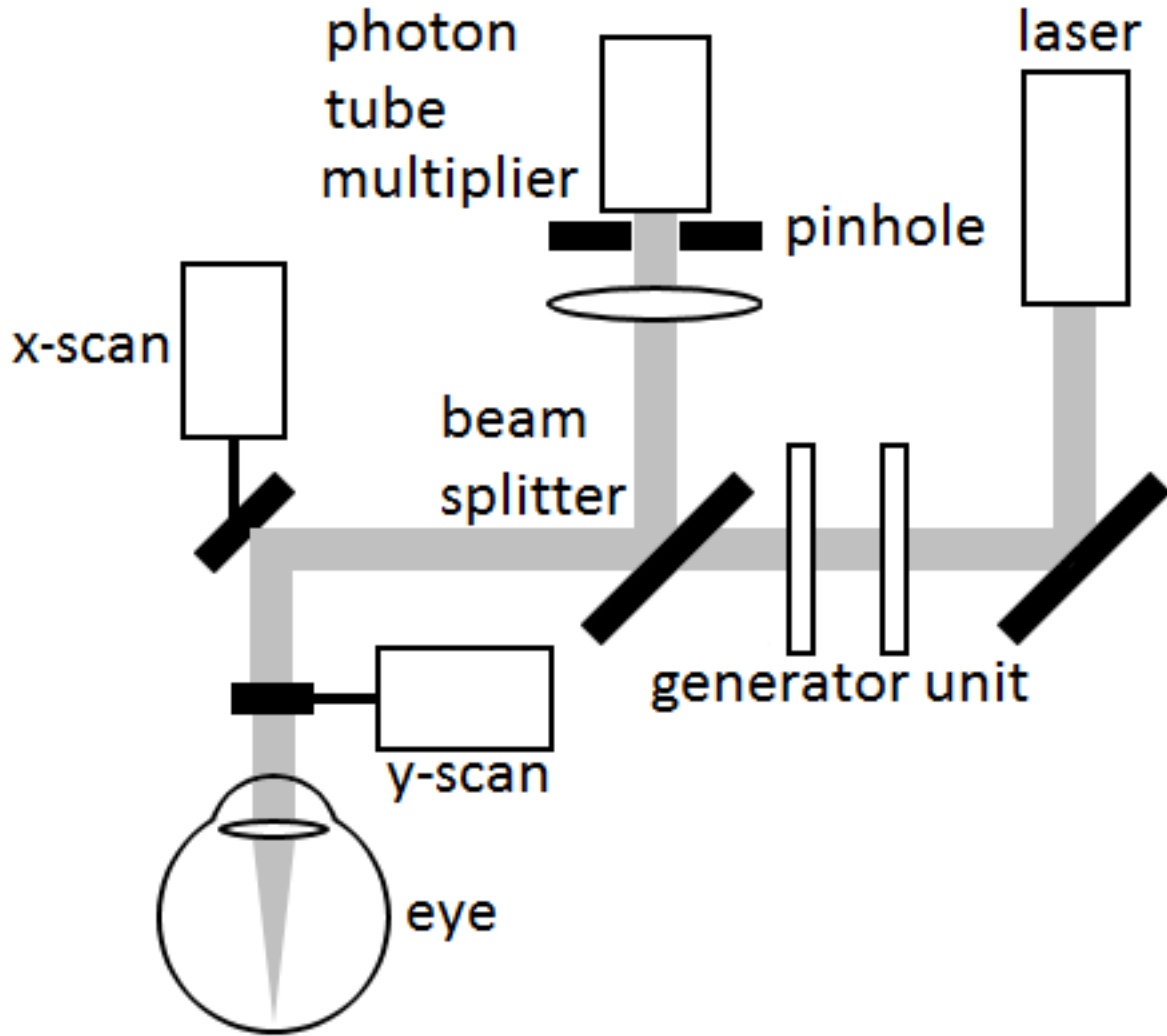


Figure 3.1: CLSO with a generator incorporated into the system.

The 633 nm HeNe laser’s power level was adjusted to a safe level according to the American National Standards Institute (ANSI) [ANSI, 2000]. The maximum laser power level used was approximately ten times below the maximum level allowed by ANSI, a power level of 150 μW at the cornea. The power was kept constant throughout the experiment for a given participant. For each participant, the power level was adjusted slightly to maximize image brightness while not exceeding the dynamic range of the imaging system when cycling through quarter-wave plate positions.

Additionally, lenses were sometimes used directly in front of the eye to vary the depth of the optic nerve head imaged or to sharply focus the fovea. Finally, a fixation target consisting of a

bright yellow LED and a magnet on a white board was used to cause rotation of the participant's eye so that the desired location of either the fovea or the ONH was imaged.

3.4 Methods

Various data sets of retinal images taken for different studies were used to test the success rate of registration using Fourier transform techniques. These sets provide a wide variety of changes to the illumination of the retina, which is essential for robust testing of the registration software. This research received ethics clearance from the University of Waterloo Office of Research Ethics. Participants were adults with normal ocular health, refractive sphere between +5.5D and -7.25D and cylinder less than 1.25D whose fundus imaging was performed for a number of studies (Table 1).

For various data sets (Table 1), two main features of the human eye were imaged using the Waterloo CSLO, the ONH and fovea, and their surrounding nerve fibre layer was recorded in a 15° field (figure 3.2).

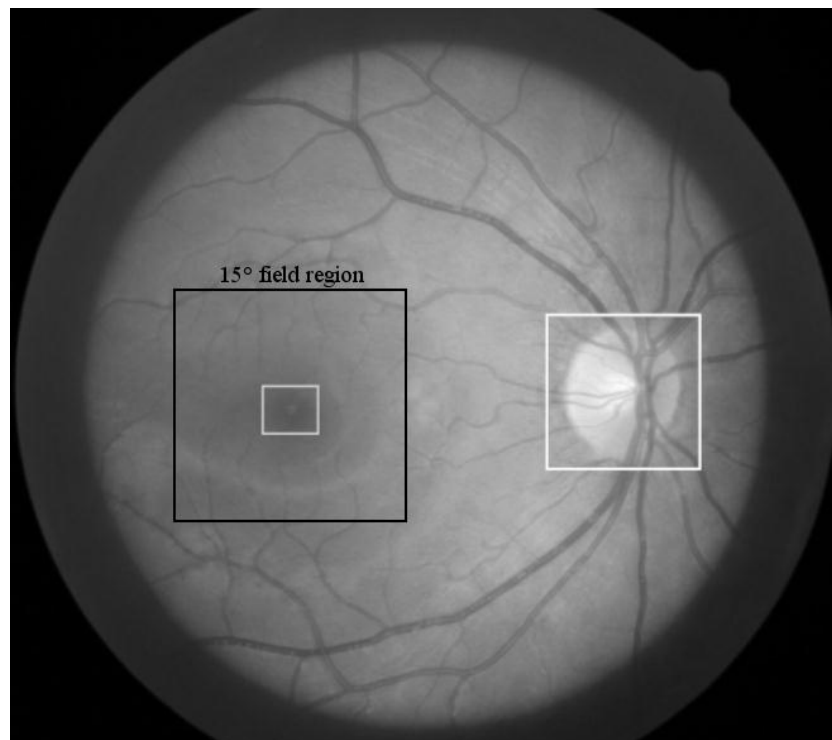


Figure 3.2: The ONH (right white square), fovea of the human eye (left white square), and 15° imaging window (black square).

In some images, the input polarization state was controlled by rotating the quarter-wave plate on the generator through -45° , 0° , 30° , and 60° with respect to the vertical axis of the linear polarizer, yielding 4 different configurations. Different incident polarization states resulted in varying brightness and contrast in the resulting images (figure 3.3).

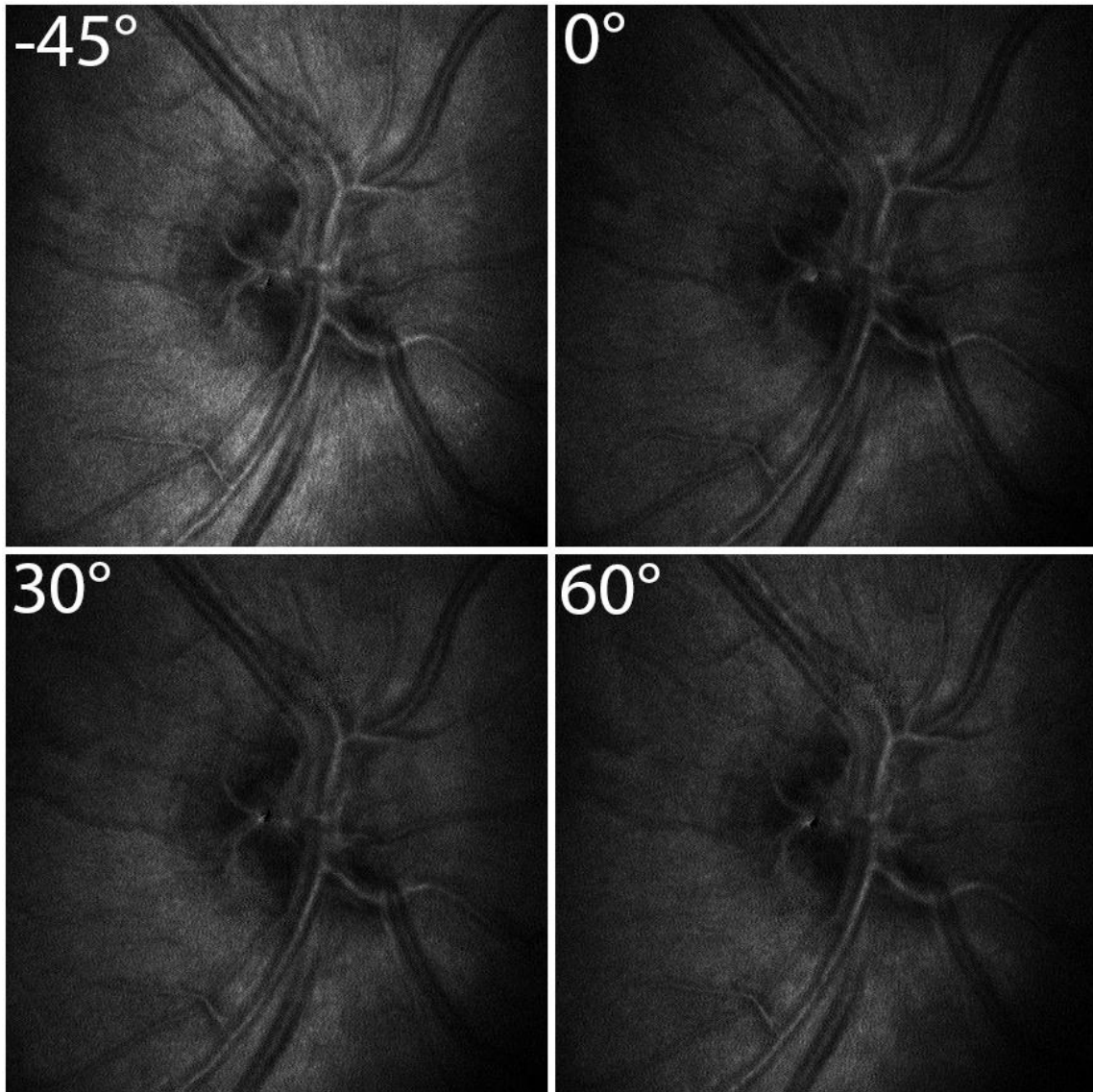


Figure 3.3: RNFL of a participant taken with incident polarized light produced by the 4 different positions of the generator unit.

The four states of polarized light incident on the eye correspond to linearly independent polarization states of circularly, linearly, elliptically, and elliptically polarized light for each rotation of the quarter wave plate [Bueno, 2002].

In other images (Table 1), the lens in front of the eye was changed to focus on the retinal nerve fiber layer (RNFL), then midway down the optic nerve head and/or on the lamina cribrosa (LC).

Number of Participants	Area Imaged	Confocal Pinhole Size (μ)	Number of Focal Positions	Number of Polarization Settings	Images Acquired For
3	ONH	100, 200, 400, 600	3	1	Hunter (2006), Hunter (2007)
6	ONH	400	2	4	Bueno (2007)
5	fovea	100, 200, 400, 600	1	1	Not previously published
11	ONH	400	2	8	Chapter 4

Table 3.1: Participant source and imaging conditions.

Finally, in some images (Table 1), the diameter of the confocal pinhole was adjusted through four different sizes: 100 μ m, 200 μ m, 400 μ m, and 600 μ m.

For 3 participants from Hunter et al (2007) (Table 1), 12 CSLO recordings of the ONH were acquired that corresponded to the 12 possible different configurations of confocal pinhole and lens (See Table 1). From each of these 12 recordings, 8 good quality images were chosen with a centered ONH and averaged together to produce 1 averaged image from each recording (36 images in total across 3 participants). One reference image was chosen to which the remaining 11 images were registered (33 registration attempts in total). Reference images were chosen as the most centered image between all images to be registered. If several appropriate images were available, the brightest image was used.

For 6 participants, (4 of which are described in Bueno, 2007), 8 CSLO recordings of the ONH were acquired that corresponded to the 4 possible configurations of input polarization state and two lens focus positions (-0.5 D and 0.5 D) with a constant confocal pinhole of 400 μ m (see

Table 1). From each of these 8 recordings, 8 good quality images were chosen with a centered ONH and averaged together to produce 1 image from each recording (48 images in total over 6 participants). From these 8 images, 1 reference image was chosen to which the remaining 7 images were registered (42 registration attempts in total).

With no polarizers in place, 4 CSLO recordings of the fovea and surrounding area were acquired for each of the 5 participants that pertained to 4 different confocal pinhole sizes. 8 good quality images were chosen with a centered ONH and averaged together to produce 1 image from each recording and, from these 4 images, 1 reference image was chosen to which the remaining 3 images were registered (15 registration attempts in total). For details on why these specific settings of pinhole, lenses, and polarization configurations were originally chosen, see Hunter [2006]. These images were reused to test differing registration processes across many different imaging conditions, giving a diverse selection of images.

I acquired an additional set of images which is the same data used to compare polarization image enhancement methods in Chapter 4 involving 11 participants. The ONH and surrounding area were recorded at two depths (RNFL and LC). The pinhole was kept constant at 400 μm . For each of the 11 participants, the input polarization state was set to generate circularly polarized light with a quarter wave plate angle of -45° relative to the generator's linear polarizer. The output polarization state was read with an analyzer rotated through -45° , 0° , 30° , and 60° with respect to the vertical axis of the linear polarizer. From each of the 8 recordings acquired, 8 good quality images were chosen (88 in total across 11 participants). From these 8 images, 2 reference images were chosen (1 corresponding to each depth) to which the 6 remaining were registered (66 registration attempts in total). Then, with only the generator in place, the quarter-wave plate was rotated through -45° , 0° , 30° , and 60° with respect to the vertical axis of the linear polarizer again for 2 depths. From these 8 images, 2 reference images were chosen (1 corresponding to each depth) to which the 6 remaining were registered (66 registration attempts in total).

Images are also acquired of the CSLO background, recording only the noise produced by the imaging system, including lens reflections and complex noise were recorded at locations and settings corresponding to each of the imaging conditions described in each imaging session. This is mainly done to remove the static lens reflections that obscure the view of the sample and, if

bright, can affect auto-contrasting by giving a false ceiling to the pixel values. Eight background images are averaged together and subtracted from their corresponding retinal images.

3.4.1 Analyzer and Generator Automation

Stepper motors were custom fit to rotating polarizer stages. Matlab software, which sent signals to a stepper motor control board via the parallel port, controlled the orientation of the quarter wave-plates in the generator unit in all polarized light experiments used in the second set of images for this work. The motors were controlled through a custom Matlab GUI that allowed control over motor 1, motor 2, or both motors simultaneously (figure 3.4).

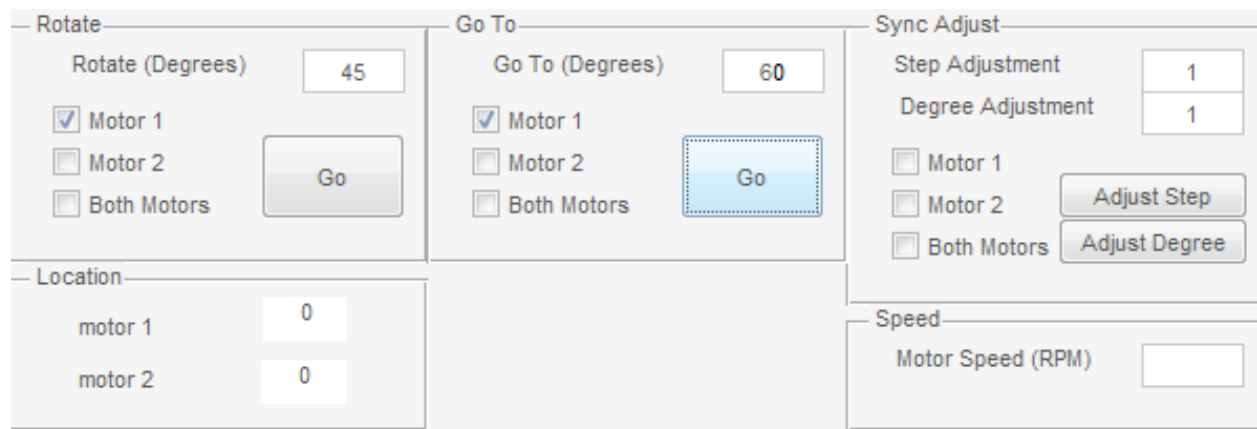


Figure 3.4: Stepper motor GUI used to control positions of quarter wave plates in both the analyzer and generator unit within the CSLO.

The position could be rotated to a specific location using the “Go To” function, anywhere between 0 and 359 degrees. The “Rotate” function was used to move the quarter wave-plates any number of degrees from their current location, which can be seen in the “Location” read out. The stepper motors could not be moved exactly one degree because the small discrete step of the motors was not a multiple of 1 degree. To compensate for this, the “Sync Adjust” function could be used to adjust the motor by any number of its smallest possible steps because 14 steps approximated but did not exactly equal one degree.

The motor driven quarter wave-plates took 10 complete revolutions to become out of sync by 1 degree. For each participant, the most each motor moved through was only 105°. The

misalignment was negligible at only $3/100^{\text{th}}$ of a degree out of sync when sweeping through all 4 positions: -45° , 0° , 30° , and 60° . Alignment of quarter-wave plates was checked after each participant by observing the alignment by eye using the ruler markings on the polarizing optics.

For 3 of the 11 participants, experiments were repeated without the use of the stepper motors, moving the quarter wave plates by hand. The time taken to perform the experiment with and without the use of stepper motors was recorded. During registration, the rotational and translational misalignment was recorded and compared for stepper motor and manually driven polarization optics.

3.4.2 Illumination variance

Due to curvature on the retina, the surface being imaged is not totally flat. This, coupled with uneven illumination from the CSLO itself, imposes illumination variance across the image, particularly around the edge of the images. Illumination variance can be treated as a type of multiplicative noise across the whole image. To cope with this problem, two illumination variance correction techniques were employed to normalize the variance. A homomorphic filtering approach was taken which is known to reduce multiplicative noise in image processing [Lowell, 2004]. Homomorphic filtering is a non-linear mapping technique that normalizes brightness and increases contrast. The second approach taken was an histogram equalization.



Figure 3.5: Original image $P_f(r)$ (left) and the corresponding image following histogram equalization $T(r)$ (right).

This process applied a transform to the histogram of an image so that, ideally, each pixel's intensity has the same chance of occurring. This was done by finding the cumulative density function (CDF) of the histogram and using this as the transform for the same histogram. Consider the original histogram of an image (figure 3.5), $P_f(r)$ where r is the intensity level. We can find the desired transform, $T(r)$, using:

$$T(r) = \int_0^r P_f(r) dr \quad (3.1)$$

This method was employed to give the edge detectors higher contrast edges with which to work.

3.4.3 Image Filters

Low pass filters were also initially used to smooth out noise so edge detecting filters do not pick up the noise as a small edge. However, this comes with a trade off as edges are also blurred while being crucial for accurate edge detection. Three edge detectors were compared in this approach: the Sobel edge detector, a high pass filter with a cut off of 20 Hz for 502 pixel by 502

pixel images (which removes non-edges, effectively acting as an edge detector) and finally, the Canny edge detector.

Taking the Fourier transform (equation 3.2) of an image puts the image into the frequency domain where low frequencies are near the center of the image and the frequencies get higher as you move away from the center to the edge. In the high pass filter edge detection method, by blocking out the low frequencies using a Gaussian filter, smoother regions are taken out, leaving only higher frequency components, such as edges and noise (figure 3.6).

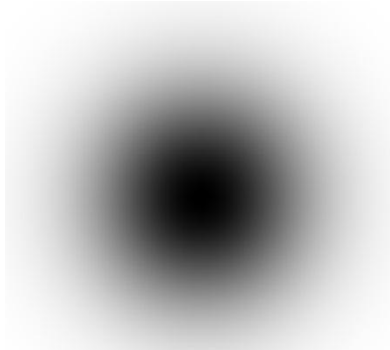


Figure 3.6: A Gaussian high-pass filter removes low frequencies in the frequency domain enhancing edges and noise.

A smooth Gaussian filter must be used or unwanted artifacts will appear on the image, reducing the usability of results. The size of the Gaussian filter will affect the strength of the subsequent edge sharpening. After applying the high pass filter, $H(x,y)$, the result, $g(x,y)$, can be seen by simply taking the inverse Fourier transform (3.3).

$$F(u, v) = \int_{-\infty}^{\infty} \int_{-\infty}^{\infty} f(x, y) e^{-j2\pi(ux+vy)} dx dy \quad (3.2)$$

$$f(x, y) = \int_{-\infty}^{\infty} \int_{-\infty}^{\infty} F(u, v) e^{j2\pi(ux+vy)} du dv \quad (3.3)$$

$$g(x, y) = IFT[FT[f(x, y)] \circ H(x, y)] \quad (3.4)$$

For my initial processing, a low pass filter, $L(x, y)$, was applied in place of the high pass filter (figure 3.7). This removed the high frequencies component of the image, reducing noise and edge contrast. The larger the filter, the stronger the blur applied to the image.

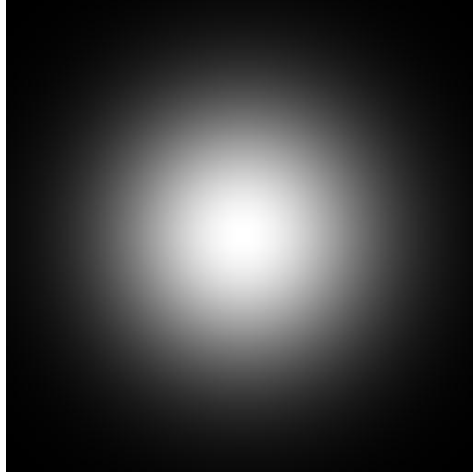


Figure 3.7: A Gaussian low-pass filter removes high frequencies in the frequency domain smoothing the image.

The Sobel edge detector works by finding the gradient of image intensity in the x and y directions. Each direction corresponds to a simple filter, ∇_x and ∇_y , and they are used to calculate the final image, S_f .

$$\nabla_x = \begin{bmatrix} -1 & 0 & 1 \\ -2 & 0 & 2 \\ -1 & 0 & 1 \end{bmatrix} \quad (3.5a)$$

$$\nabla_y = \begin{bmatrix} 1 & 2 & 1 \\ 0 & 0 & 0 \\ -1 & -2 & -1 \end{bmatrix} \quad (3.5b)$$

$$S_f = \sqrt{\nabla_x^2 + \nabla_y^2} \quad (3.6)$$

Finally, the Canny edge detector works in three stages. First, the image is run through a Gaussian filter (3.7), (3.8) to smooth edges.

$$f_\sigma(x, y) = f(x, y) * g_\sigma(x, y) \quad (3.7)$$

$$\text{where } g_{\sigma}(x, y) = \frac{1}{2\pi\sigma^2} \exp\left(-\frac{x^2 + y^2}{2\sigma^2}\right) \quad (3.8)$$

The x and y components of the gradient of the smoothed function can then be found (3.9), (3.10), (3.11).

$$\nabla f_{\sigma}(x, y) = (f * \nabla g_{\sigma}) \quad (3.9)$$

$$\nabla_x f_{\sigma}(x, y) = \left(f * \frac{\partial g_{\sigma}}{\partial x} \right) \quad (3.10)$$

$$\nabla_y f_{\sigma}(x, y) = \left(f * \frac{\partial g_{\sigma}}{\partial y} \right) \quad (3.11)$$

Finally, the edge gradient and direction can be found using (3.12), (3.13), respectively.

$$M_{\sigma}(x, y) = \sqrt{(\nabla_x f_{\sigma}(x, y))^2 + (\nabla_y f_{\sigma}(x, y))^2} \quad (3.12)$$

$$\theta_{\sigma}(x, y) = \arctan\left(\frac{\nabla_y f_{\sigma}(x, y)}{\nabla_x f_{\sigma}(x, y)}\right) \quad (3.13)$$

Then, an upper and lower threshold is chosen to locate the edges. Local maxima, found above the upper threshold value, on the gradient magnitude along different orientations are used as strong edge locations. If the gradient magnitude of an adjacent pixel at these locations is higher than the lower threshold, it is turned into an edge. The algorithm searches in the Canny method until all edges are located helping to reduce the number of false edge locations being turned into edges [Grigorescu, 2004].

3.4.4 Application of Filters

Many combinations of illumination variance correction, low pass filters, and edge detection filters were used in conjunction to find best filter combination for registration. This represents a chain of three filters used one after the other. A general approach was taken to each image to be registered and was also applied to the reference image. First, an illumination variance correction technique was applied, followed by a low pass filter to reduce the increase in noise due to the

application of the illumination variance correction. Then, an edge detection algorithm was applied to find the presumably enhanced edges with other unnecessary information removed so the images could be registered more easily. The cut off frequency used in the application of the low pass filter was changed in steps of 5 Hz. Note that a cut off frequency of 0 is equivalent to removing the low pass filter from the chain. Incremental steps were used with the cut off frequency in the low pass filter to minimize processing time since many different combinations are possible and registration of images is a time consuming process. Tests were also done with the illumination variance correction removed because it both enhanced the edges and increased noise in the image so it was difficult to know whether it was a benefit or detriment to the edge detection filter (figure 3.8).

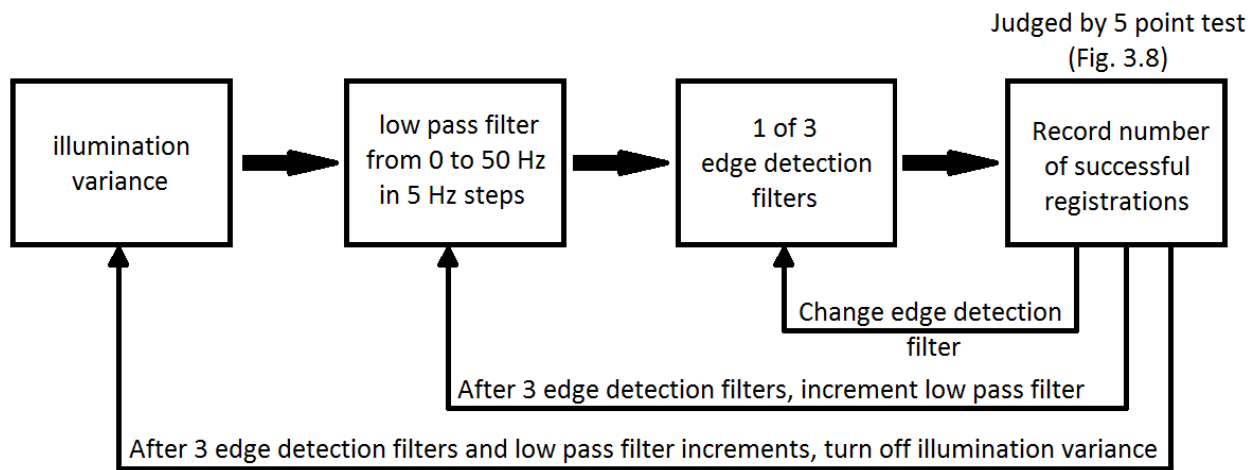


Figure 3.8: Flowchart demonstrating method for testing filter chains in the competition for highest registration success rate.

Due to extremely long image processing times for registration, all possible combinations of filters could not be applied to all of the images. A smaller set of images was used to narrow down the best filter combination for each type of edge detection. The best of each was then applied to all images. Filter combinations were judged by the number of images they successfully registered.

3.4.5 Registration

Image registration can be a very slow process if the displacement and rotational misalignment of the images to be matched is large. For the process, a reference image must be chosen to which the rest of the images in a set are aligned. When possible, the reference image was always chosen as the image corresponding to a pinhole of 400 μm and no lens. A 400 μm pinhole was found to be the best tradeoff for brightness and image quality [Hunter, 2006]. When polarization was varied, the brightest image from the 4 input polarization states was chosen. Images (after application of the filter series being tested) were rotated and translated over a large area in many small steps and the cross-correlation between each image was calculated. The amount of translation and rotation varies from image to image because no subject can always fixate in the exact same spot even with a fixation target used in these experiments [Cherici, 2012]. To ensure the images are overlapped by rotation and translation, they had to be rotated through 1.5° in both clockwise and counterclockwise directions by steps of 0.1° and stepped through 40 pixels in $\pm x$ and $\pm y$ directions by steps of 1 pixel. This would move through an area of 81 by 81 pixels. An angle of 1.5° and 81 by 81 pixels were chosen because they were the maximum observed values of misalignment of past images. For each step, the correlation function was calculated and the position yielding the maximum cross-correlation value was taken as the registered image. The cross-correlation between two images, s and f , is defined as

$$R_{sf}(\gamma) = \int s(x)f(x+\gamma)dx \quad (3.14)$$

$$\text{where } 0 \leq R_{sf}(\lambda) \leq 1$$

If this value, R_{sf} , equals 1, then the images are perfectly correlated. This special case would only occur for two identical images. Likewise, if the value is 0, the images are not correlated at all. The highest correlation was used by the algorithm to choose the most aligned image during the registration process.

3.4.6 Judging Successful Registration

To ensure each image is registered to its reference image, five landmarks were chosen on the reference image; one point along each edge and one in the center (figure 3.9). Landmarks have been exaggerated for easy viewing. All landmarks were always chosen to be vessel edge and intersections. Images were auto-contrasted to enable maximum visibility during judgment.

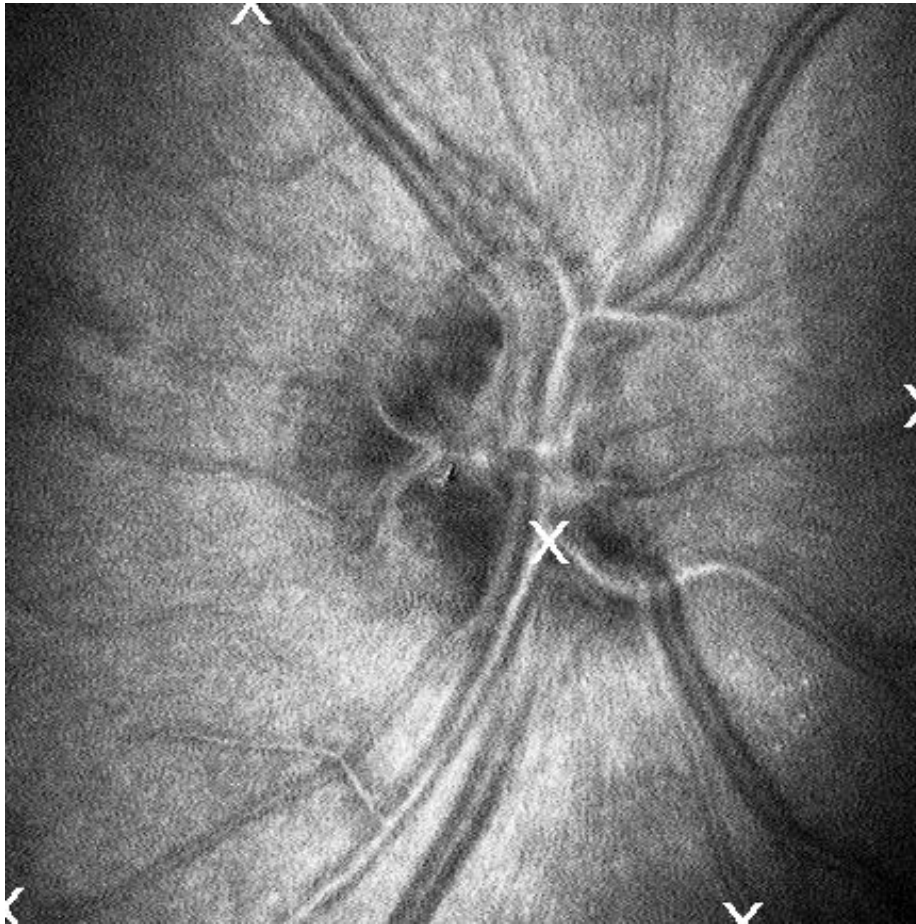


Figure 3.9: Reference image with five chosen landmarks.

If each point showed no translation in any direction, the image is considered registered. Using a computer, images were overlapped for ideal viewing of landmark positions. Whether a registration was successfully was only based on this judgment method and not based on any correlation value found by the registration algorithm during processing.

3.5 Results

3.5.1 Analyzer and Generator Automation

Over 3 participants, acquisition times were 4.9 times faster using the stepper motors to drive the rotation of the quarter wave plate versus movement by hand. Experimental time was significantly reduced by an average of 80% from an average of $519 \text{ s} \pm 26 \text{ SD}$ to $104 \text{ s} \pm 6 \text{ SD}$ ($p = 0.0008$, paired t-test). Figure 3.10 shows experiment time lapse for participant 1, 2, and 3 with manually rotated quarter wave plates shown in blue and motor driven in red.

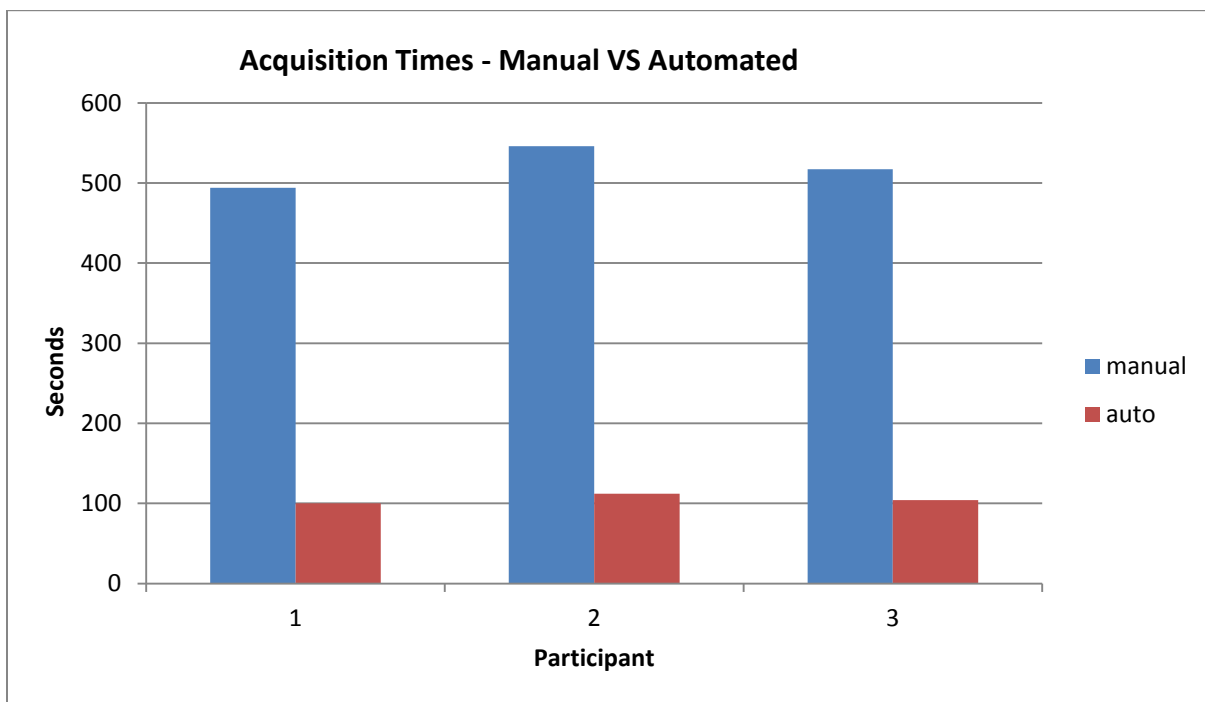


Figure 3.10: Acquisition times were reduced significantly with automated rotation of the polarizing optics.

Registration times were also reduced by an average of 1.7 times although this reduction was not significant. It reduced from $49 \text{ s} \pm 27 \text{ SD}$ to $28 \text{ s} \pm 11 \text{ SD}$ ($p = 0.18$, power < 0.8 , paired t-test) Average total time for the registration of the 3 polarization images to the chosen reference image can be seen in figure 3.11.

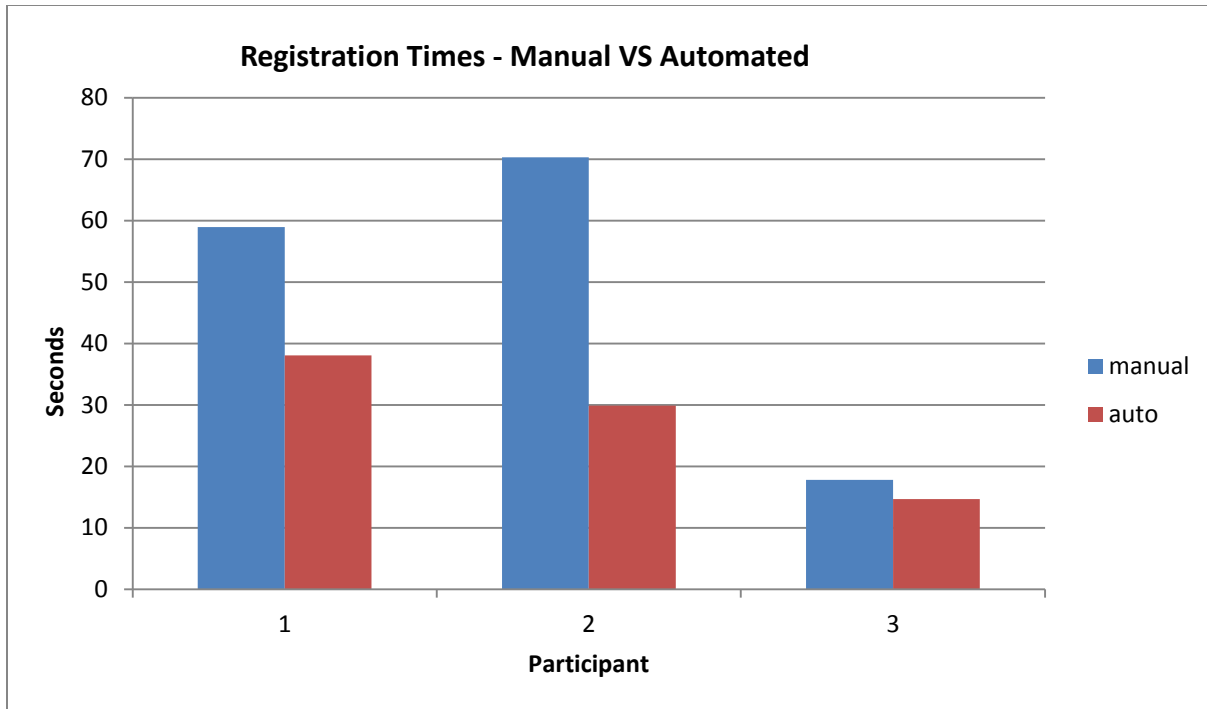


Figure 3.11: Registration times were reduced with automated rotation of the polarizing optics. Averages are taken across the three images registered for each of 3 participants.

Over 3 CSLO images, the average misalignment of rotation and translation between images before registration was found with respect to the original image for each subject (Table 3.2).

Participant	Translation (pixels)		Rotation (degrees)	
	Manual filter adjustment	Auto filter adjustment	Manual filter adjustment	Auto filter adjustment
1	8.5	6.8	0.53	0.47
2	10.6	8.3	0.47	0.30
3	8.1	8.8	0.30	0.10

Table 3.2: Average translation and rotation over 3 images for polarizing optics.

A reduction for translation (figure 3.12) was seen in 2 of 3 participants with a mean reduction of 1 pixels from an average of 9 pixels \pm 1 SD to 8 pixels \pm 1 SD ($p = 0.34$, paired t-test). Rotation was reduced for all participants with a mean reduction of 0.14° from an average of 0.4°

± 0.1 SD to $0.3^\circ \pm 0.2$ SD ($p = 0.07$, paired t-test) (figure 3.13). However, the power of this test was not high. In order to reach a power of 0.8, the sample size is estimated at 16 participants.

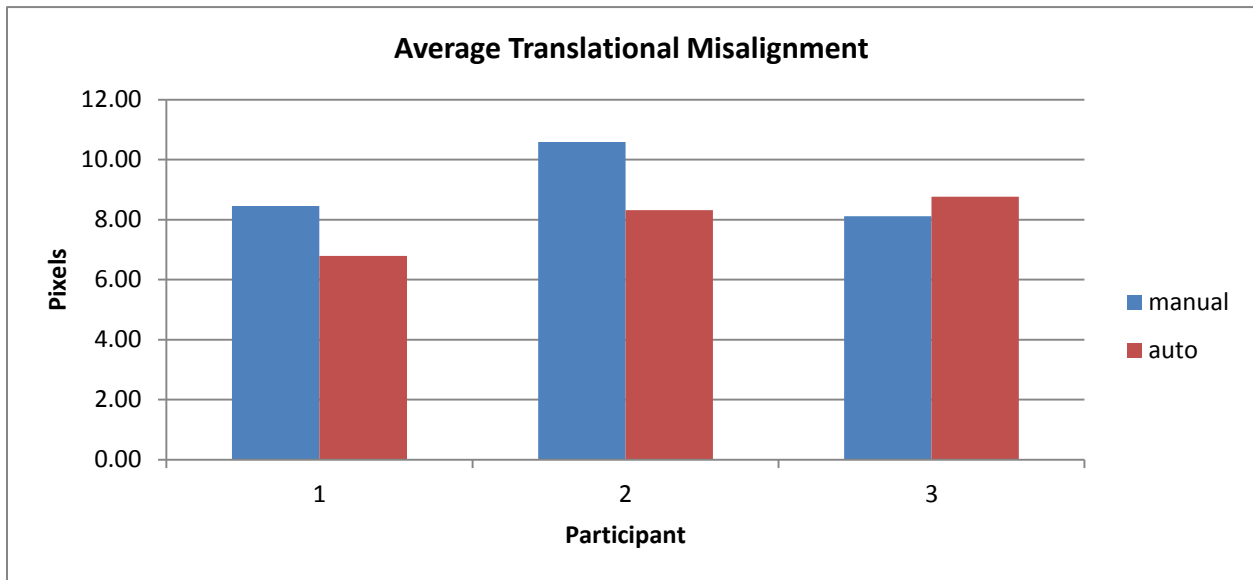


Figure 3.12: Average translation misalignment using automated and manually driven polarizing optics.

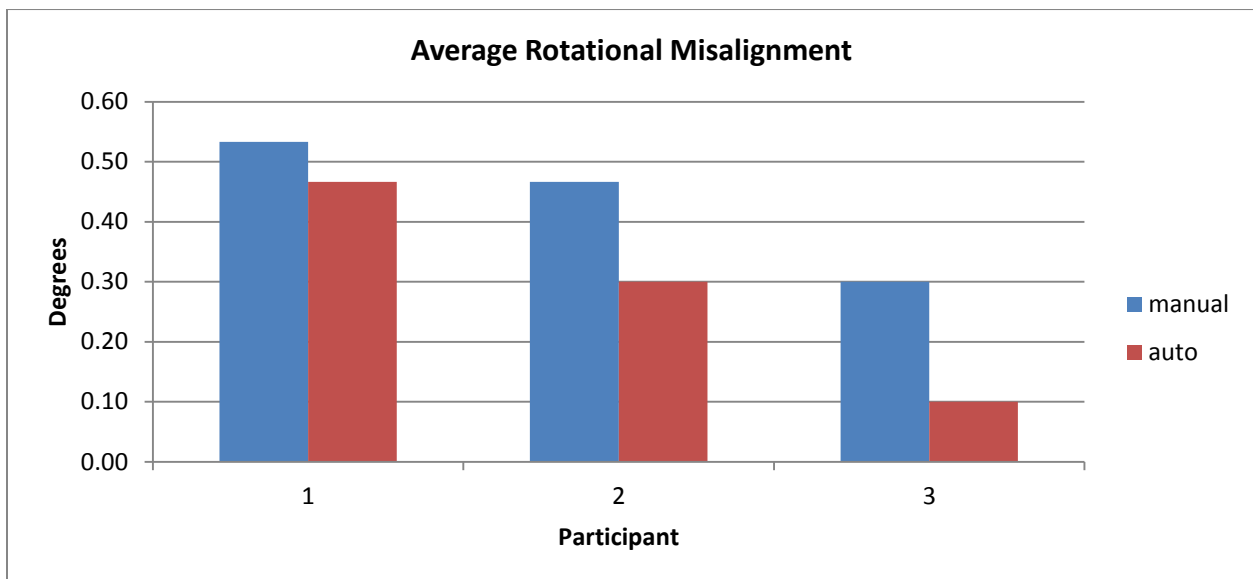


Figure 3.13: Average rotation misalignment using automated and manually driven polarizing optics.

3.5.2 Frame Averaging

Images acquired with the CSLO contain some noise due to the detector. In addition, the coherent laser produces laser speckle and the noise characteristics are further complicated by the raster scan of the system [Hunter, 2006]. To reduce additive noise and improve image quality, all images registered are first frame averaged. After acquiring each recording from the CSLO, eight images of very similar location and with the same experimental conditions were chosen, registered and averaged. The effects of frame averaging to reduce noise has been well documented [Castleman, 1996]. The optimal number of images when trying to balance image quality with increased difficulty of alignment due to eye movements was found to be 8 images [Hunter, 2006]. Since the 8 images to be averaged are in almost the same location and are nearly identical to each other, registration with no edge detection is fast and completely reliable.

As a quantitative measure of the improvement, we can measure the signal to noise ratio (SNR) of the images before and after averaging (figure 3.14). For a complete description of SNR, see section 4.3.5.

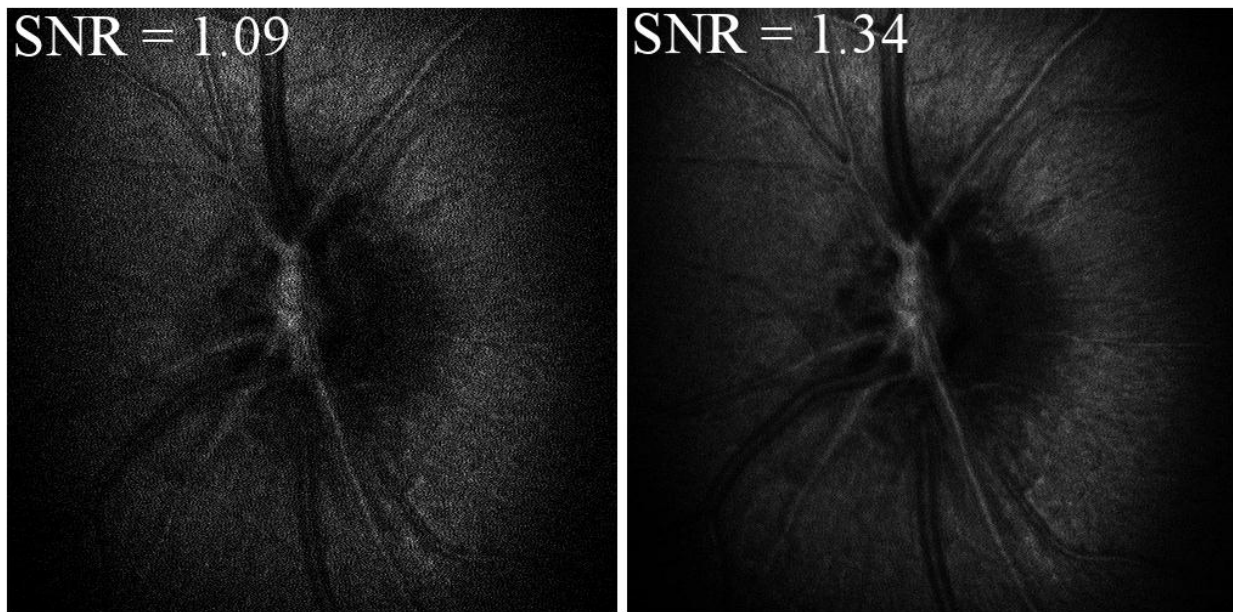


Figure 3.14: Average of 8 images (right) shows a marked improvement in the signal-to-noise over original image (left) ratio.

3.5.3 Illumination variance

Homomorphic techniques failed to produce desirable results for image quality improvement (figure 3.15). Homomorphic techniques normalized illumination very well but introduced artifacts and smoothed the vessel edges, which is the most important feature in registration. Vessel edges are consistently present in all images and a strong edge is necessary for edge detection filters.

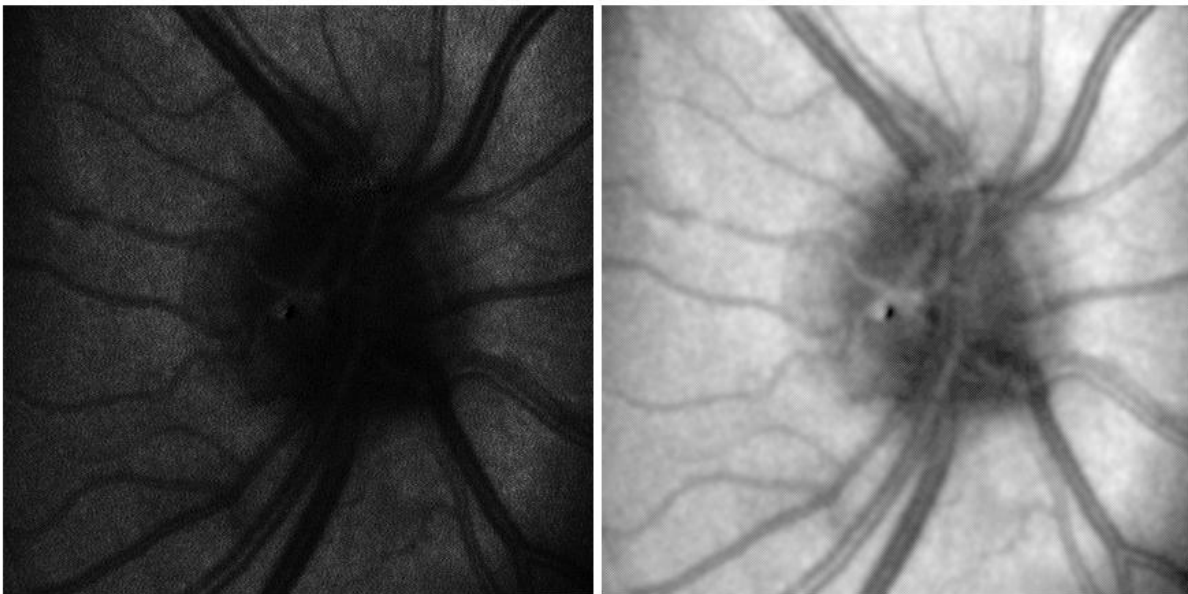


Figure 3.15: 400 μ pinhole CSLO image (left) and image with illumination correction using homomorphic techniques (right).

The second approach taken to deal with this variation was histogram equalization. The resulting images show a significant improvement in uniformity of illumination across images. As figure 3.16 shows, the vessels in the images, especially in the 100 micron pinhole image, are much brighter than before.

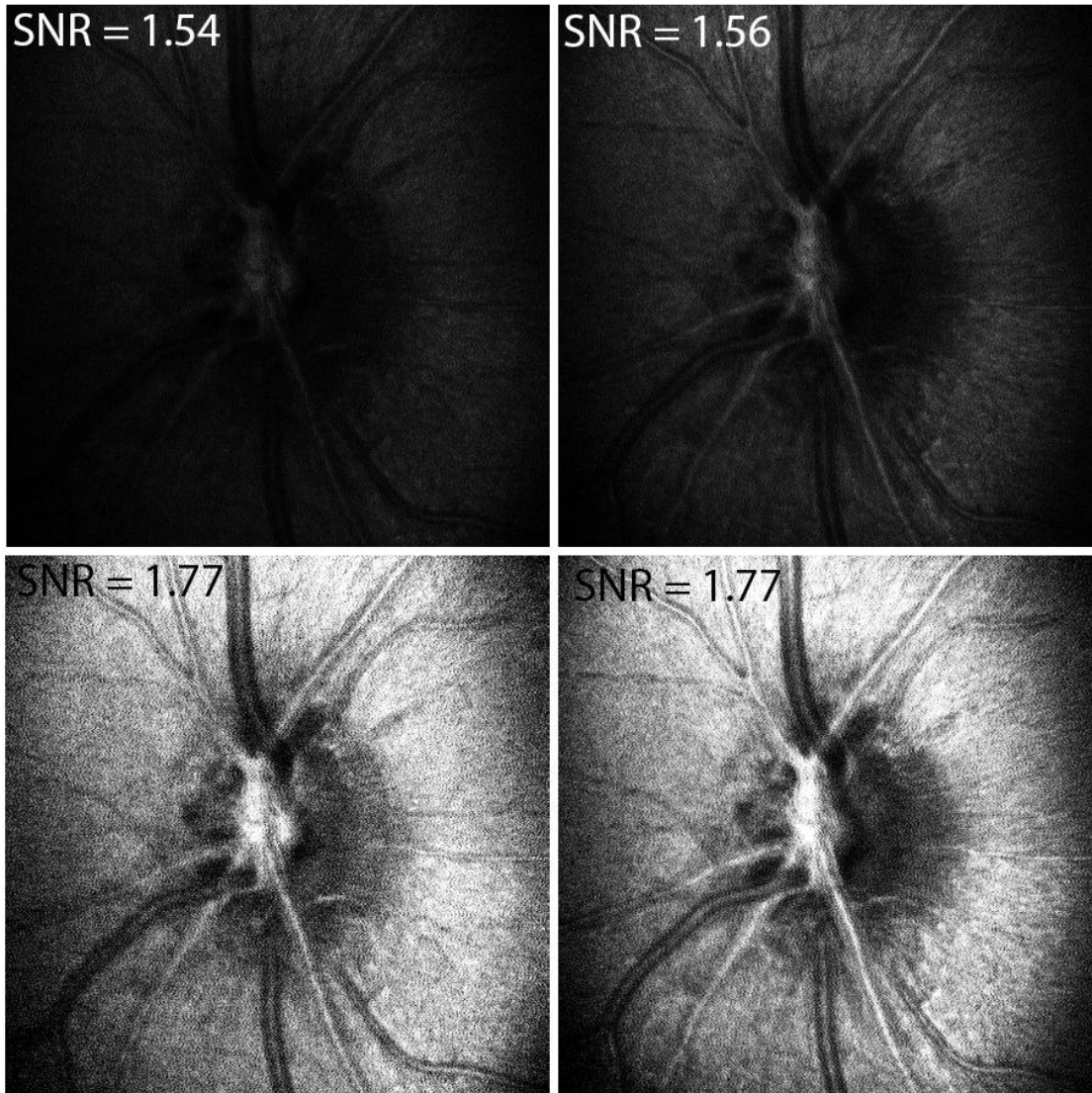


Figure 3.16: Original 100 μ pinhole image (top left), original 400 μ pinhole image (top right), histogram equalized 100 μ pinhole image (bottom left), and histogram equalized 400 μ pinhole image (bottom right).

This gives the edge detectors higher contrast edges to work with by increasing the SNR and increasing global brightness and contrast. However, even with a higher SNR value, the higher contrast edges come at the cost of higher contrast noise which can be picked up more easily by edge detection. Edge detector algorithms cannot tell the difference between an edge and the large pixel value difference between neighbouring pixels introduced by noise and will treat noise as edges. This is detrimental to the registration process.

In testing, all histogram equalizations showed improved SNR results when the histogram equalization was followed by a low pass filter to smooth out the noise that had been enhanced by the process (figure 3.17).

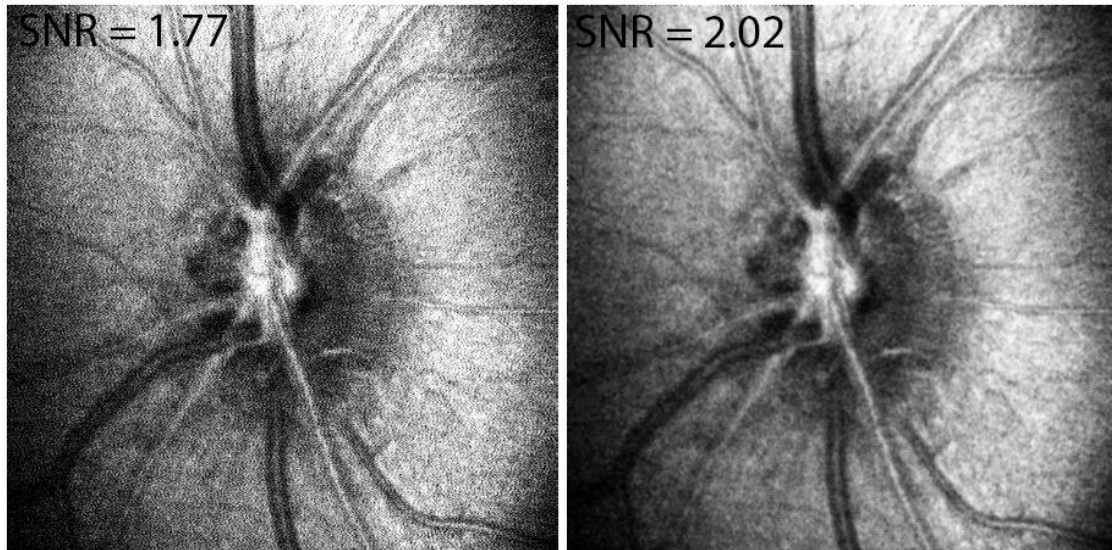


Figure 3.17: Histogram equalized image (left) and histogram equalized image followed by a low pass filter (right). Fine features appear smoother in the image after filtering.

Without the low pass filter, edge detection algorithms found the noise as edges and produced very poor results.

3.5.4 Influence of Controlled Variables on ONH Images

To ensure that the edge detection filter was versatile, many different typical images were chosen for registration. For the ONH, registration of images acquired using changes in the type of incident polarized light, pinhole changes, and depth changes were explored.

With a generator and analyzer in place in the CSLO, the influence of the polarization state on the intensity of the image is complex. It changes depending on the visible features, orientation of fiber layers and also from subject to subject. Since some areas of the nerve fiber layer are more sensitive to certain orientations of polarization state, the image brightness and contrast will vary slightly locally and globally (figure 3.18).

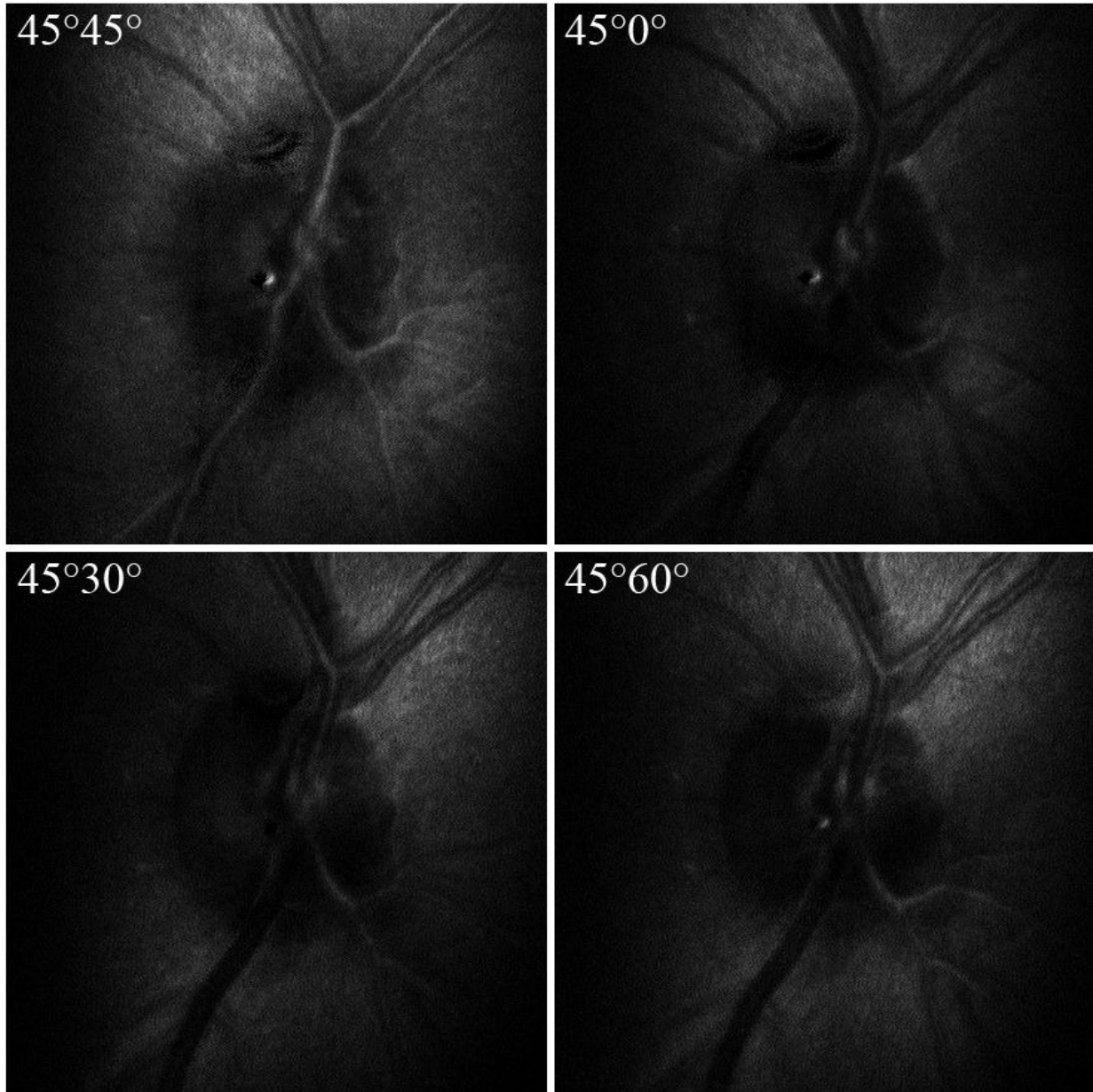


Figure 3.18: 4 images corresponding to the 4 settings on the polarization state analyzer.

With the analyzer removed and only a generator in place, the changes to brightness and contrast are more predictable (figure 3.19). While some local variation in the brightness can be seen, the observed changes between generator states are mostly seen as a global change in brightness and contrast.

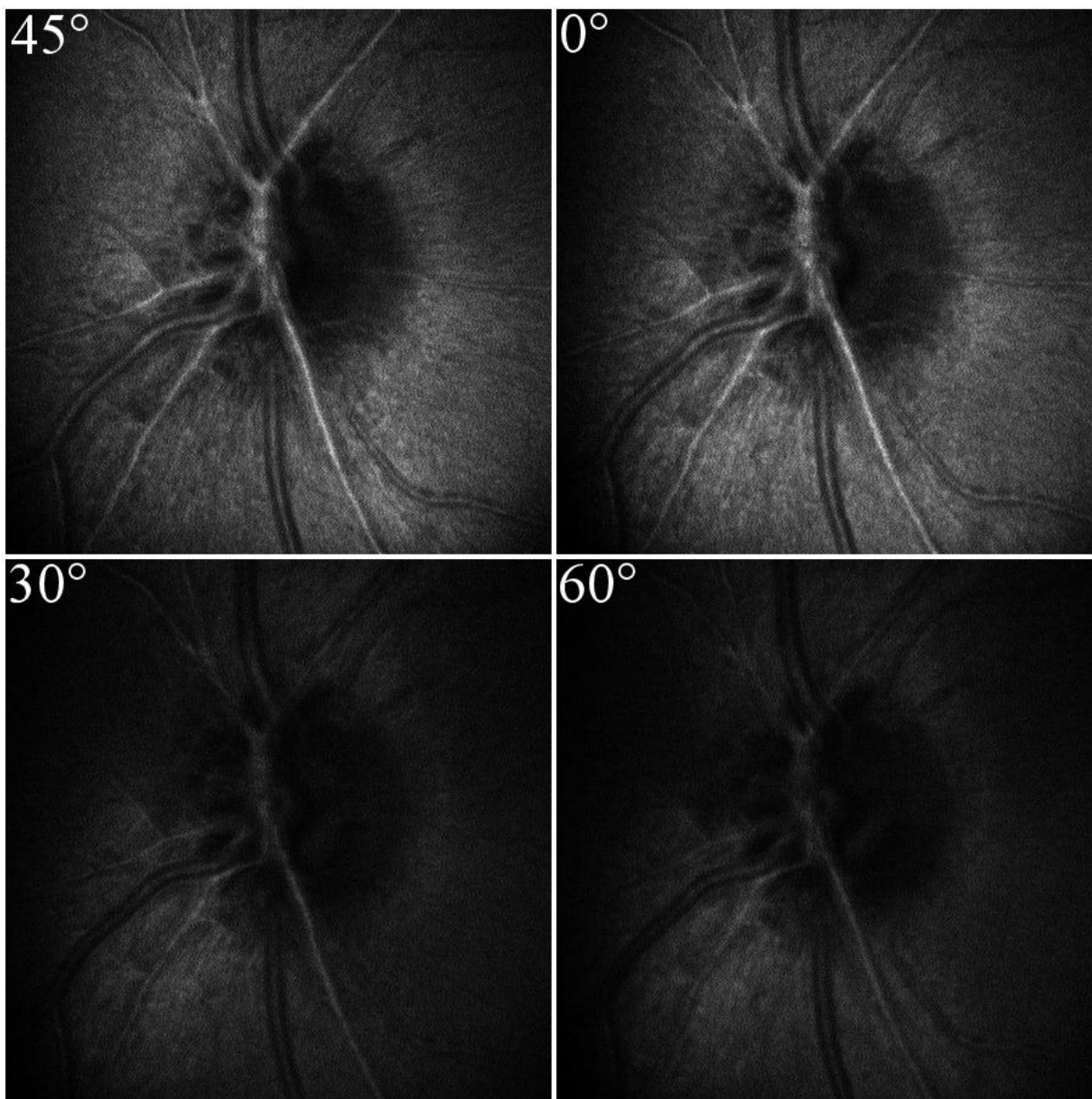


Figure 3.19: 4 images corresponding to the 4 settings on the polarization state generator with no analyzer.

Secondly, the lens, which controls the depth of measurement, changes the features distinguished in each image. While some images may show the surface of the nerve fiber layer and vessels, deeper optical slicing will image below the vessels into the nerve fiber layer and also into the ONH cup (figure 3.20). It should be noted that the images in figure 3.20 have been auto-contrasted to make feature difference more visible. Observe the differences in the two

images, in particular, how the vessels appear white when imaged on their surface, but when imaged by slicing through them, they appear black. Additionally, when imaging deeper, previously invisible blood vessels appear visible. Finally, the ONH is very dissimilar between images since the depth of focus of the left image is not great enough to pick up the deep features of the ONH cup, while the second image shows them more clearly.



Figure 3.20: Images of different depths of the same ONH taken with the CSLO.

Lastly, changing the pinhole size on the CSLO, directly before the detector, controls the amount of scattered light entering the detector and should affect the depth of focus of the image. This affects both the intensity of light globally across the entire image and the contrast and visibility of some of the features shown in each image. A large pinhole will yield a bright image but with a tradeoff, features will be less sharp since more scattered light will degrade contrast. Also light from out of focus planes will be picked up by the detector. That is, the optical slice is thicker. This also changes the features shown in each image because objects out of the plane of focus will still be picked up when the pinhole is larger.

It is interesting to note that reduced depth of focus between 100 and 400 micron pinholes seemed to disappear under histogram equalization as seen in figure 3.16. This occurs because histogram equalization redistributes pixel intensities, effectively spreading out and flattening the

images corresponding histogram, allowing for low contrast areas to appear with higher contrast. Since the apparent depth is due to variation between dark and bright areas, this can seem to vanish once histogram equalization is applied to an image.

3.5.5 Sobel Filter

Each edge detection filter reacted differently depending on the processing done previous to the application of the edge detection algorithm. On its own, the Sobel filter picked up the fine striations in the nerve fiber layer creating heavy noise in the final image. This created reduced clarity on the strong edges of the image, producing a poor registration success rate. The output of the Sobel filter versus no filter can be seen in figure 3.21.

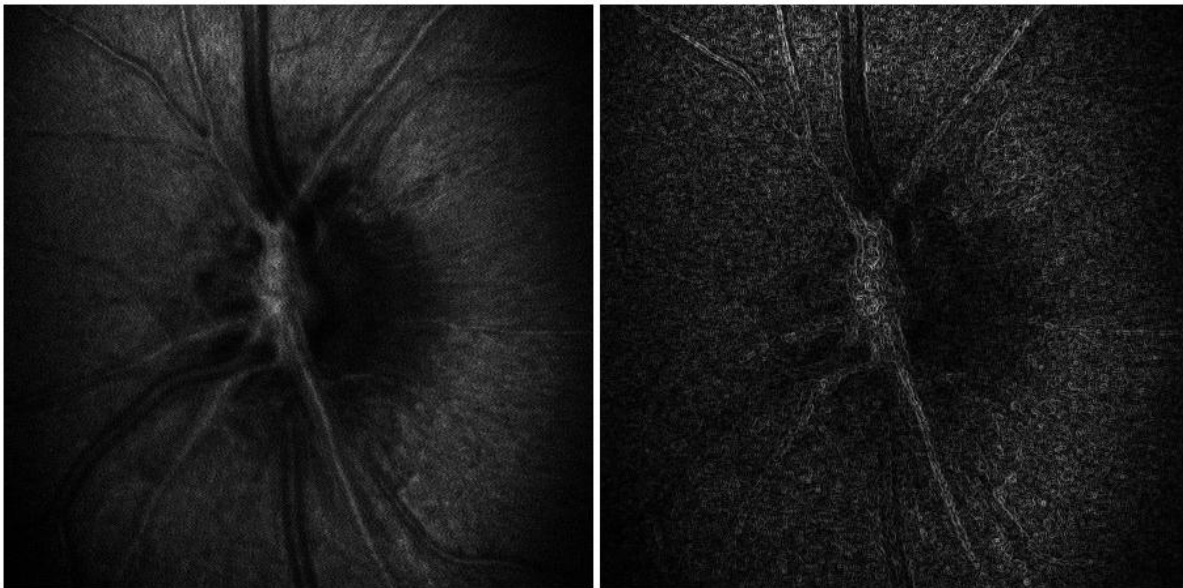


Figure 3.21: No filter image (left) and Sobel filter image (right).

The Sobel filter also worked poorly with any illumination variance correction. This is most likely because, while the correction did increase contrast around edges, it also greatly increased the strength of the noise within the image and small features that are undesirable for vessel edge detection such as the fine striations in the fiber layer. The combination of filters detected this increase in noise as small edges, resulting in extremely noisy images with low edge contrast (figure 3.22).



Figure 3.22: No filter image (left) and image resulting from an histogram equalization followed by a Sobel filter (right).

Since almost all of the strong edges are lost to noise after illumination variance correction, the low pass filter used to reduce noise after correction of illumination variation, leaves the Sobel filter little to work with, resulting in a low success rate for registration. Figure 3.23 shows the results of smoothing the histogram equalization with a low pass filter using a cut-off of 15 Hz and applying a Sobel filter.

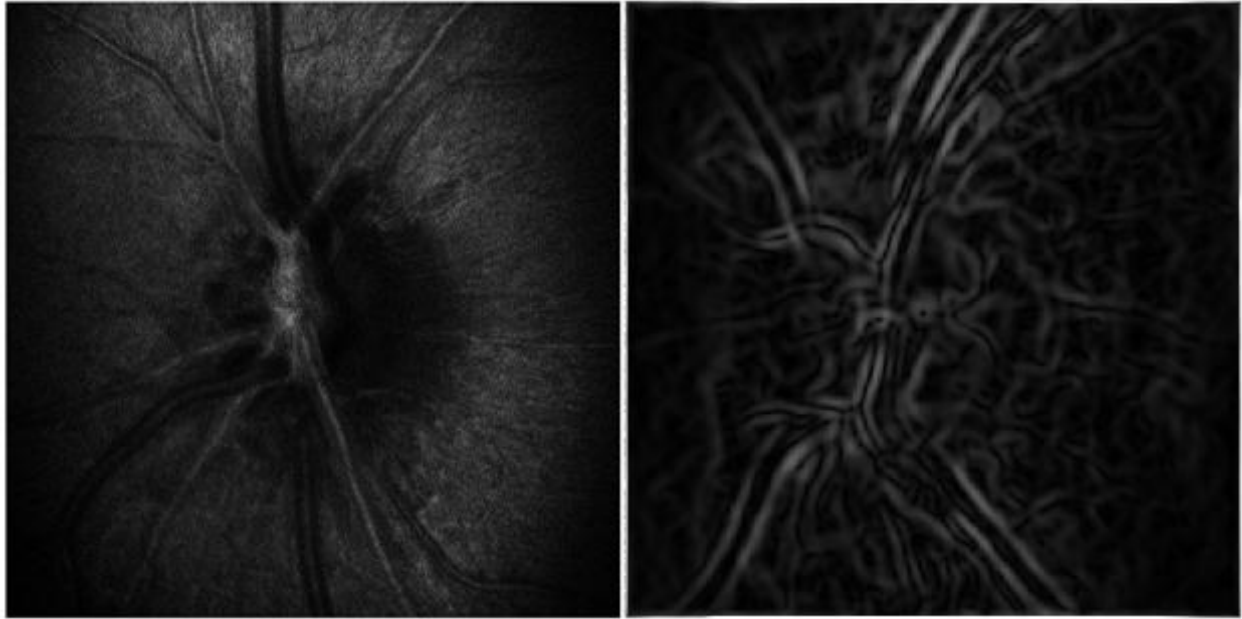


Figure 3.23: No filter image (left) and image resulting from an histogram equalization followed by a low pass filter followed by a Sobel filter (right).

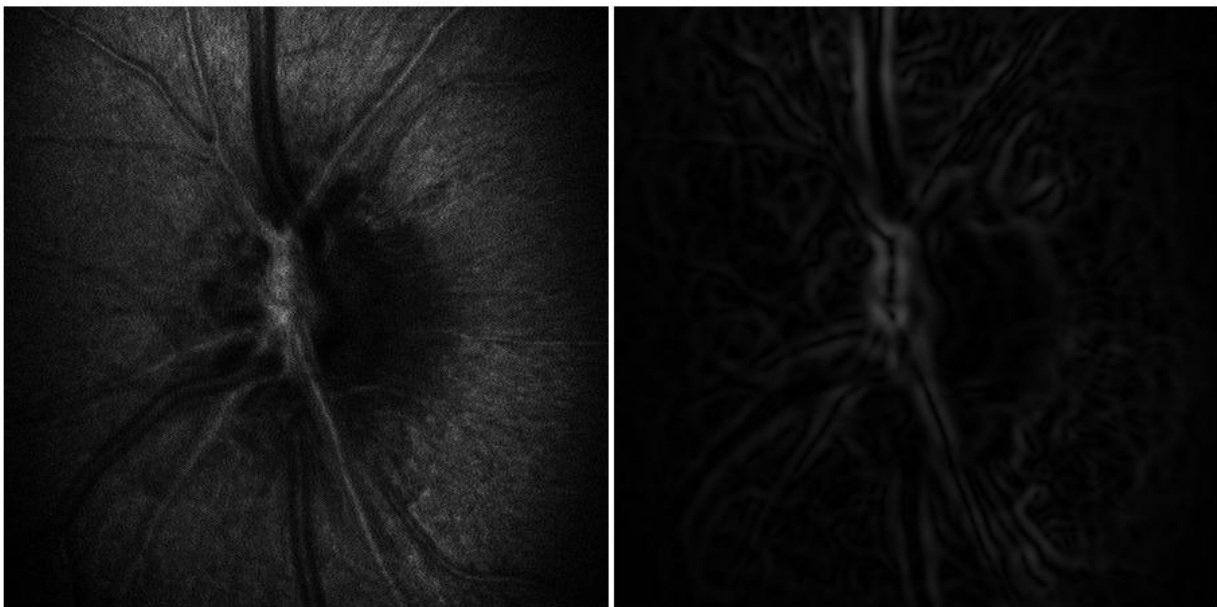


Figure 3.24: No filter image (left) and image with low pass filter followed Sobel Filter (right) with no illumination correction.

Since correction of illumination variance created such an increase in the noise level, the best choice was to skip it and apply a low pass filter to the original image in an attempt to reduce the finer features of the retina. This left mainly the strong edges of the blood vessels for the Sobel filter to enhance (figure 3.24).

3.5.6 High Pass Filter

The high pass filter reacted similarly to the Sobel filter when applied to an illumination variance correction, undesirably enhancing the noise and striations in the image (figure 3.25). While the vessels themselves did show up fairly well, the overall quality was hampered by the noisy nerve fiber layer.

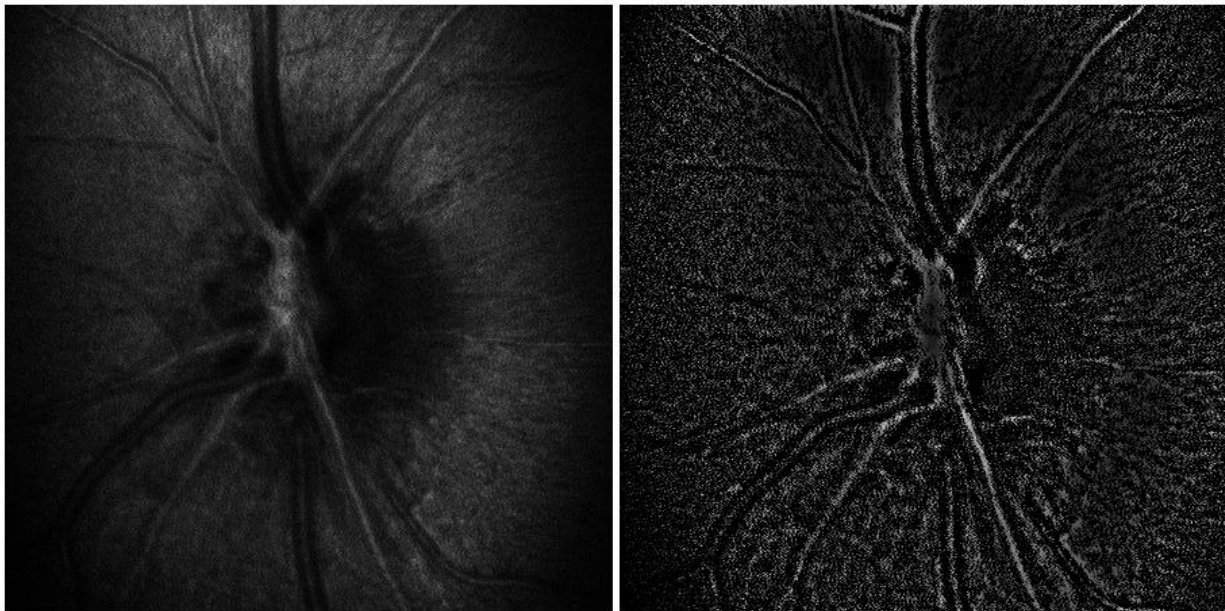


Figure 3.25: No filter image (left) and the image resulting from an illumination variance correction followed by a high pass filter (right).

Using a low pass filter followed by a high pass filter didn't produce good results because some of the vessel information was lost in the process (figure 3.26).

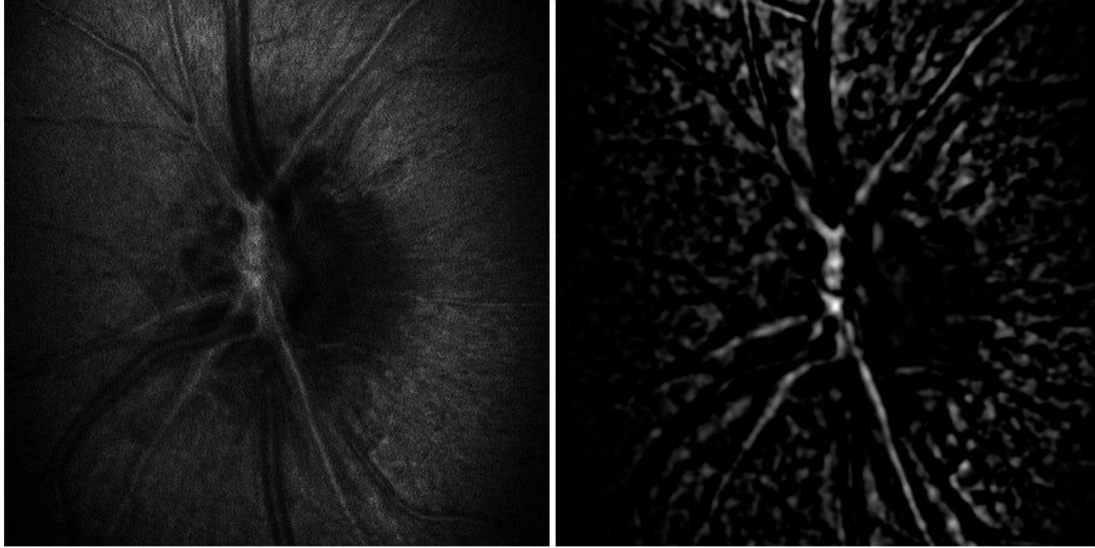


Figure 3.26: No filter image (left) and the image resulting from a low pass filter followed by a high pass filter (right).

The poor results from a low pass filter followed by a high pass filter (figure 3.26) possibly occurred because the strength of the vessel edge is not consistent due to depth changes of the vessel, varying background brightness of the retina and ONH cup, and the detection of the fine striations making up the RNFL.

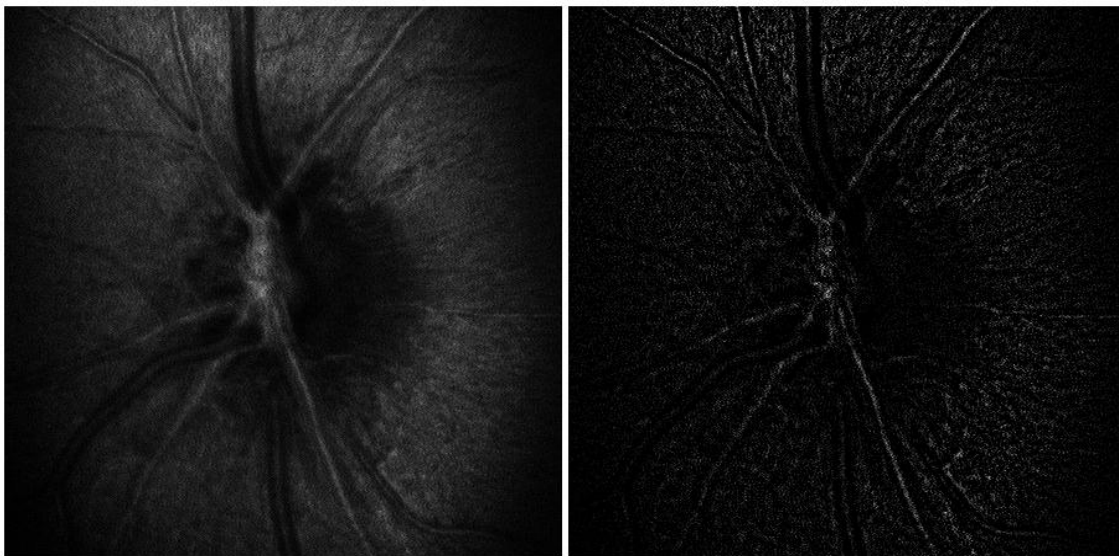


Figure 3.27: No filter image (left) and high pass filter image (right).

A simple high pass filter (figure 3.27) worked best to improve image registration because it reduced the signal of the fine striations in the RNFL while leaving the blood vessels themselves intact.

3.5.7 Canny Filter

When the Canny edge detection algorithm was applied to images by itself, the algorithm picked up noise and nerve fiber striations as edges (figure 3.28). This created many edges that change slightly with the noise, making registration unreliable.

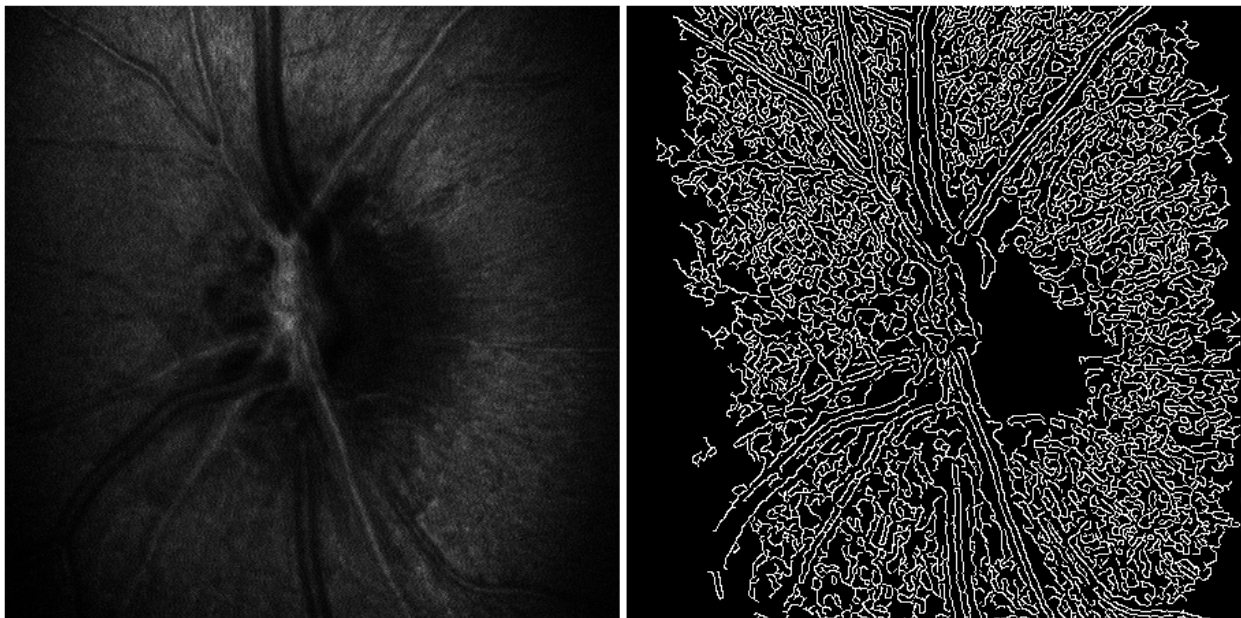


Figure 3.28: No filter image (left) and image with Canny filter (right).

The application of a low pass filter prior to the Canny filter greatly reduced the edges detected in the RNFL while maintaining the structure of the vessels which are the most important feature for registration (figure 3.29).

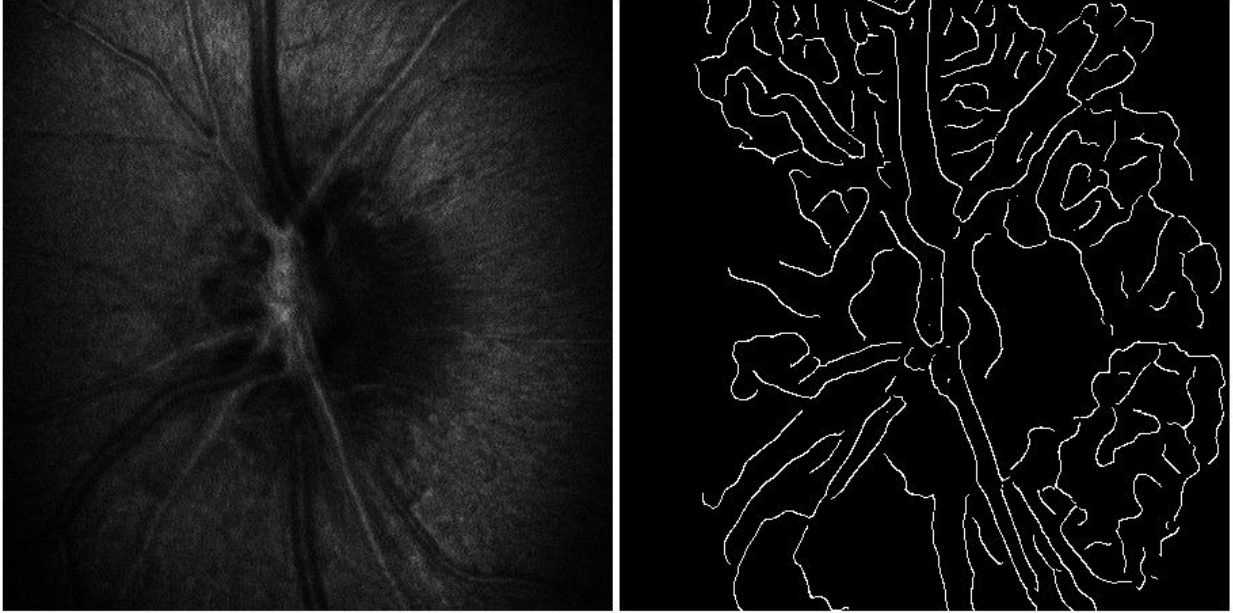


Figure 3.29: No filter image (left) and image resulting from a low pass filter followed by a Canny filter (right).

This can be taken further by first applying an histogram equalization to the image (figure 3.30).

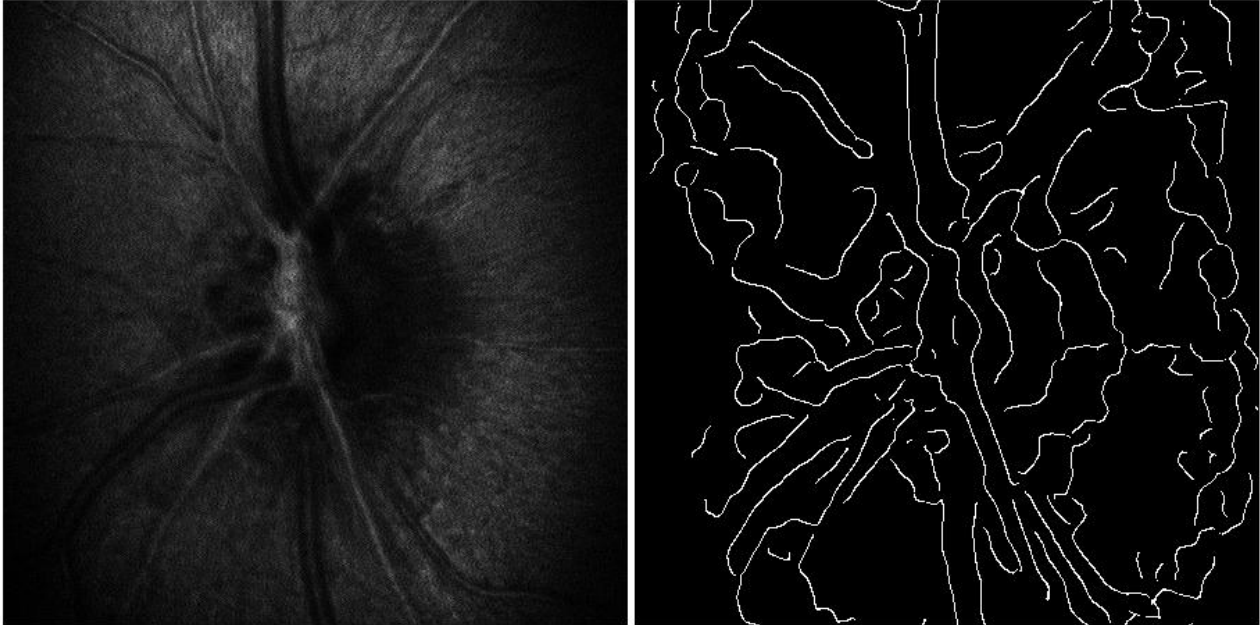


Figure 3.30: No filter image (left) and image resulting from histogram equalization followed by a low pass filter and then followed by a Canny filter (right).

While histogram equalization increased noise contrast substantially for the Sobel and high pass filter edge detection algorithms, the Canny filter (following a low pass filter) was not affected in the same way due to its binary nature. It also maintained vital information regarding the edge of the blood vessels. The application of the histogram equalization revealed information that was too dark to be picked up with just a low pass filter followed by Canny edge detector alone. Information close to the edges of the images is particularly important when aligning the orientation of the image since with rotation, pixels around the edges will move further than pixels near the centre. For the Canny filter, at least 3 of the 5 judgment points were always aligned.

3.5.8 Registration Results for ONH Images as a Function of Depth

Recall that for registration to be successful, each of the 5 points in figure 3.9 must align in a given image. From the first set of images, attempts were made to register 84 ONH images across 9 different participants. With no filter in place, 70.7% of the images were registered successfully.

The best result with a Sobel filter was comprised of a low pass filter with a cut off of 20 Hz to smooth out the noise and nerve fiber layer, leaving only the vessels for detection, followed by the Sobel filter. This yielded 89.3% of images registered. The results of the best Sobel filter can be seen in figure 3.31.

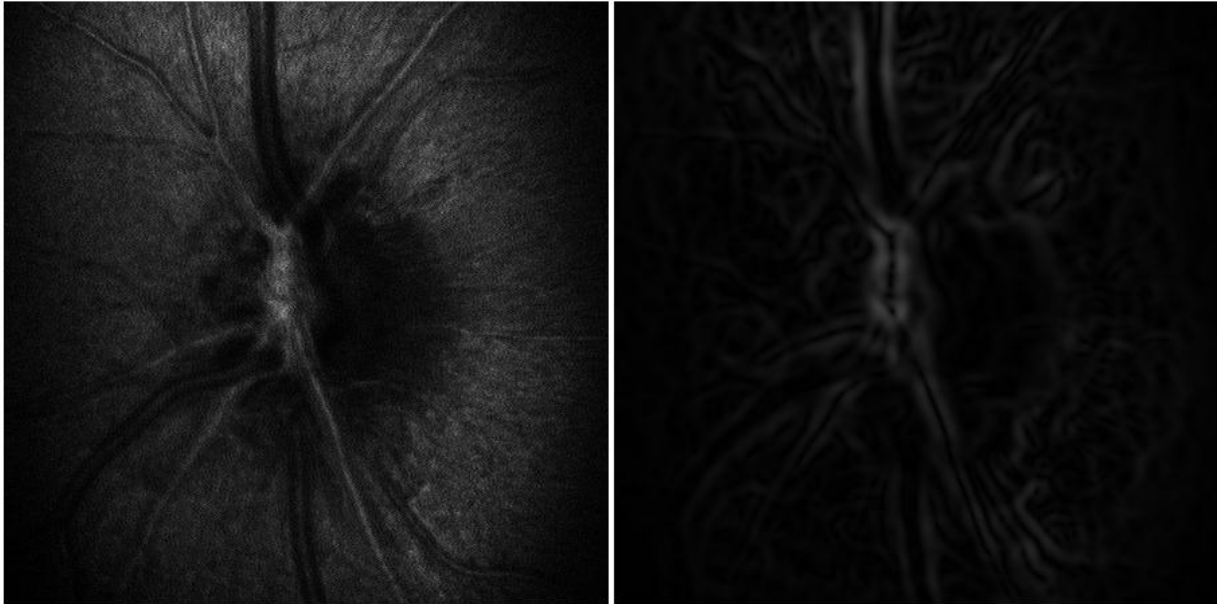


Figure 3.31: Image without filtering (left) and image resulting from a low pass filter followed by a Sobel filter (right).

The best high pass filter was simply a high pass filter with a cut off of 20 Hz giving very good results with 93.3% of images being successfully aligned. The high pass filter image is shown in figure 3.32.

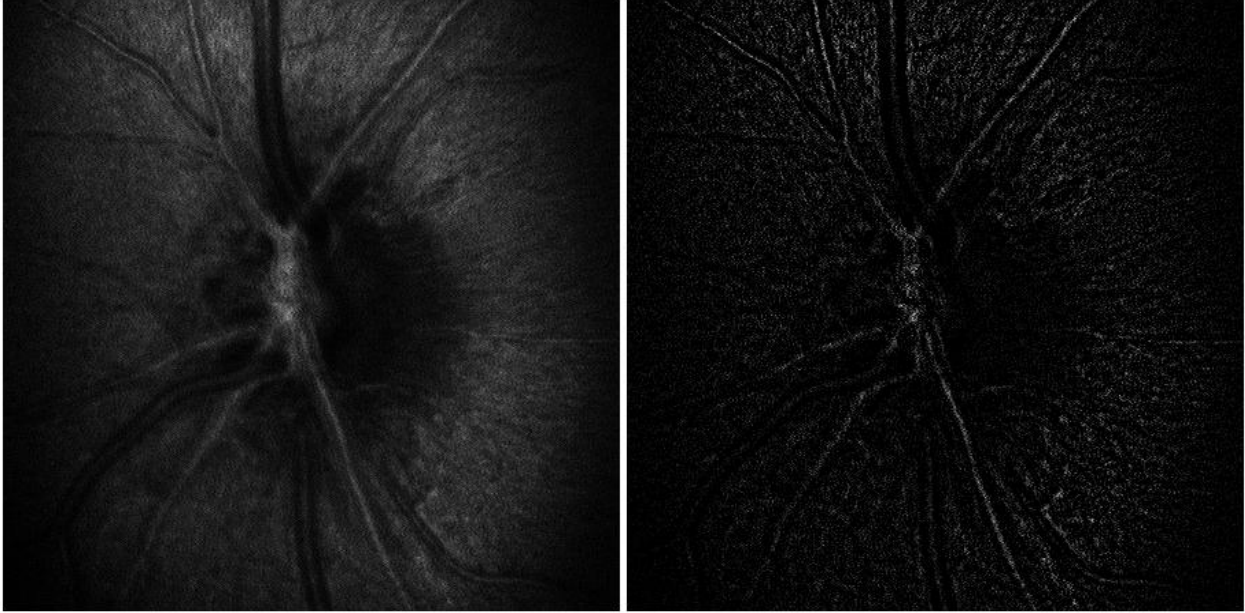


Figure 3.32: Image without filtering (left) and high pass filter image (right).

The best Canny filter produced the highest success rate of all the filters with 94.7% of images being successfully registered (figure 3.33). It was comprised of an histogram equalization, then a low pass filter with a cut off of 15 Hz, followed by a Canny filter.

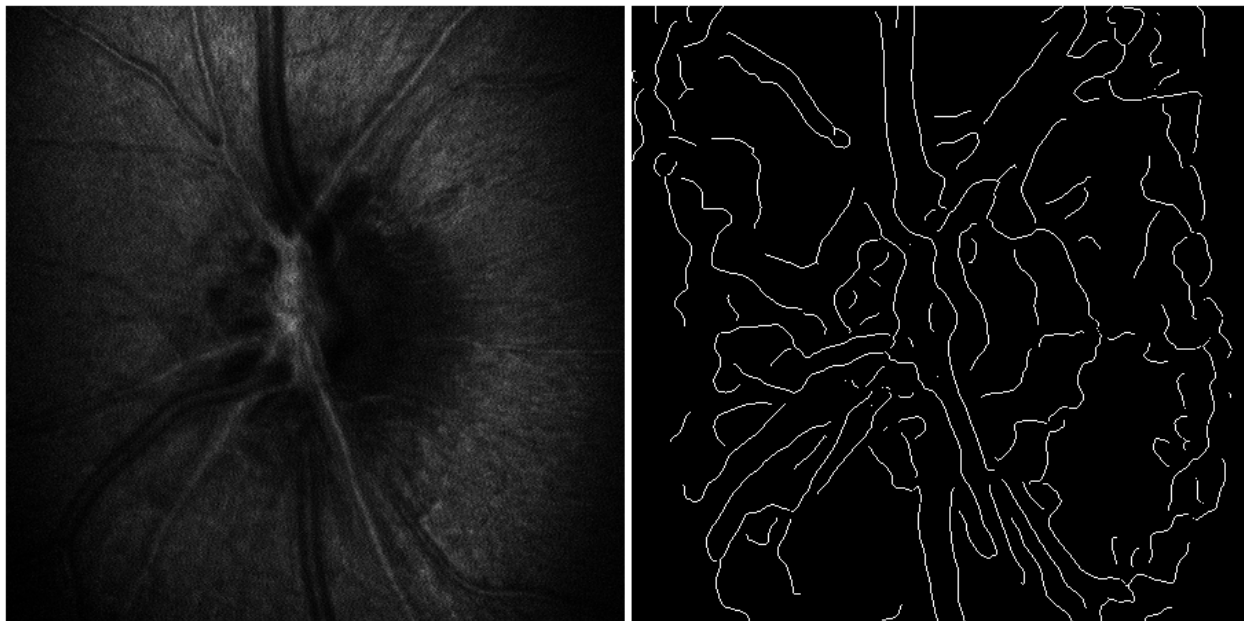


Figure 3.33: Image without filtering (left) and image resulting from an histogram equalization followed by a low pass filter followed by a Canny filter (right).

3.5.9 Registration Results for Fovea Images

Attempts to register 15 CSLO images of the fovea were made. With no filter in place, 20.0% of the images were registered successfully. The best high pass, Sobel, and Canny filters all produced outstanding and identical results, registering 93.3% of images. The filters and the original image with no filter can be seen in figure 3.34.

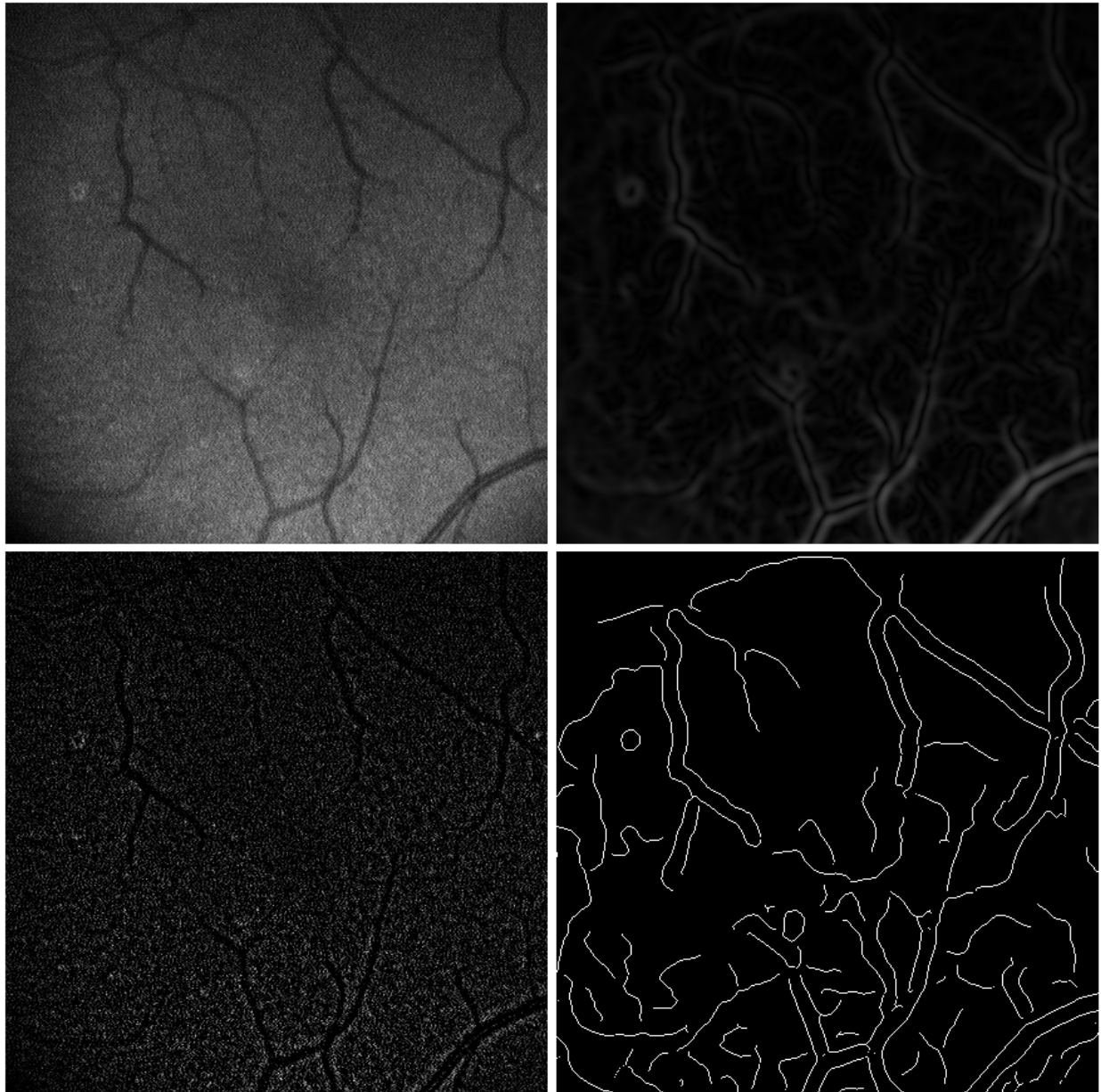


Figure 3.34: Image without filtering (top left), the same image with best Sobel filter (top right), with best high pass filter (bottom left), and with best Canny filter (bottom right).

3.5.10 Registration Results for Variable Analyzer ONH Images

From the ONH images taken at different depths and polarizer settings, across 11 participants, 132 registration attempts of images were made. With no filtering performed, 81.8% of the images were registered. The best Canny filter increased registration success to 91.7% of images.

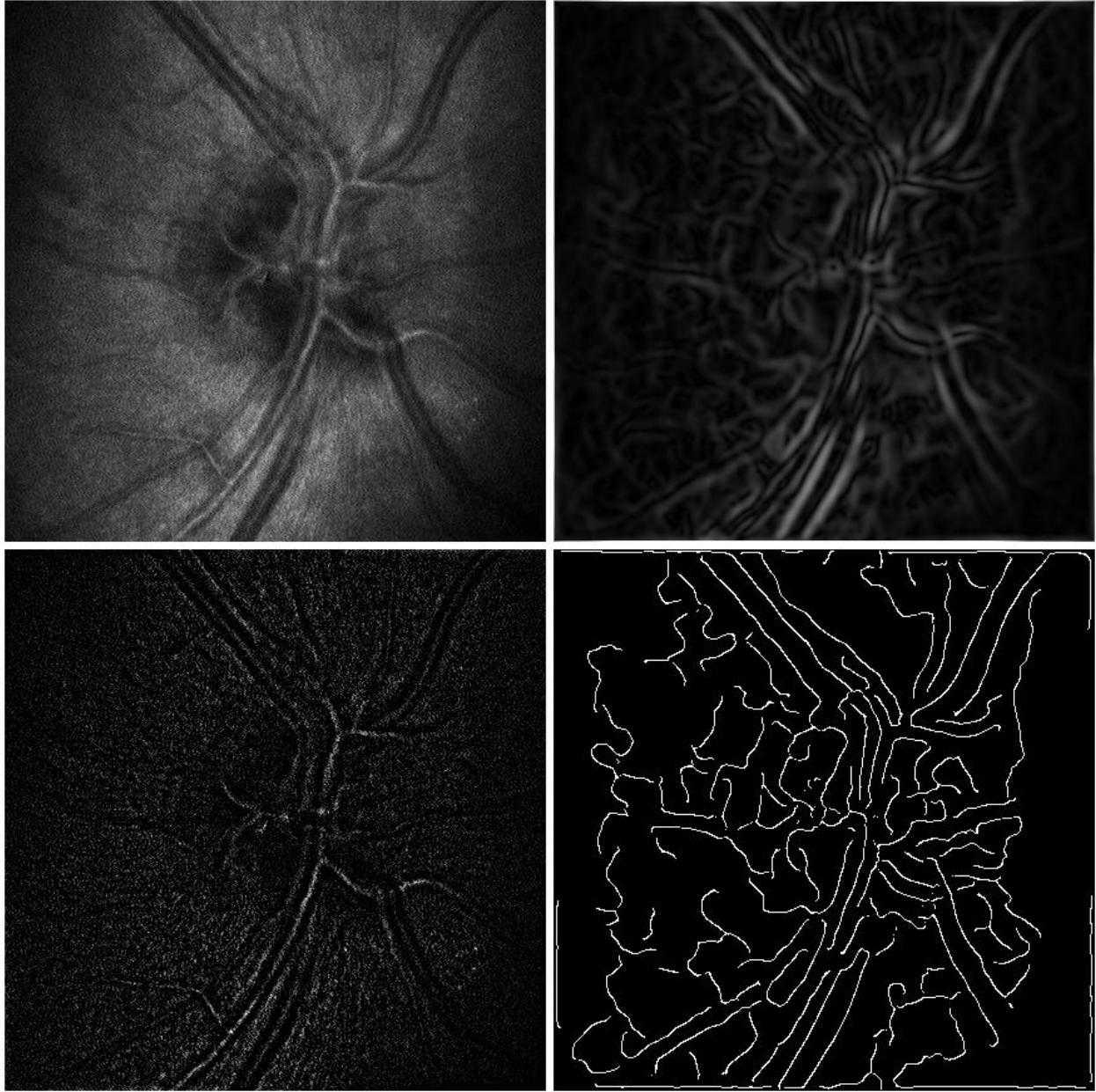


Figure 3.35: Image without filtering (top left), the same image filtered with best Sobel filter (top right), with best high pass filter (bottom left), and with best Canny filter (bottom right).

The second best results were from the high pass filter which achieved a success rate of 90.2%. Again, the worst of the three filters was the best Sobel filter, which had a success rate of 86.4%. The filtered images and the original image with no filter can be seen in figure 3.35.

3.6 Conclusions

As expected, automation of the rotation of quarter wave-plates within the generator and analyzer unit decreased acquisition time substantially, with a significant average time reduction of 414 s ($p = 0.0008$). Also since the participant no longer came in and out of the system, participant comfort increased.

The automation reduced the time needed to register the images during image processing for all 3 participants, but the results were not significant. The amount of time needed for translational and rotational correction also reduced non-significantly across participants. The time for registration was more sensitive to rotational changes than translational changes. An increased number of subjects would improve the power of the t-test.

Registration of CSLO images, using combinations of known edge detection filters increased the success rate of retinal image registration for a variety of optical and polarimetric configurations at two positions imaged with the CSLO. All three filters (high pass, Sobel and Canny) produced excellent results for foveal images, with registration success rates increased from 20% to 93.3%. For the ONH images in set 1, results were more dependent on the filter used. The best filter was an histogram equalization, followed by a low pass filter with a cut off of 15 Hz, followed by a Canny edge detection filter. Registration success rates went from 70.7% to 93.3%. For set 2 (consisting exclusively of polarization ONH images) the same best Canny algorithm achieved highest success rate increasing successful registrations from 81.8% to 91.7%. Over all images to be registered (set 1 and set 2), the best Canny algorithm gave best results improving success rate from 73.9% to 92.3%. The increased success rate will greatly reduce the overall processing time of acquired data. It also may allow for registration of samples that could not be registered without edge detection filters. This could allow for the calculation of polarization properties for samples that could previously not be assessed with polarimetry.

Chapter 4 - Reassessment of Mueller-matrix Image Quality Enhancement Methods

4.1 Overview

Mueller matrix polarimetry was used together with a CSLO imaging system to reassess 2 image quality enhancement techniques, Mueller matrix reconstruction (MMR) and Stokes vector reconstruction (SVR), using two image quality metrics, entropy and signal-to-noise ratio (SNR). Images output by the enhancement techniques were auto-contrasted or normalized within the algorithm. The goal of the reassessment was to determine the degree to which auto-contrasting or normalization is responsible for image quality improvement of the MMR and SVR images. Improvement was shown to be partially due to auto-contrasting or normalizing for MMR in terms of entropy but not in terms of SNR. For DOP and SVR, auto-contrasting or normalizing was partially responsible for image quality improvement in terms of both SNR and Entropy.

All data described in this chapter were acquired for the purpose of this thesis. For this experiment designed by myself, Marsha Kisilak, and Dr. Melanie Campbell, I operated the recording computer and provided guidance for the positioning of imaging on the retina. I also operated the analyzer and generator units on the CSLO. I registered, processed, and analysed all data acquired from the system. MMR and SVR software used in this work was written by Dr. Juan Bueno.

4.2 Introduction

Polarimetry has been reported to enhance image quality of imaging systems using several methods. Bueno and Campbell used Mueller matrix polarimetry to enhance retinal image quality in confocal microscopy by acquiring 16 different spatially resolved polarized images by incorporating a generator and analyzer unit in a confocal scanning laser ophthalmoscope (CSLO) [Bueno, 2007]. The techniques in their work were then simplified to require only 4 spatially resolved polarized images, greatly reducing acquisition and processing time while still showing image quality improvements (percent increases as high as 80% for entropy) for fundus images [Bueno, 2009b]. Bueno and Campbell also developed a second spatially resolved, 4 image polarization enhancement technique that utilized a modified version of the degree of polarization (DOP) as well as the first element of the calculated Stokes vector to improve image quality. Using this method, Bueno reported percent improvements above 200% in terms of entropy and

25% in terms of SNR for biological targets [Bueno, 2008]. However, when comparing CSLO images to reconstructed images to attain percent improvement values, auto-contrasting or normalization was performed at the end of the algorithm. This means that percent improvements may not only be due to the polarization methods alone but from a combination of polarization image enhancement methods and auto-contrasting or normalization.

In this chapter, both of these image enhancement methods will be reassessed with a comparison of the original methods to the same methods using auto-contrasted CSLO images. When choosing the best auto-contrasted CSLO images, SNR and entropy is reassessed and a new best image is chosen that is not necessarily the same image as the best CSLO image. The first method calculates images using the top row of the Mueller matrix (MM) to perform Mueller matrix reconstruction (MMR) [Bueno, 2007]. This method essentially looks at all possible polarization states and finds the “best” image, that is, the image that returns the highest value of SNR or entropy. The second method reconstructs images using the output Stokes vectors (SV) performing Stokes vector reconstruction (SVR) [Bueno, 2009b]. This method produces DOP and S_0 images which can be assessed for image quality by applying the SNR and entropy metrics. It should be noted that the labels MMR and SVR were chosen by me as umbrella terms for the methods summarized in Bueno and coauthors (2007 and 2009b).

The goal of the reassessment of these techniques is to show how much of the image quality improvements was due to auto-contrasting or normalization and how much was due to the polarization methods themselves. MMR images will also be compared to the linearly polarized CSLO image from each set, both original and auto-contrasted. Since many polarization retinal imaging systems only use linearly polarized light for imaging and may be modified to employ these image quality enhancement techniques, their performance with respect to linearly polarized light is an important distinction. SVR does not use linearly polarized light so no comparison will be made in that respect. For SVR, the comparison made was only against the best CSLO image.

4.3 Methods

Eleven participants were imaged at 2 imaging depths. Participants were chosen from ages 19 to 68 to study if percent change in metric value changed as a function of age. A lens was used to focus on the RNFL and then a second lens was used to focus on the LC for each participant. The

power of lens used was dependent on the participant. Sixteen recordings were acquired for each participant producing 176 CSLO recordings in total of the optic nerve head (ONH). For each recording, 8 images were chosen with centered optic nerve head. These images were averaged together to produce a reduced noise image for each required polarization setting. Images were reconstructed using MMR and SVR with the exact methods of Bueno and Campbell outlined in their corresponding papers [Bueno, 2007] and [Bueno, 2009b], respectively. These methods were performed using the appropriate configurations of the analyzer and generator units incorporated into the Waterloo CSLO for polarimetry imaging.

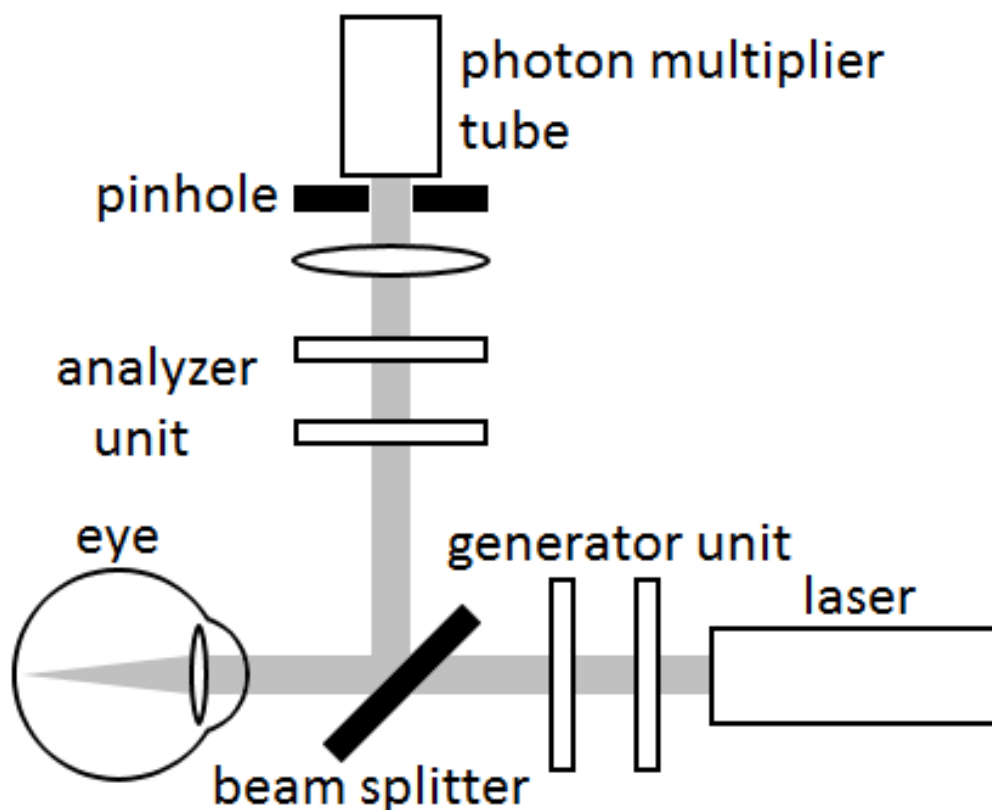


Figure 4.1: Waterloo CSLO schematic with removable generator and analyzer units in place.

Images were captured using a 400 μm confocal pinhole incorporated into the system as shown in figure 4.1 with a 15° field of view. Participants with normal ocular health and 6/6 corrected visual acuity were imaged at two depths, one at the depth of the lamina cribrosa and

the other at the depth of the retinal nerve fiber layer surrounding the ONH. Pupil dilation was induced for each participant using drops of 0.5% tropicamide before their imaging session. Every participant had their ocular health assessed by a licensed optometrist to ensure the safety of pupil dilation. All participants in need of refractive correction wore their spectacles or contact lenses during the imaging session. Eight frames were averaged for each CSLO image to reduce noise as described in section 3.5.2. This research received ethics clearance from the University of Waterloo Office of Research Ethics.

Over all for 11 participants at 2 imaging depths, both the Mueller matrix reconstructed images and Stokes vector reconstructed images combined with auto-contrasting were compared to the best original image (original image with highest value of SNR or entropy) and best auto-contrasted original image. The Mueller matrix reconstructed images were also compared to the original linearly polarized image (image acquired by the CSLO when the generator unit generates linearly polarized light) and best auto-contrasted linearly polarized image.

4.3.1 Auto-contrasting

When an image is auto-contrasted, its pixel values are linearly normalized to stretch across the entire greyscale of the image ranging from 0 to 255. The lowest pixel value of an image will be assigned a value of 0 (black) and the highest pixel value will assigned a value of 255 (white). For example, in the washed out image given below (left), the lowest pixel value is 55 and the highest pixel value is 187.

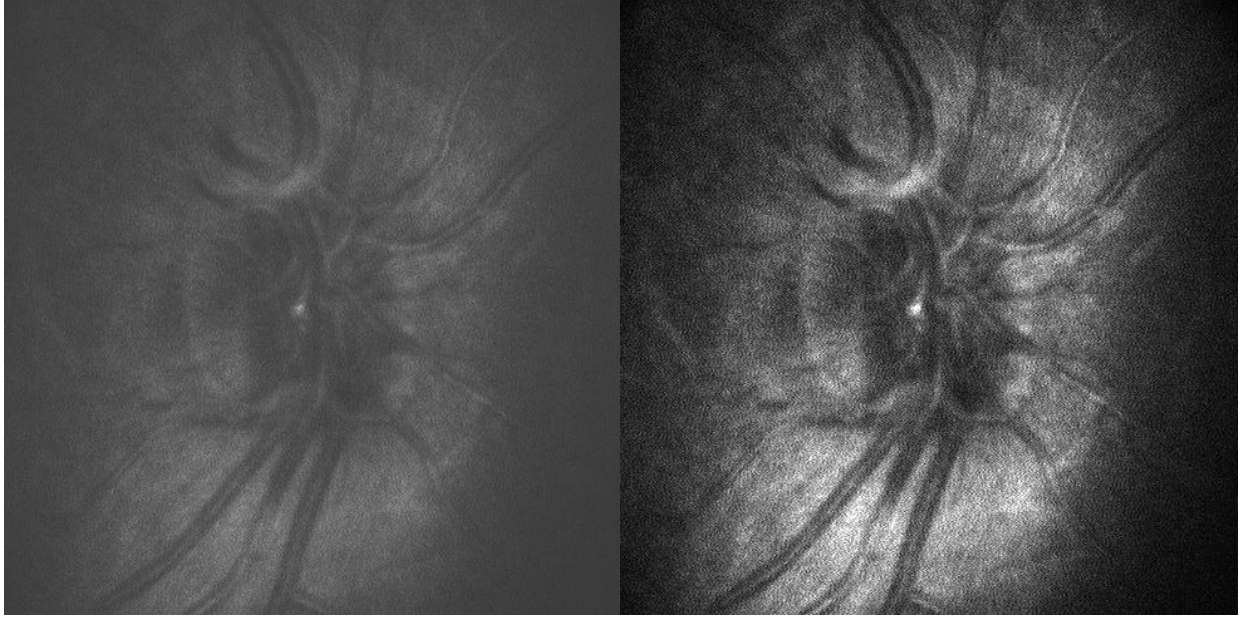


Figure 4.2: Original low contrast and dim image (left) and an image after auto-contrasting the original (right).

To auto-contrast the image, each pixel has the minimum pixel intensity subtracted from it, yielding values of 0 and 132 for the lowest and highest pixel intensity, respectively. Then, each pixel intensity value is divided by a 255/132 (dynamic range/highest pixel intensity) to normalize the values across the full dynamic range. As shown in figure 4.2, this can greatly improve the brightness and contrast of dark images but has less effect on already bright and/or high-contrast images. Note that an auto-contrast could make an image darker if it did not contain low valued pixels, but this never occurred for any images in this study.

4.3.2 Mueller Matrix Reconstruction

MMR requires the input of 4 spatially resolved CSLO images of differing polarization state. These states are determined by 4 different settings on a generator unit which is incorporated into the Waterloo CSLO as seen in figure 4.1. The analyzer is removed from the CSLO during imaging sessions for MMR.

As discussed in Chapter 1, every possible polarization state of light can be represented by its associated Stokes vector. The Stokes vector of the light measured at the photometer, $S_D^{(i)}$, is

related to the Mueller matrix of the combined system and Stokes vector of the light transmitted through the generator unit by:

$$S_D^{(i)} = M_C \cdot S_G^{(i)} \quad (4.1)$$

Where M is the Mueller matrix of the subject being imaged combined with the Mueller matrix of the scanning system where $M_C = M_{SCAN} M_{EYE} M_{DESCAN}$. $S_G^{(i)}$ is the predetermined Stokes vector produced by the generator unit for its 4 settings, $i = 1,2,3,4$. The first term of the Stokes vector, $S_{0D}^{(i)}$, represents the intensity values measured by the detector for the i^{th} setting of the generator unit. If we look at this relationship for a single generator setting, one can show that the intensity value S_{0D} is related to the top row of the Mueller matrix and the Stokes vector produced by the generator unit.

$$\begin{bmatrix} S_{0D} \\ S_{1D} \\ S_{2D} \\ S_{3D} \end{bmatrix} = \begin{bmatrix} m_{00C} & m_{01C} & m_{02C} & m_{03C} \\ m_{10C} & m_{11C} & m_{12C} & m_{13C} \\ m_{20C} & m_{21C} & m_{22C} & m_{23C} \\ m_{30C} & m_{31C} & m_{32C} & m_{33C} \end{bmatrix} \cdot \begin{bmatrix} S_{0G} \\ S_{1G} \\ S_{2G} \\ S_{3G} \end{bmatrix} \quad (4.2)$$

$$\therefore S_{0D} = [m_{00C} \quad m_{01C} \quad m_{02C} \quad m_{03C}] \cdot \begin{bmatrix} S_{0G} \\ S_{1G} \\ S_{2G} \\ S_{3G} \end{bmatrix} \quad (4.3)$$

This may be extended to the four polarization states created by the generator unit as they are related to the intensity values, $S_{0D}^{(i)}$, using exclusively the top row of the Mueller matrix. Let I_D represent the 4x1 matrix containing S_{0D} measured by the detector for each of the 4 configurations.

$$I_D = \begin{bmatrix} S_{0D}^{(1)} \\ S_{0D}^{(2)} \\ S_{0D}^{(3)} \\ S_{0D}^{(4)} \end{bmatrix} = [m_{00C} \quad m_{01C} \quad m_{02C} \quad m_{03C}] \begin{bmatrix} S_{0G}^{(1)} & S_{0G}^{(2)} & S_{0G}^{(3)} & S_{0G}^{(4)} \\ S_{1G}^{(1)} & S_{1G}^{(2)} & S_{1G}^{(3)} & S_{1G}^{(4)} \\ S_{2G}^{(1)} & S_{2G}^{(2)} & S_{2G}^{(3)} & S_{2G}^{(4)} \\ S_{3G}^{(1)} & S_{3G}^{(2)} & S_{3G}^{(3)} & S_{3G}^{(4)} \end{bmatrix} \quad (4.4)$$

$$I_D = M_{0C} \cdot M_G \quad (4.5)$$

$$M_{0C} = I_D \cdot (M_G)^{-1} \quad (4.6)$$

Using equation 4.6, the top row of the Mueller matrix may be calculated using only the intensity images recorded by the detector and the known Stokes vector S_0 components corresponding to the 4 polarization states produced by the generator unit.

Using the top row of the Mueller matrix, one may now calculate the resulting intensity level for *any* input polarization state. The resulting intensity image can be calculated for any input polarization state once the Mueller matrix has been calculated at each pixel. Recall that the first term of the Stokes vector represents the intensity value measured by the detector. Generally for any sample, this can be expressed as:

$$S_0^{OUT} = [m_{00C} \quad m_{01C} \quad m_{02C} \quad m_{03C}] \cdot \begin{bmatrix} S_0^{IN} \\ S_1^{IN} \\ S_2^{IN} \\ S_3^{IN} \end{bmatrix} \quad (4.7)$$

Also, remember that from section 1.4, it was shown that the elements of the Stokes vector may be written in terms of ellipticity and orientation of the polarization ellipse:

$$S_1 = S_0 \cos 2\chi \cos 2\psi \quad (4.8)$$

$$S_2 = S_0 \cos 2\chi \sin 2\psi \quad (4.9)$$

$$S_3 = S_0 \sin 2\chi \quad (4.10)$$

where χ and ψ are the ellipticity and orientation, respectively. If we sub equations 4.8 to 4.10 into 4.7, it can be seen that:

$$S_0^{OUT} = [m_{00} \quad m_{01} \quad m_{02} \quad m_{03}] \cdot \begin{bmatrix} S_0^{IN} \\ S_0^{IN} \cos 2\chi \cos 2\psi \\ S_0^{IN} \cos 2\chi \sin 2\psi \\ S_0^{IN} \sin 2\chi \end{bmatrix} \quad (4.11)$$

We can now calculate the output intensity image, S_0^{OUT} , for any input polarization state, defined by its position on the Poincare sphere. For any completely polarized input Stokes vector,

the value of S_0^{IN} will always be one [Collett, 1992]. This means we can set $S_0^{\text{IN}} = 1$, simplifying equation 4.11 into:

$$S_0^{\text{OUT}} = [m_{00} \quad m_{01} \quad m_{02} \quad m_{03}] \cdot \begin{bmatrix} 1 \\ S_0 \cos 2\chi \cos 2\psi \\ \cos 2\chi \sin 2\psi \\ \sin 2\chi \end{bmatrix} \quad (4.12)$$

Finally, by using equation 4.12, we can vary χ and ψ to calculate the output image for all possible input polarization states.

The variables χ and ψ are varied by 5° steps producing the output images resulting from the many input polarization states. This is equivalent to changing the Stokes vector of the input polarization so that it traces out the entire Poincaré sphere surface, approximately representing every possible input polarization state.

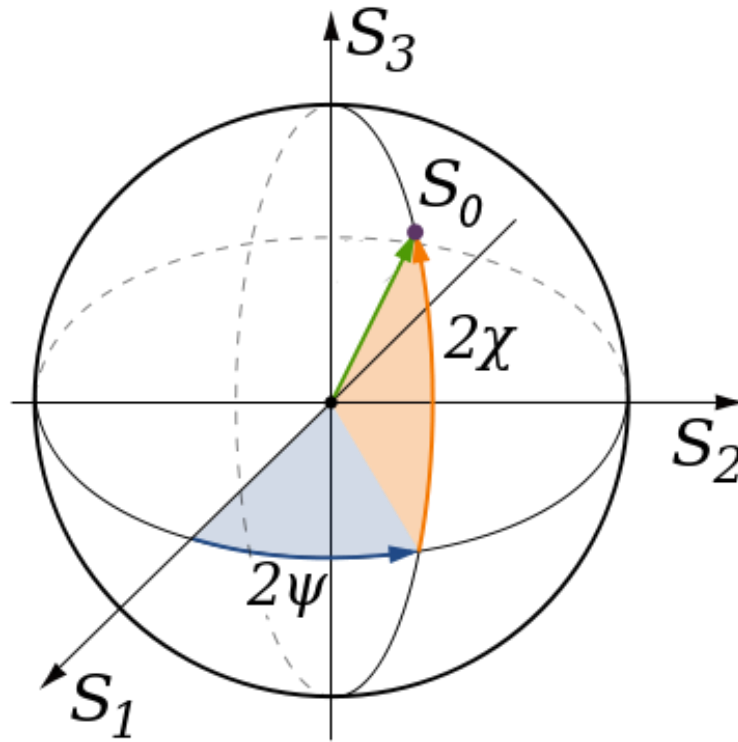


Figure 4.3: A convenient geometrical representation of all possible polarization states (Public domain wikipedia image - http://en.wikipedia.org/wiki/File:Poincaré_sphere.svg).

By outputting images for all polarization states (in the 5° increments around the sphere), we are able to find the polarization state that corresponds to the best value generated by image quality metrics when applied to each output image. In this case, image quality metrics signal-to-noise ratio (SNR) and entropy are applied to each image to quantify the image quality. From this, MMR will produce 2 reconstructed images, the image corresponding to the maximum SNR value and a second image corresponding to the maximum entropy value. For each participant, I produced the MMR max SNR and max entropy images by inputting original CSLO images which were then compared to the best original CSLO image (the CSLO image yielding the highest value of the corresponding metric). Then, a second set of MMR max SNR and max entropy images was reconstructed by inputting auto-contrasted CSLO images. Those were compared to the best auto-contrasted CSLO image. Once auto-contrasted images are input into the MMR algorithm, the top row of the Mueller matrix elements are no longer the true elements since auto-contrasting of CSLO images changes the relative values of the pixels between the 4 input images. The Mueller matrix elements and reconstructed images would lose any physical meaning with this change. However, it is still of interest to see if the reconstructed images have improved quality. The MMR reconstruction algorithm used is that of Bueno [Bueno, 2007] which auto-contrasts images at the end of the algorithm.

4.3.3 Stokes Vector Reconstruction

SVR also requires the input of 4 spatially resolved CSLO images of differing polarization state. These states are determined by a constant setting on the generator unit (which produces circularly polarized light) and 4 different settings of the analyzer unit. Both units are incorporated into the Waterloo CSLO as seen in figure 4.1.

By setting the generator unit to produce circularly polarized light and using four different polarization sampling positions of the analyzer unit, we can determine the Stokes vector of reflected light for the input polarized light. With both an analyzer and generator unit in place in the CSLO, the Stokes vector of the light measured at the photometer, I_D , is related to the four corresponding intensity images by:

$$\begin{bmatrix} I_1 \\ I_2 \\ I_3 \\ I_4 \end{bmatrix} = M_A \cdot I_D = M_A \cdot \begin{bmatrix} S_0 \\ S_1 \\ S_2 \\ S_3 \end{bmatrix} \quad (4.13)$$

$$I_D = \begin{bmatrix} S_0 \\ S_1 \\ S_2 \\ S_3 \end{bmatrix} = (M_A)^{-1} \cdot \begin{bmatrix} I_1 \\ I_2 \\ I_3 \\ I_4 \end{bmatrix} \quad (4.14)$$

Where M_A is the known 4x4 matrix for the CSLO's analyzer unit comprised of the four Stokes vectors representing the different polarization states produced by the four settings of the analyzer unit. Each Stokes vector component is a function of pixel position which can be mapped as an image.

Once the Stokes vector at the detector for each pixel is known, we can calculate the modified degree of polarization (DOP_M) at each pixel position, giving the modified DOP image. The value S_0^{Max} is a constant value and is equal to the maximum pixel value found over the entire S_0 image.

$$DOP_M = \frac{\sqrt{(S_1^2 + S_2^2 + S_3^2)}}{S_0^{Max}} \quad (4.15)$$

Within the DOP_M calculation, once the Stokes parameters are determined they are stretched by dividing each of the 4 parameters by S_0^{Max} as can be seen in equation 4.15. This in effect normalizes S_0 (which is not used in the calculation of DOP_M) while stretching S_1 , S_2 , and S_3 but not completely normalizing them from 0 to 1 (black to white). This means that the S_0 that is compared to the initial images is normalized, while the initial images are not.

Once the stretched Stokes parameters are used to calculate DOP_M in the algorithm, DOP_M is auto-contrasted before it is output.

Recall that the amount of DOP is calculated by:

$$DOP = \frac{\sqrt{(S_1^2 + S_2^2 + S_3^2)}}{S_0} \quad (4.16)$$

The DOP_M can be found in terms of DOP by multiplying both sides of the DOP equation by S_0 and dividing both sides of the equation by S_0^{Max} .

$$DOP * S_0 = \sqrt{(S_1^2 + S_2^2 + S_3^2)} \quad (4.17)$$

$$\frac{DOP * S_0}{S_0^{Max}} = \frac{\sqrt{(S_1^2 + S_2^2 + S_3^2)}}{S_0^{Max}} = DOP_M \quad (4.18)$$

This means that the DOP_M is $DOP * S_0$ divided by S_0^{Max} (the constant maximum pixel value across the entire S_0 image). Again the output image has been normalized while the input images to which it is compared have not.

In the MMR calculation, the final output image is normalized to have a maximum value of 1, indicating that it corresponds to a polarized light image. This image is then compared to an initial input image which has not been normalized.

In order to see the effect of the stretching of the images in comparison to the differences in polarization, I compared the final images to the initial images, after the initial images are auto-contrasted. Since there are normally black pixels in the images, this is equivalent to the stretching that is performed on the output images.

Work by Song et al. calculated the all polarized light image using by simply multiplying $DOP * S_0$. This was found to improve image quality [Song, 2008]. This was compared to DOP_M to assess image quality differences with SNR and entropy.

DOP_M and S_0 images produced by SVR are auto-contrasted within the algorithm. From this, SVR will produce 2 reconstructed images, the calculated S_0 image and the DOP_M image. Both the DOP_M image and S_0 image have their image quality quantified by image quality metrics SNR and entropy. Unlike MMR, auto-contrasted images cannot be input into the SVR algorithm because they would change the value of the Stokes parameters. The S_0 and DOP_M images produced by SVR were compared to both the best original CSLO image input into the SVR algorithm and the best image after the same images have been auto-contrasted.

4.3.4 Image Quality Metrics

Signal-to-noise ratio is a good measure of image quality because it measures the strength of the signal relative to the background noise level. This noise can result from laser speckle and noise within the imaging system, among other sources. SNR is defined as the ratio of the mean

intensity of the pixels (the pixel value) to the standard deviation of the pixel intensities [Blanchet, 2006].

$$\text{SNR} = \frac{\overline{I(x,y)}}{\sqrt{\left(\frac{1}{(i-1)(j-1)}\right) \sum_{x=1}^i \sum_{y=1}^j (I(x,y) - \overline{I(x,y)})^2}} \quad (4.19)$$

The pixel intensity as a function of spatial location on the image is represented by $I(x, y)$ and i and j are the number of horizontal and vertical pixels in the image, respectively.

Also used to measure image quality is the metric Shannon entropy. In this work, a predefined calculation for entropy was used from the Matlab library defined as:

$$\text{Entropy} = - \sum_x \sum_y I(x, y)^2 \ln (I(x, y)^2) \quad (4.20)$$

Shannon entropy is dependent on the absolute values of pixel intensities within a given two-dimensional image. Although the relationship is complex, generally, as pixel intensity increases, entropy increases. This is demonstrated in section 4.4.7. Hunter et al found entropy to be a superior image quality metric for fundus image quality when compared to SNR [Hunter, 2006]. For both image quality improvement techniques, following Bueno's method, the output images were compared to both the best original images acquired from our Waterloo CSLO. We have added a comparison to the best original images after auto-contrasting. The best original images are chosen as the image yielding the highest SNR or entropy values of the 4 output polarization images from the CSLO for Mueller matrix top row measurement or Stokes vector measurement.

Metric improvement was calculated using a standard percent change calculation:

$$\% \text{ improvement} = \frac{A-B}{B} \times 100 \quad (4.21)$$

where A is the image quality metric value of the given reconstruction method and B is the image quality metric of the original CSLO image.

4.4 Results

4.4.1 Mueller Matrix Reconstruction VS Best CSLO Image

As expected, Mueller matrix reconstruction showed significant improvement over the best CSLO image (no auto-contrasting) in terms of both SNR and entropy at both imaging depths. Since all percent increases of entropy or SNR are above zero, the mean values of entropy and SNR at both depths must always be significantly above zero.

Both MMR max entropy and max SNR images always showed positive improvement when compared to the best CSLO image (not auto-contrasted) as expected across all 11 participants at both the LC and RNFL depth. Images of the LC and RNFL yielded very similar results. Entropy showed large, significant (Fig. 4.4, 4.26) percent increases and a significant positive linear relationship with age at the LC depth ($p = 0.048$, $R^2 = 0.37$, using Sigmaplot's linear fitting) (figure 4.4). At the RNFL depth, the linear regression model was not significant ($p = 0.08$, $R^2 = 0.30$).

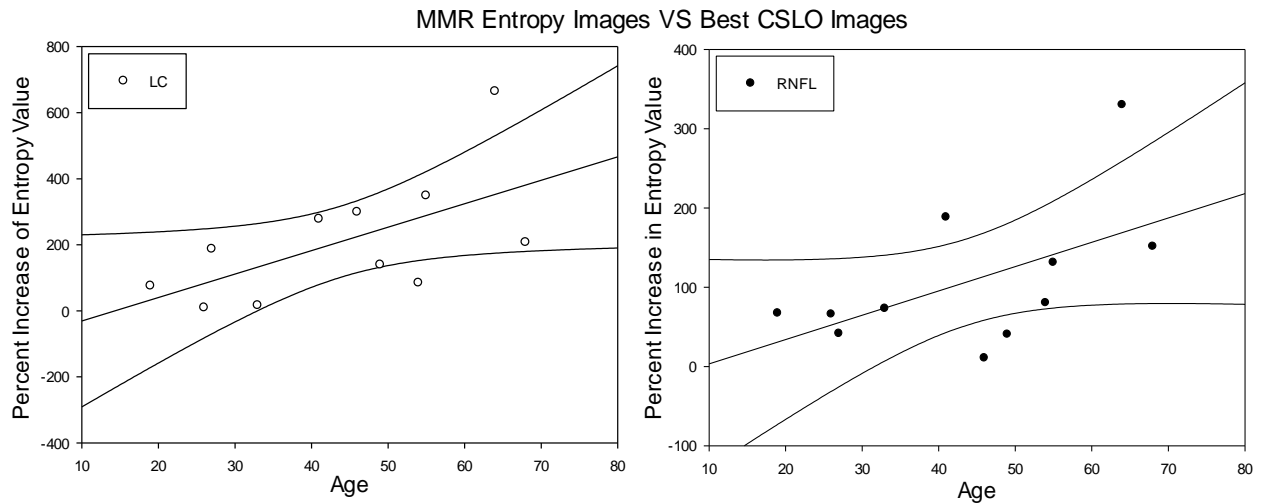


Figure 4.4: Percent improvement of MMR images over the best CSLO images as measured by entropy at the LC (left) and RNFL (right) depths. The fit on the left (LC) is significant while that on the right is not (RNFL).

When compared to original CSLO images, SNR improvement showed no significant relationship between percent increase in SNR value and age when fit with the linear regression model at the LC depth ($p = 0.26$, $R^2 = 0.14$) or the RNFL depth ($p = 0.26$, $R^2 = 0.14$) and yielded all positive percent increases considerably lower than entropy (figures 4.5, 4.28).

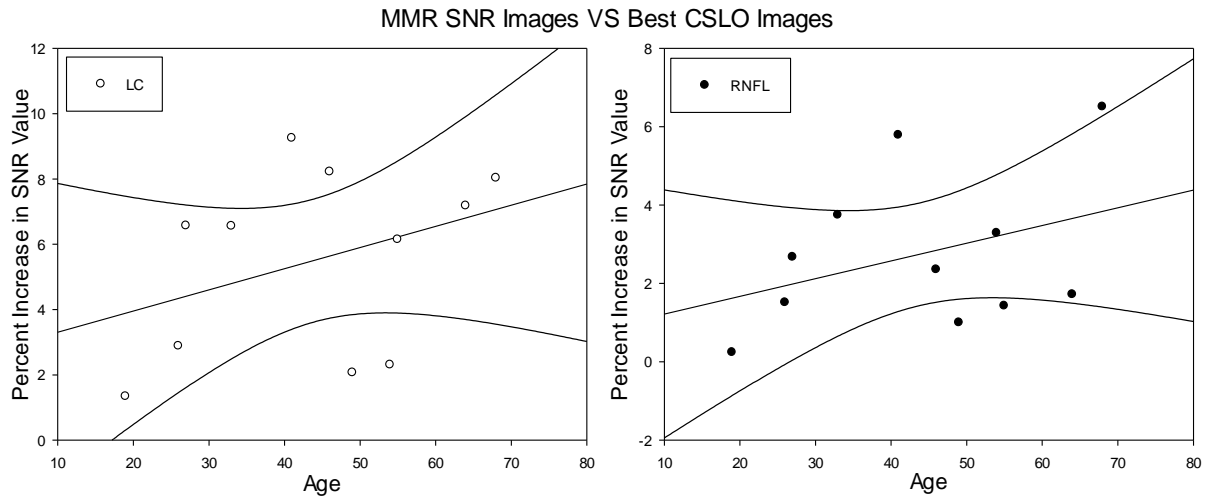


Figure 4.5: Percent improvement of MMR images over the best CSLO images as measured by SNR at the LC (left) and RNFL (right) depths. Fits shown are not significant.

The results when inputting auto-contrasted CSLO images into the MMR algorithm differ considerably. The percent change in entropy still showed all positive, significant results for all image sets, but percent increases were considerably lower (Fig 4.26) and now show no significant relationship between percent increase in entropy and age with the linear fit at the LC depth ($p = 0.60$, $R^2 = 0.03$) or the RNFL depth ($p = 0.80$, $R^2 = 0.007$) (figure 4.6).

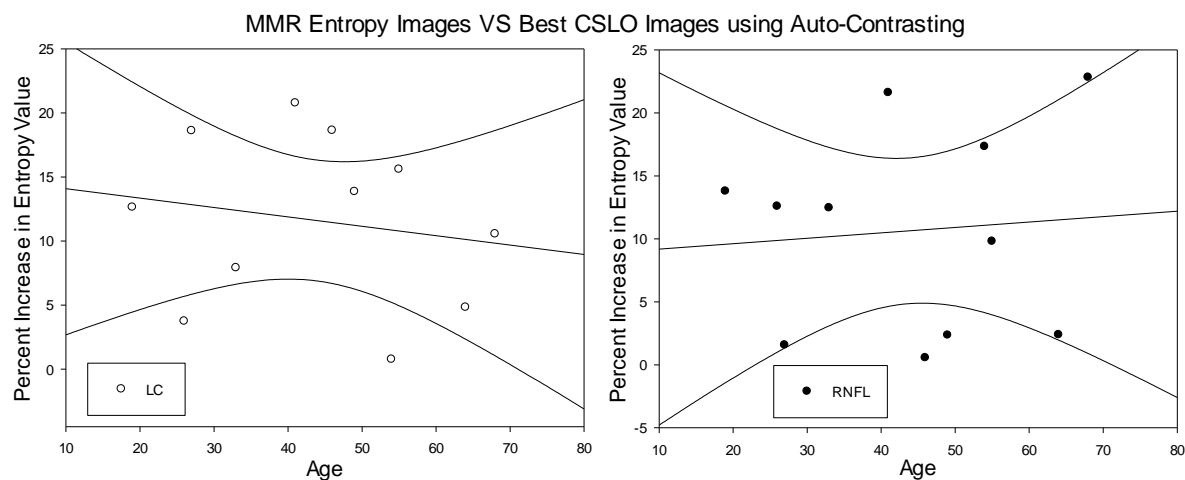


Figure 4.6: Percent improvement of MMR images over CSLO images as measured by entropy using auto-contrasted inputs at the LC (left) and RNFL (right) depths. Fits shown are not significant.

As with the original images, SNR again showed no significant linear relationship with age at the LC depth ($p = 0.68$, $R^2 = 0.02$) or at the RNFL depth ($p = 0.47$, $R^2 = 0.06$) (figure 4.7). The percent change in SNR showed all positive, significant increases across subjects (figure 4.28).

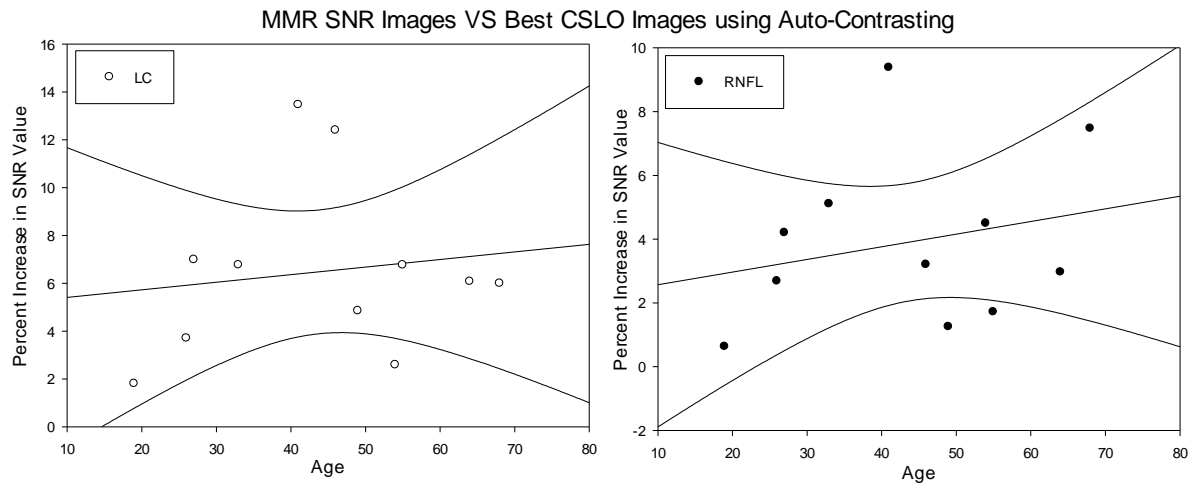


Figure 4.7: Percent improvement of MMR images over CSLO images as measured by SNR using auto-contrasted inputs at the LC (left) and RNFL (right) depths. Fits shown are not significant.

Sample images of both original CSLO and auto-contrasted CSLO images compared to MMR max entropy and max SNR images can be seen in figures 4.8 and 4.9.

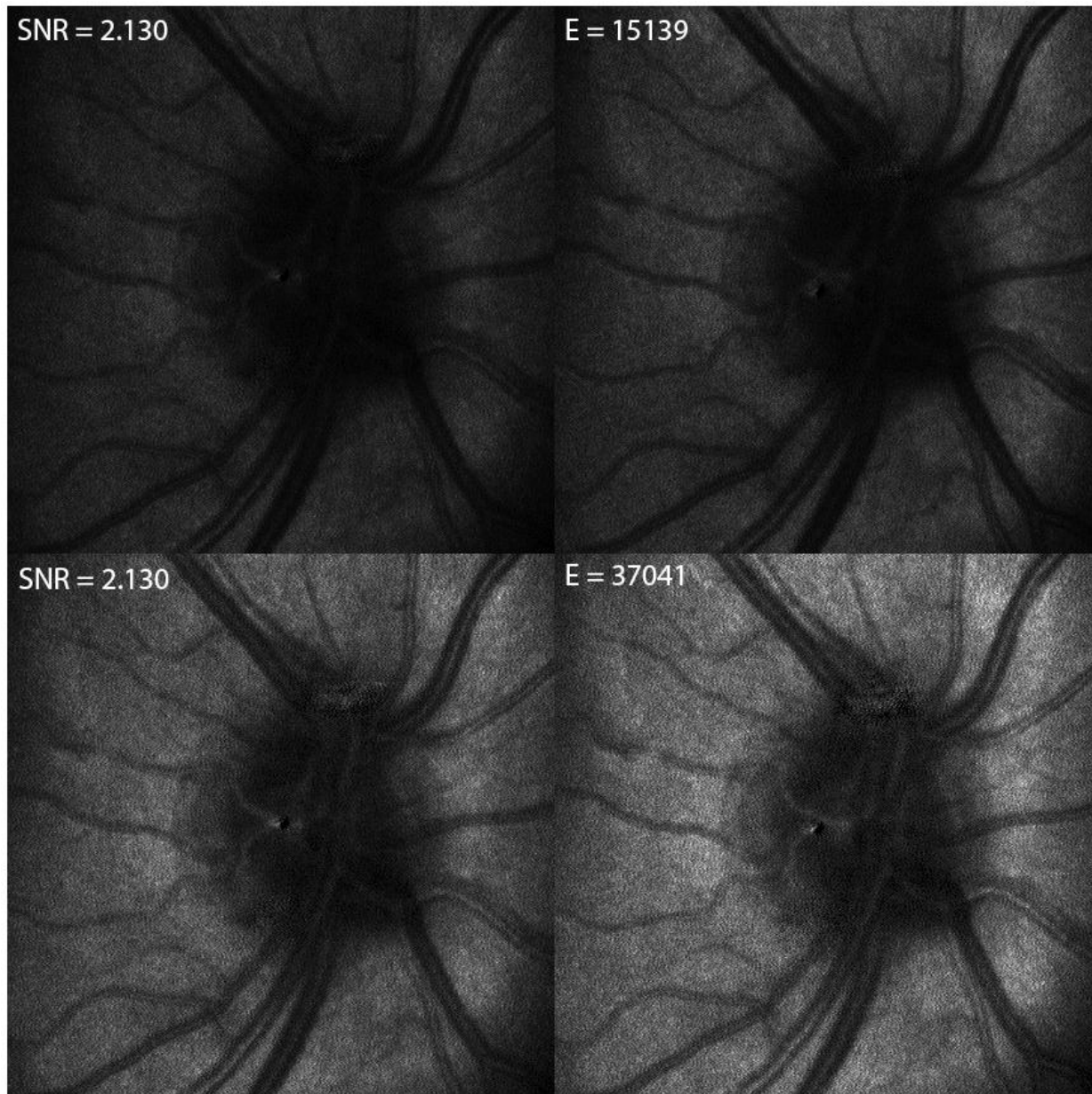


Figure 4.8: Best SNR CSLO image (top left), best entropy CSLO image (top right), Best auto-contrasted SNR CSLO image (bottom left), and best auto-contrasted entropy CSLO image (bottom right).

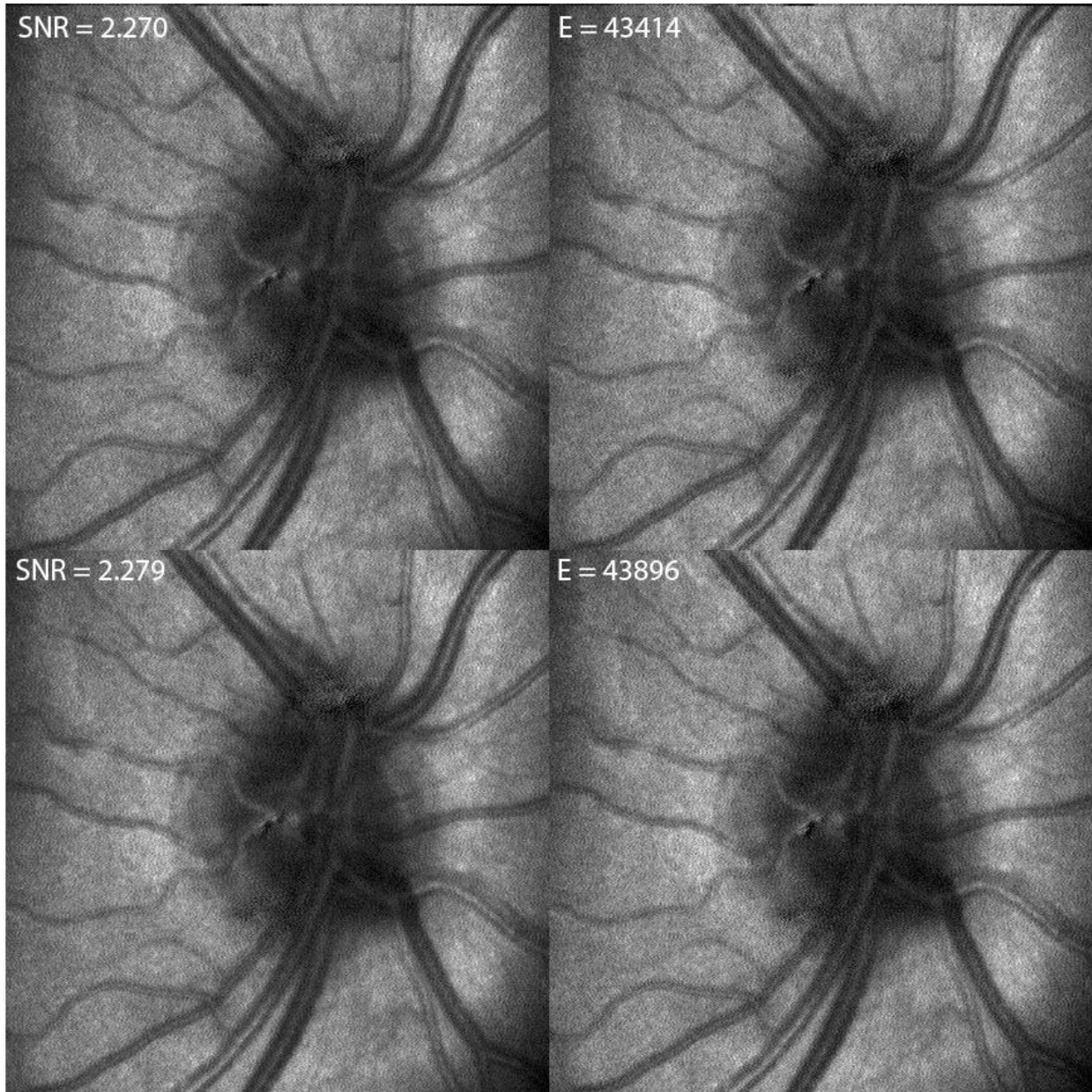


Figure 4.9: MMR max SNR image calculated from CSLO images (top left), MMR max entropy image calculated from the original CSLO inputs (top right), MMR max SNR image with auto-contrasted CSLO inputs (bottom left), MMR max entropy image with auto-contrasted CSLO inputs (bottom right)

4.4.2 Mueller matrix reconstruction VS Linear CSLO Image

Overall, Mueller matrix reconstruction methods showed a greater image quality improvement, again significant, when compared to the image formed by linearly polarized light

captured by the CSLO versus the best CSLO image (figures 4.26, 4.28), as expected, since the best CSLO image is guaranteed to perform equally or better than the linearly polarized image when quantified by either image quality metric.

Entropy (figure 4.10) did not show a significant linear relationship with age at the LC depth ($p = 0.08$, $R^2 = 0.30$) and an insignificant relationship at the RNFL depth ($p = 0.06$, $R^2 = 0.34$).

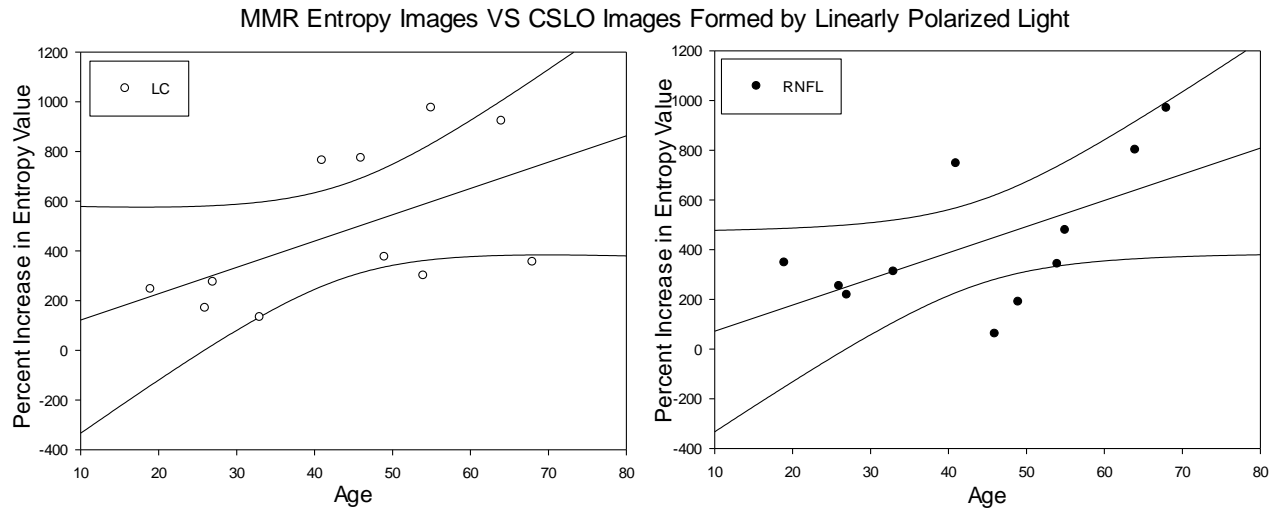


Figure 4.10: Percent improvement of MMR images over the CSLO image formed by linearly polarized light as measured by entropy at the LC (left) and RNFL (right) depths. The fits on the left and right are insignificant ($p=0.08$ and $p=0.06$).

SNR (figure 4.11) on average increased significantly but showed no significant linear relationship with age at the LC depth ($p = 0.50$, $R^2 = 0.05$) or the RNFL depth ($p = 0.73$, $R^2 = 0.01$).

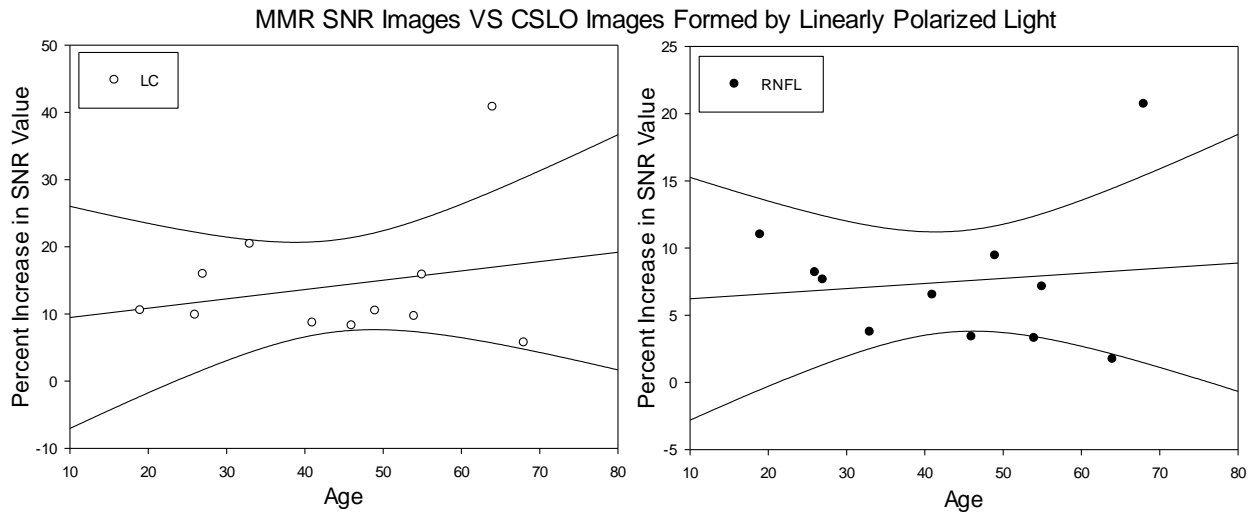


Figure 4.11: Percent improvement of MMR images over CSLO images formed by linearly polarized light as measured by SNR at the LC (left) and RNFL (right) depths. The fits shown are insignificant.

When auto-contrasted CSLO images are used as inputs into the MMR algorithm, the percent increase of image quality drops substantially for entropy but is significantly above zero (figures 4.12, 4.26). There is no significant linear relationship of percent increase in entropy with age at the LC depth ($p = 0.25$, $R^2 = 0.14$) or the RNFL depth ($p = 0.30$, $R^2 = 0.12$).

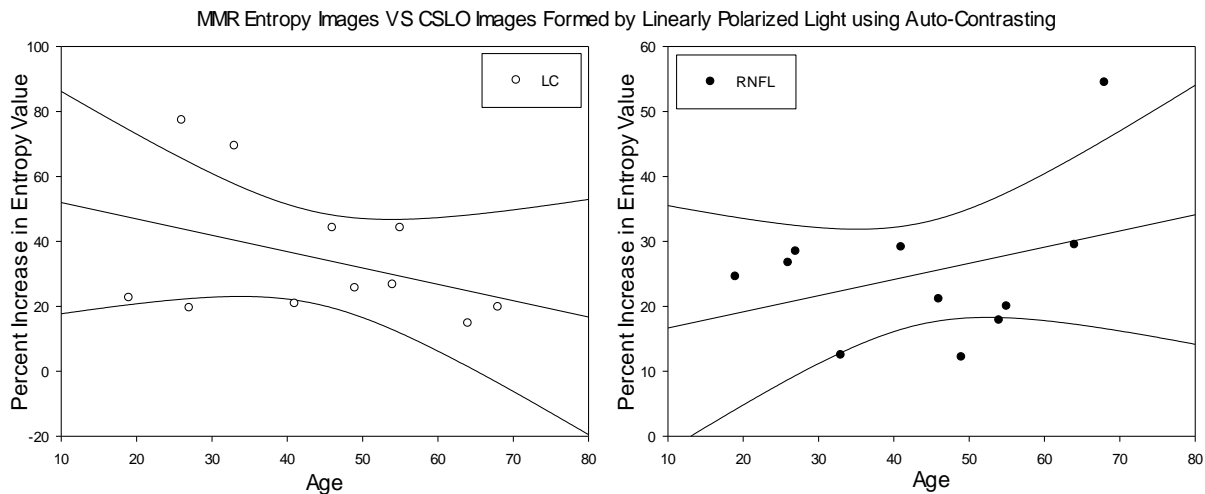


Figure 4.12: Percent improvement of MMR images over the CSLO images formed by linearly polarized light as measured by entropy at the LC (left) and RNFL (right) depths. Fits shown are not significant.

For SNR (figures 4.13, 4.28), no significance was found using the linear regression model at the LC depth ($p = 0.53$, $R^2 = 0.05$) or the RNFL depth ($p = 0.73$, $R^2 = 0.01$). The mean increase was significantly above zero.

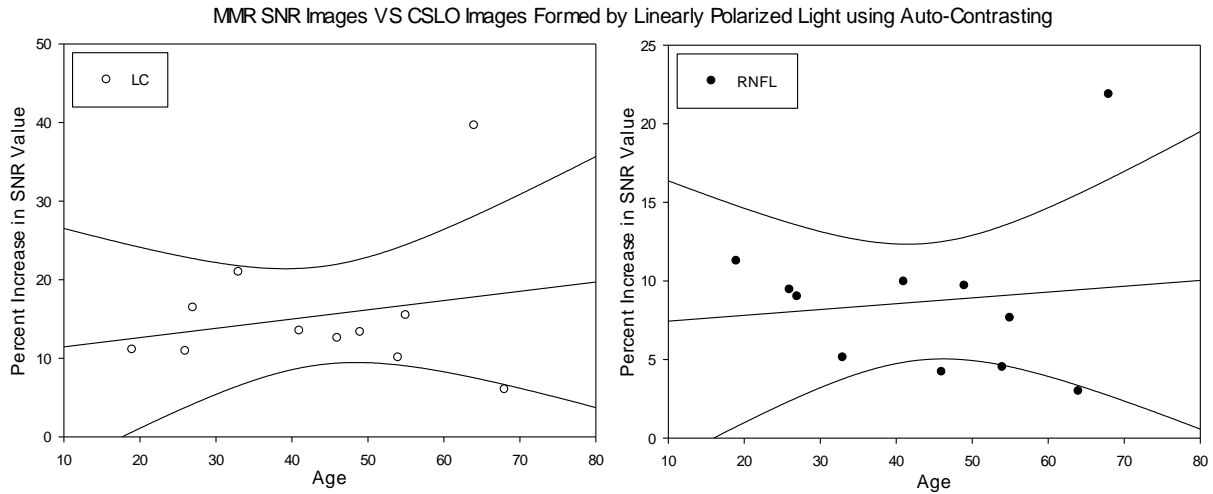


Figure 4.13: Percent improvement of MMR images over the CSLO images formed by linearly polarized light as measured by entropy at the LC (left) and RNFL (right) depths. Fits shown are not significant.

Sample CSLO images taken in linear input polarization for both original and auto-contrasted CSLO images can be seen in figure 4.14. Note that the output MMR max entropy and max SNR images are the same as those compared with the best CSLO image and can be seen in figure 4.9.

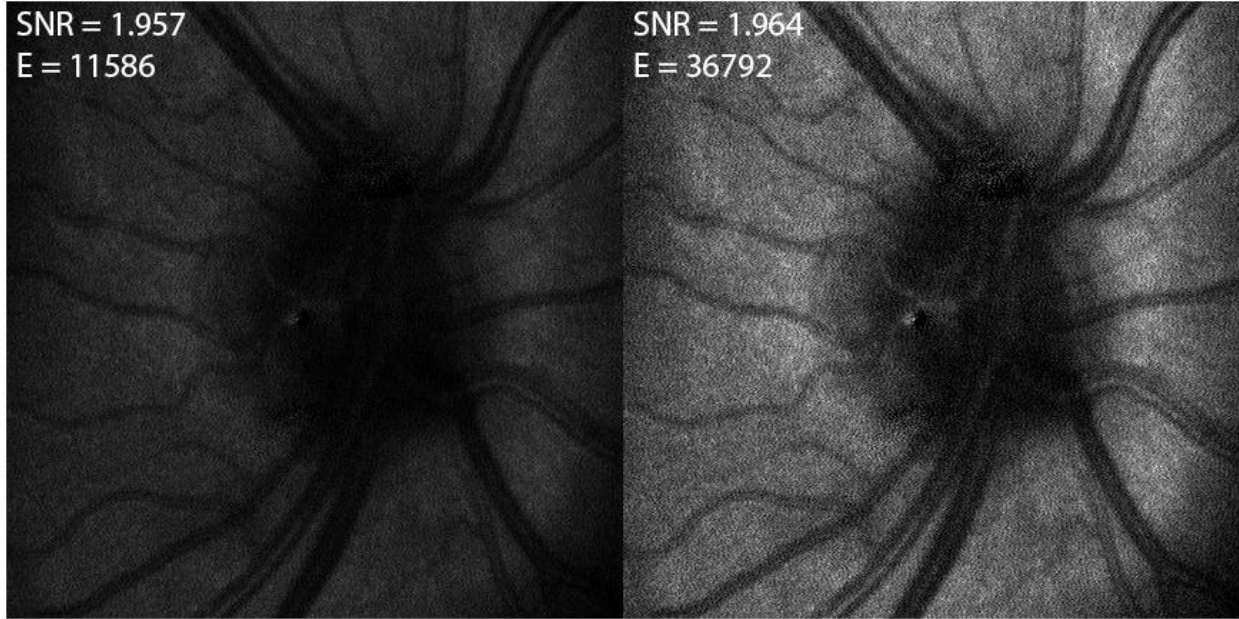


Figure 4.14: Original CSLO image formed by linearly polarized light (left), auto-contrasted CSLO image formed by linearly polarized light (right).

4.4.3 DOP_M VS CSLO Images

The Stokes vector reconstruction (SVR) method also yielded expected improved images when compared to raw CSLO images (no auto-contrasting). For the DOP_M image, a significant linear relationship between percent increase in entropy and age was not seen at the LC depth ($p = 0.16$, $R^2 = 0.21$) but was observed at the RNFL depth ($p = 0.046$, $R^2 = 0.37$) (figure 4.15). A linear relationship with age is expected as demonstrated by Bueno et al. [Bueno 2008]. The mean of the value at the LC depth was significantly above zero ($p = 0.03$, one sided t-test). The mean of the value at the RNFL depth was not significantly above zero ($p = 0.052$, one sided t-test).

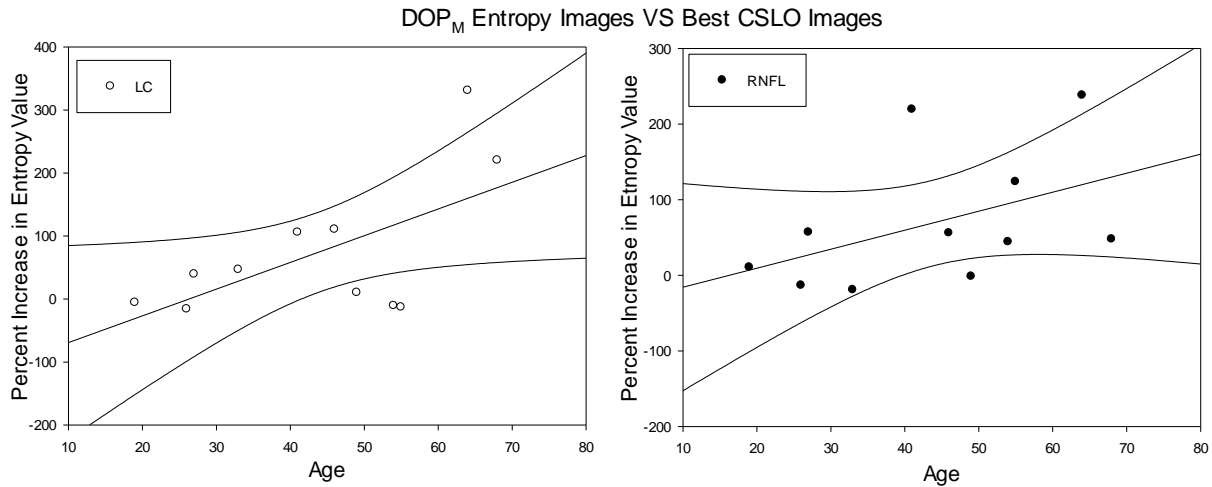


Figure 4.15: Percent improvement of DOP_M images over the best CSLO images as measured by entropy at the LC (left) and RNFL (right) depths. The fit shown on the left is not significant and that on the right is significant.

In terms of SNR, the DOP_M images showed no significant linear relationship with age at the LC depth ($p = 0.81$, $R^2 = 0.007$) or the RNFL depth ($p = 0.12$, $R^2 = 0.25$) (figure 4.16). The mean values at the LC and RNFL depths were significantly below zero ($p = 0.02$, and $p=0.001$, one sided t-test).

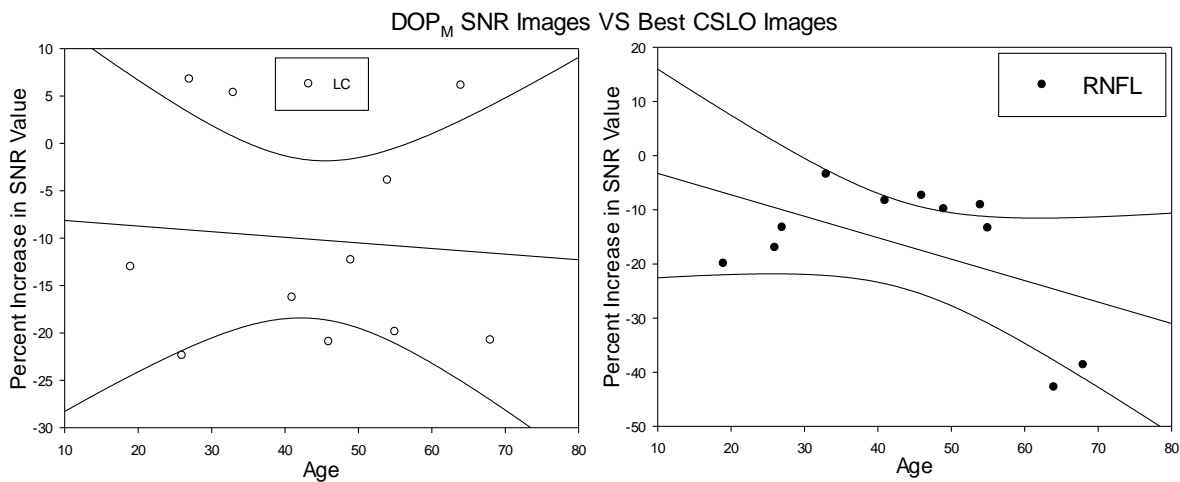


Figure 4.16: Percent improvement of DOP_M images over the best CSLO images as measured by SNR at the LC (left) and RNFL (right) depths. Fits shown are not significant.

When compared to the best auto-contrasted CSLO images, no significant linear relationship between percent increase in entropy value for DOP_M and age at the LC depth ($p = 0.66$, $R^2 = 0.02$) or the RNFL depth ($p = 0.23$, $R^2 = 0.15$). The mean of the value at the LC depth was not significantly below zero ($p = 0.06$, one sided t-test). The mean of the value at the RNFL depth was significantly below zero ($p = 0.02$, one sided t-test).

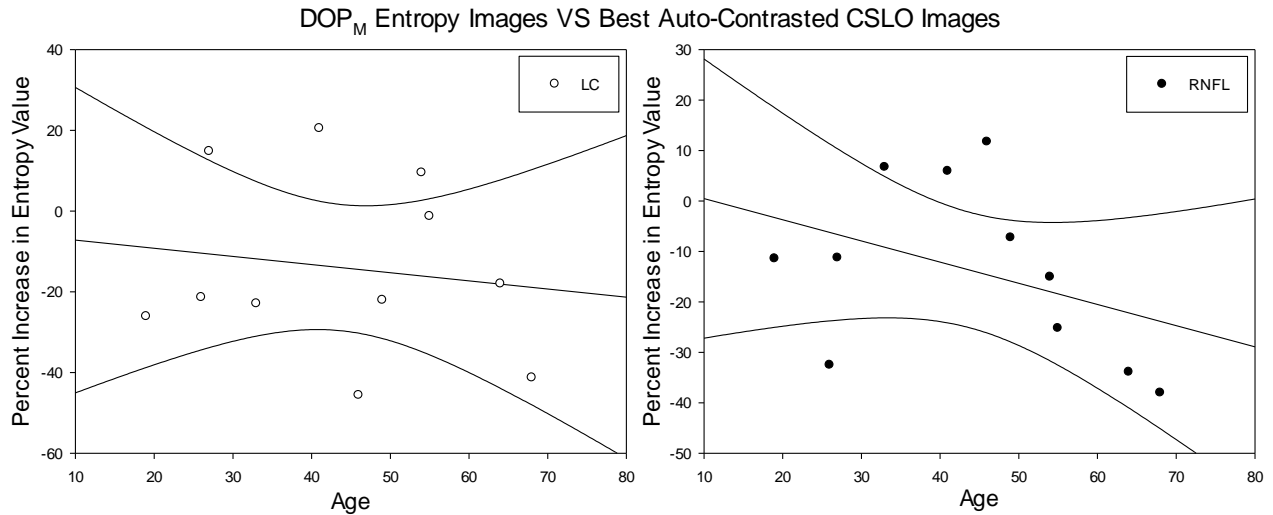


Figure 4.17: Percent improvement of DOP_M images over the best auto-contrasted CSLO images as measured by entropy at the LC (left) and RNFL (right) depths. Fits shown are not significant.

Against auto-contrasted images, no significant linear relationship with percent increase with SNR at the LC depth ($p = 0.08$, $R^2 = 0.30$) was found but the data does show a significant linear relationship with a decline in performance with age at the RNFL depth ($p = 0.03$, $R^2 = 0.40$) (figure 4.18). The mean of the value at the LC depth was significantly below zero ($p < 0.0001$, one sided t-test) as was the mean of the value at the RNFL depth ($p < 0.0001$, one sided t-test).

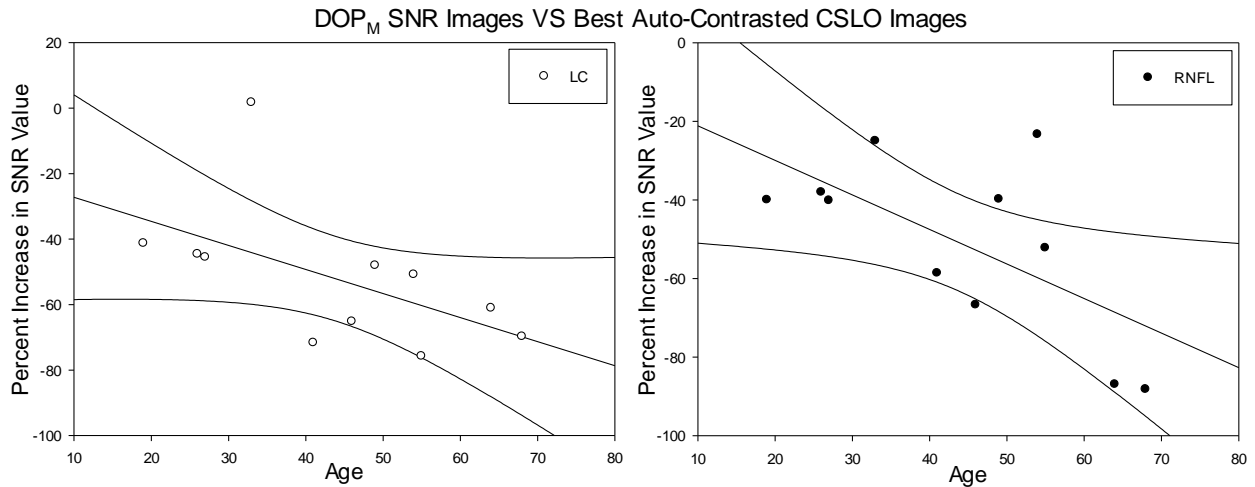


Figure 4.18: Percent improvement of DOP_M images over the best auto-contrasted CSLO images as measured by SNR at the LC (left) and RNFL (right) depths. The fit shown on the left is not significant and the one on the right is significant.

4.4.4 S₀ VS CSLO Images

As expected (Bueno, 2008), S₀ image quality quantified with entropy showed a significant improvement over the best CSLO images. No significant linear relationship was found at the LC depth ($p = 0.19$, $R^2 = 0.19$) but was found at the RNFL depth ($p = 0.04$, $R^2 = 0.39$) (figure 4.19). The mean of the value at the LC depth was significantly above zero ($p = 0.01$, one sided t-test) as was the mean of the value at the RNFL depth ($p = 0.02$, one sided t-test).

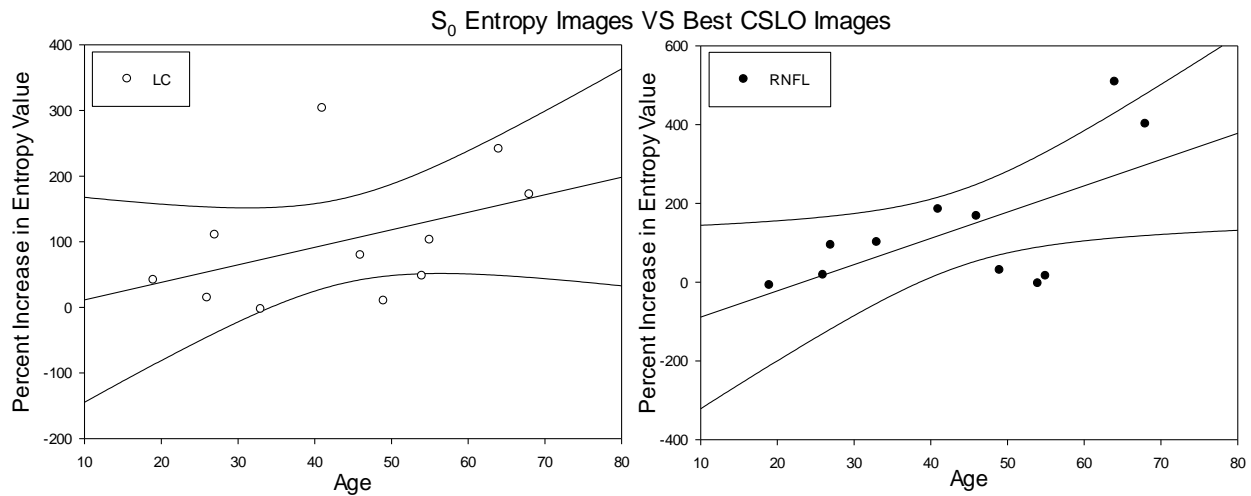


Figure 4.19: Percent improvement of S_0 images over the best CSLO images as measured by entropy at the LC (left) and RNFL (right) depths. The fit shown on the left is not significant and the one on the right is significant.

The data shows no significant linear relationship between percent increase in SNR and age at the LC depth ($p = 0.24$, $R^2 = 0.15$) but does show a significant linear relationship with decline in improvement for the RNFL depth images with age ($p = 0.03$, $R^2 = 0.42$) (figure 4.20). The mean of the value at the LC depth was significantly above zero ($p = 0.006$, one sided t-test). The mean of the value at the RNFL depth was not significantly above zero ($p = 0.63$, one sided t-test).

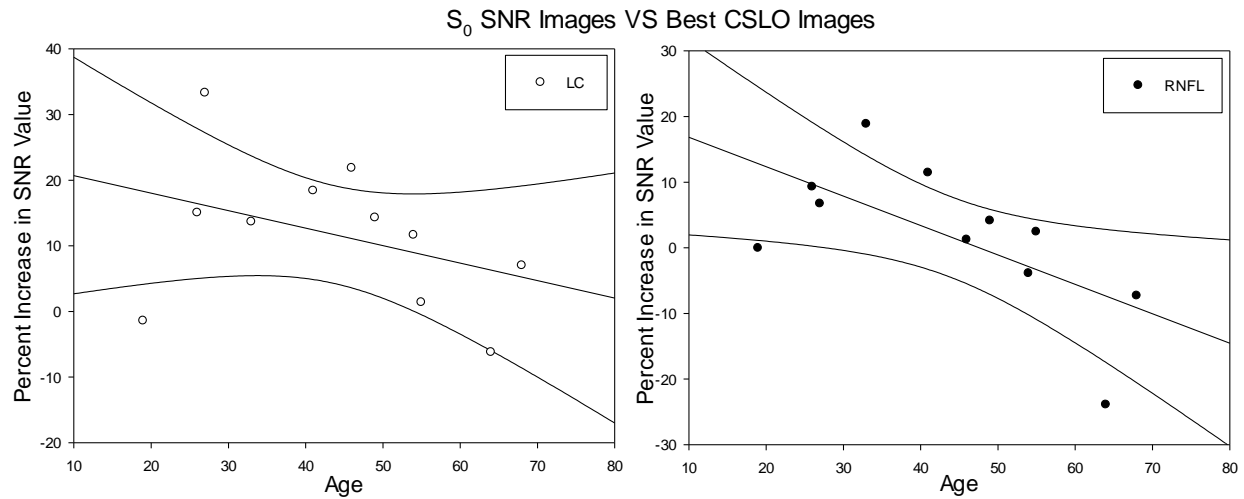


Figure 4.20: Percent improvement of S_0 images over the best CSLO images as measured by SNR at the LC (left) and RNFL (right) depths. The fit shown on the left is not significant and the one on the right is significant.

When compared to the best auto-contrasted CSLO images, entropy showed no significant relationship with age at the LC depth ($p = 0.43$, $R^2 = 0.07$) or the RNFL depth ($p = 0.56$, $R^2 = 0.04$) (figure 4.21). The mean of the value at the LC depth was not significantly above zero ($p = 0.69$, one sided t-test) nor was the mean of the value at the RNFL depth ($p = 0.13$, one sided t-test). The power was substantially below the desired value of 0.8. The test is unlikely to detect a difference when one actually exists.

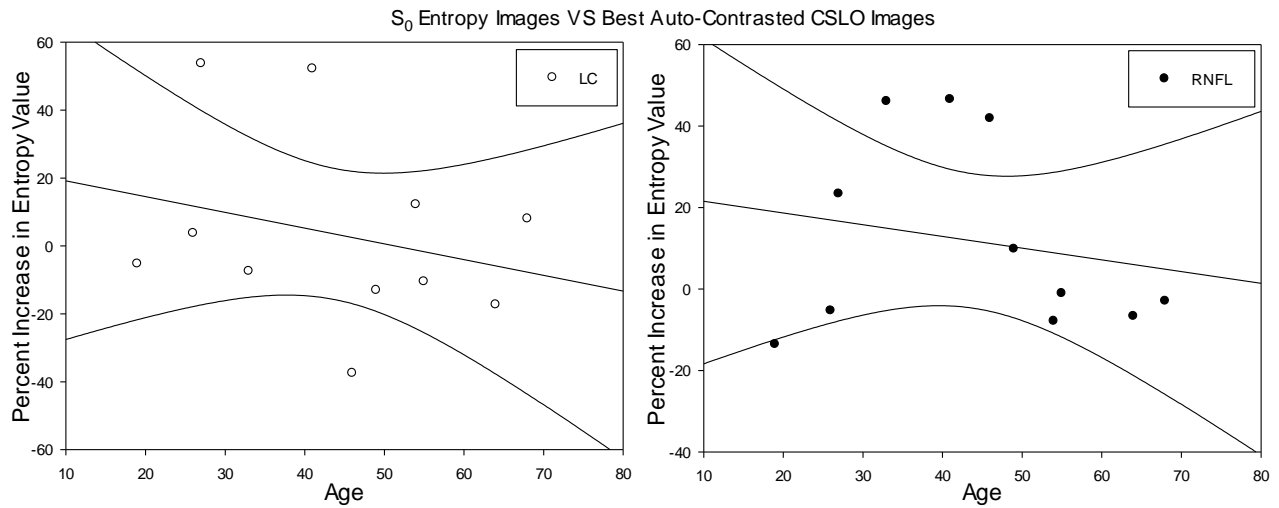


Figure 4.21: Percent improvement of S₀ images over the best auto-contrasted CSLO images as measured by entropy at the LC (left) and RNFL (right) depths. Fits shown are not significant.

When compared to the auto-contrasted CSLO image, there was a significant linear relationship of percent change in SNR value and age with a decline in improvement at both the LC depth ($p = 0.03$, $R^2 = 0.44$) and the RNFL depth ($p = 0.01$, $R^2 = 0.52$) (figure 4.22). The mean of the value at the LC depth was significantly below zero ($p < 0.0001$, one sided t-test) as was the mean of the value at the RNFL depth ($p < 0.0001$, one sided t-test).

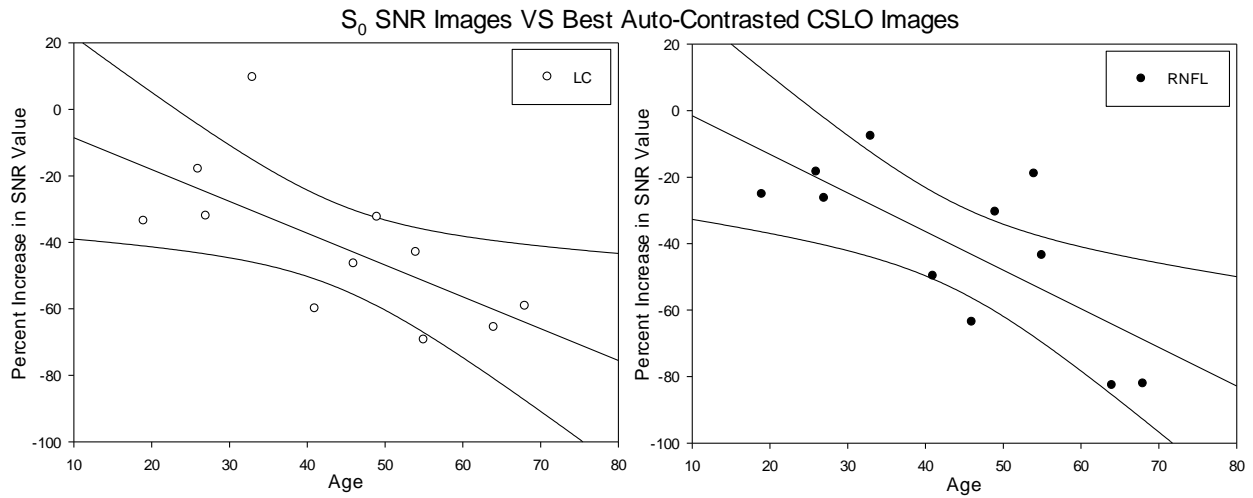


Figure 4.22: Percent improvement of S_0 images over the best auto-contrasted CSLO images as measured by SNR at the LC (left) and RNFL (right) depths. Both fits shown are significant.

Sample DOP_M and S_0 images can be seen in figure 4.23. Note that best entropy and SNR images for original and auto-contrasted CSLO images can be seen in figure 4.8.

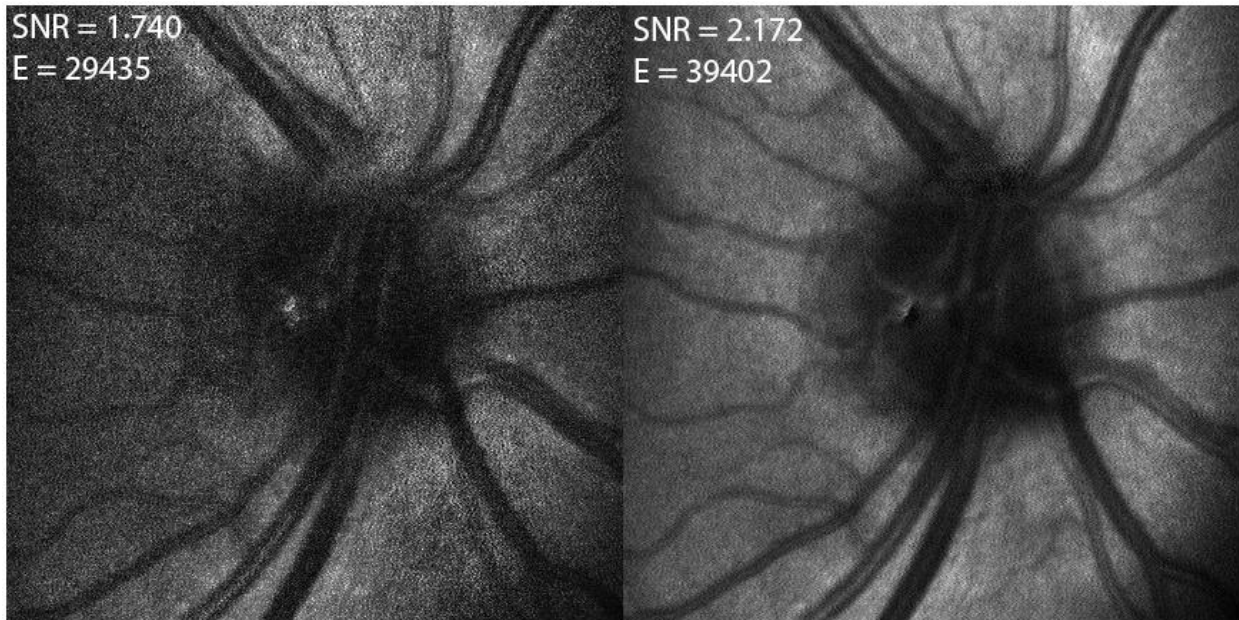


Figure 4.23: DOP_M image (left), and S_0 image (right).

4.4.5 Auto-Contrasted MMR Inputs Increase max SNR and Entropy Values

An important side-effect to the reassessment of MMR was that inputting auto-contrasted CSLO images into the MMR algorithm, in the majority of cases, improved the SNR and entropy values of the max SNR and max entropy images compared to those generated when the original CSLO images were inputted. Below is a graph showing the differences between the two sets of reconstructed images (figure 4.24) for the two different inputs.

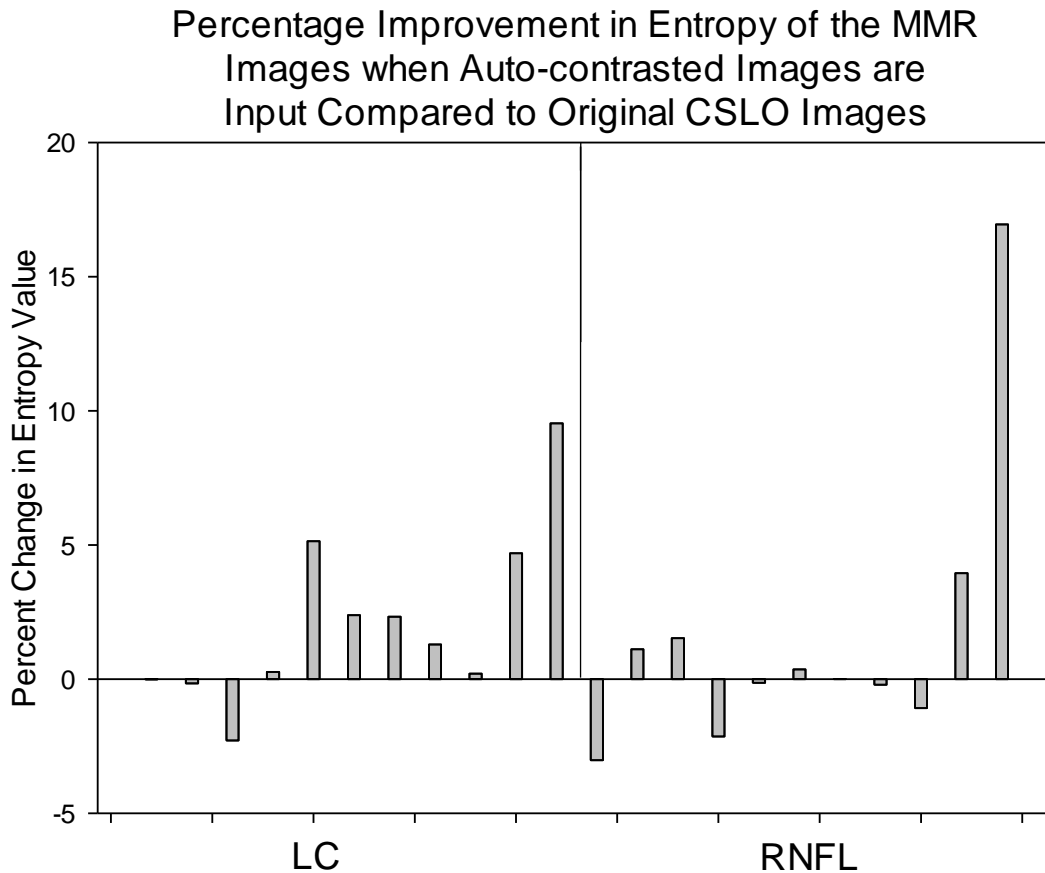


Figure 4.24: Performance increase of the max entropy image produced by MMR when inputting auto-contrasted CSLO images instead of original CSLO images. The increase in performance was not significantly greater than zero ($p = 0.06$).

The metric value of entropy was not always increased when inputting auto-contrasted images compared to the result against original images but the mean value was increased insignificantly by 4% across all participants ($p = 0.06$). This might become significant with more subjects.

The SNR value was always increased when inputting auto-contrasted images instead of the original images and the mean value of SNR was increased significantly by 53% across all participants ($p < 0.0001$) (figure 4.25).

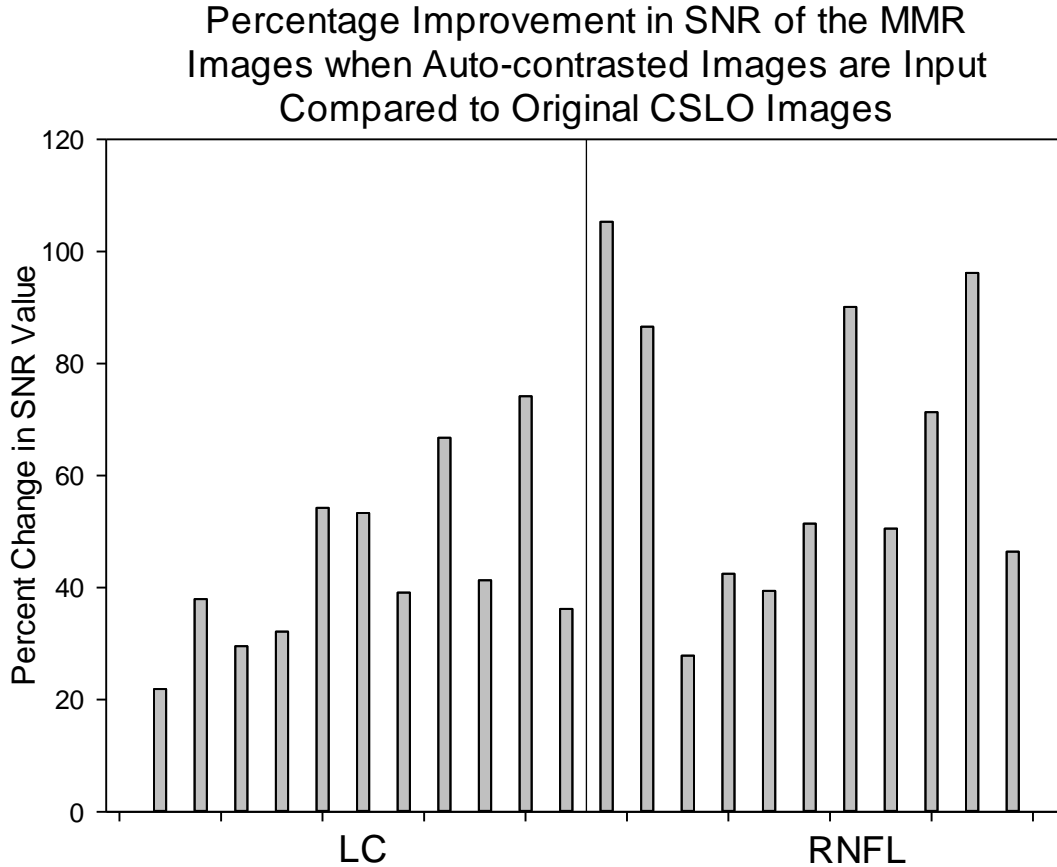


Figure 4.25: Performance increase of the max SNR image produced by MMR when inputting auto-contrasted CSLO images instead of original CSLO images. The increase in performance was significantly greater than zero ($p < 0.0001$).

4.4.6 Average Image Quality Improvement

When quantified with entropy, the average percent change in image quality achieved by the Mueller matrix reconstructed image when compared to the best CSLO image fell significantly from 158% to 11% when the input images were auto-contrasted (figure 4.26). A paired t-test of percent increase in entropy value compared with best auto-contrasted and best original CSLO images failed a normality test. A signed rank test was performed instead ($p < 0.001$). When compared to the linearly polarized CSLO image, the percent change in entropy dropped

significantly from 454% to 29% when the initial images were auto-contrasted (figure 4.26). A paired t-test of percent increase in entropy value between using auto-contrasted and original CSLO images formed by linearly polarized light failed a normality test. A signed rank test was performed instead ($p < 0.001$).

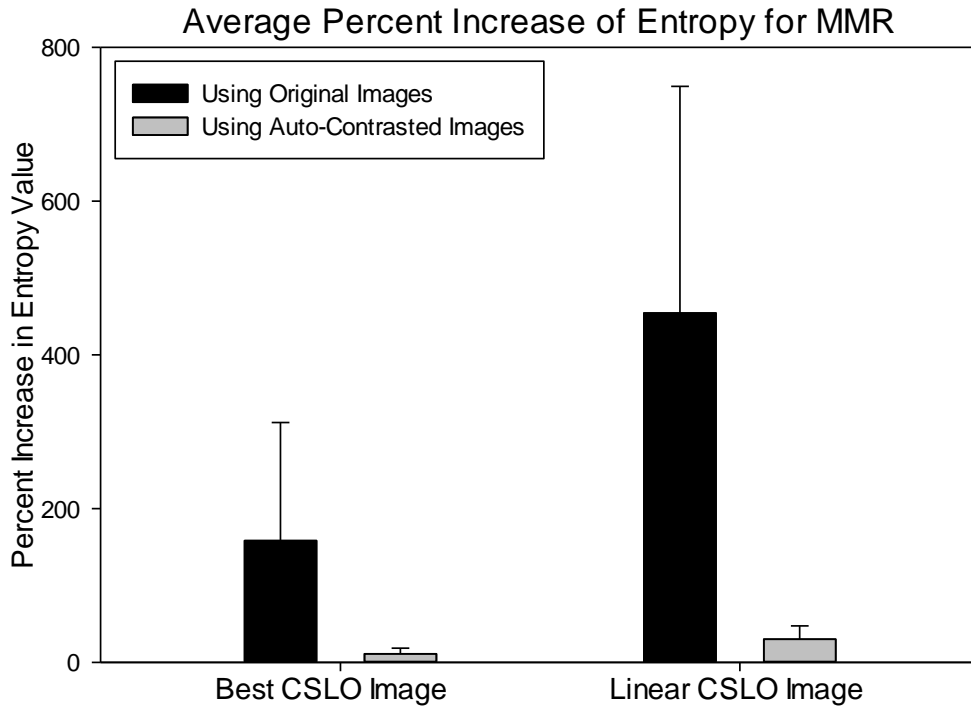


Figure 4.26: Average percent increase in entropy value of MMR images when using original (black) and auto-contrasted (grey) CSLO images. Error bars shown are standard deviations of the percent increase in entropy value across all participants.

The average image quality improvements for SVR were mixed (figure 4.27). In terms of entropy, the average value of percent change across all participants dropped significantly from 71% to -13% for the DOP_M image when auto-contrasted images were used in place of the original images. A paired t-test of percent increase in entropy value between best auto-contrasted and best original CSLO images failed a normality test. A signed rank test was performed instead ($p < 0.001$). For the S_0 image, the percent change in entropy value dropped significantly from 119% to 7% when compared to best auto-contrasted CSLO images instead of best original CSLO images. A paired t-test of percent increase in entropy value between best auto-contrasted and

best original CSLO images failed a normality test. A signed rank test was performed instead ($p < 0.001$).

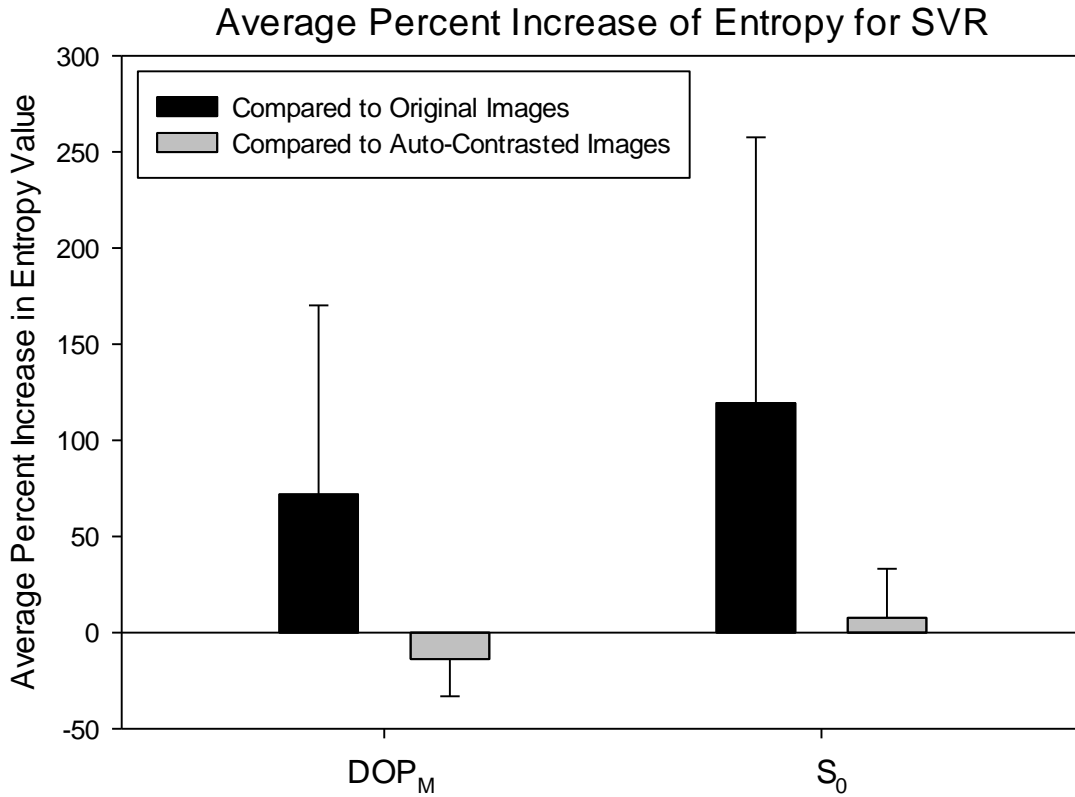


Figure 4.27: Average percent increase or decrease in entropy value of SVR images when compared to original (black) and auto-contrasted (grey) CSLO images. Error bars shown are standard deviations of the percent change in entropy value across all participants.

When quantified with SNR, MMR performed very well (figure 4.28). In fact, it can be seen that the percent possible improvement of image quality was being underestimated when using original CSLO images instead of auto-contrasted CSLO images.

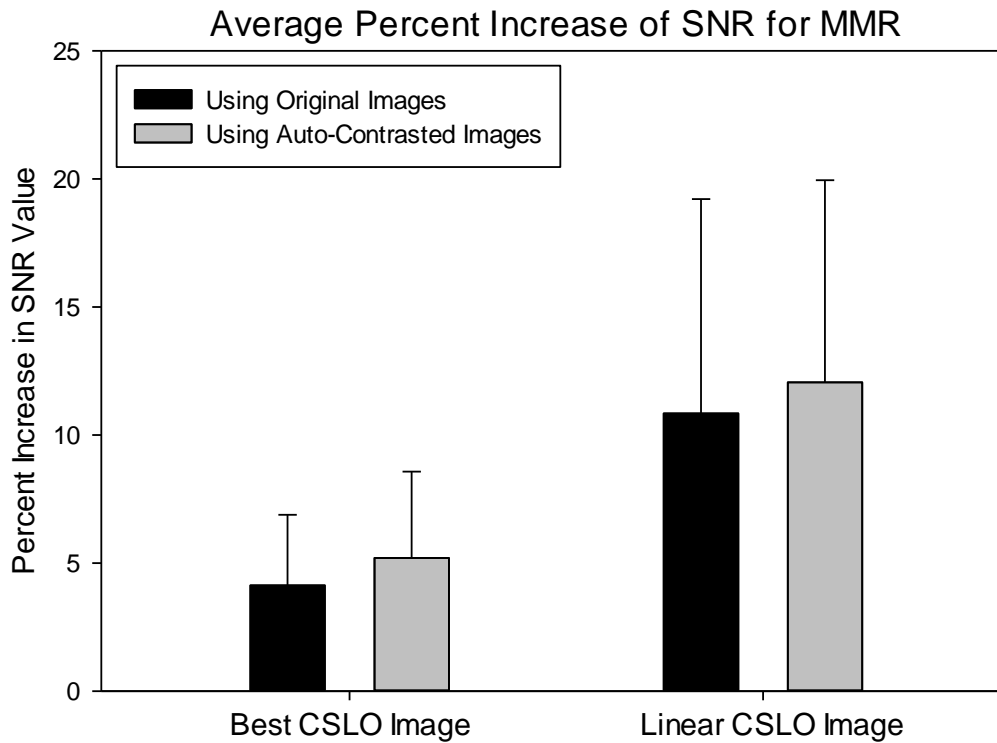


Figure 4.28: Average percent increase in SNR value of MMR images when using original (black) and auto-contrasted (grey) CSLO images. Error bars shown are standard deviations of the percent increase in SNR value across all participants.

When compared with the best CSLO image, average percent increase in SNR value increased significantly from 4% to 5% when inputting auto-contrasted CSLO images instead of original CSLO images. A paired t-test of percent increase in entropy value between best auto-contrasted and best original CSLO images failed a normality test. A signed rank test was performed instead ($p = 0.002$). When measured against the linearly polarized CSLO image, average SNR values increased significantly from 10% to 12% when inputting auto-contrasted CSLO images instead of original CSLO images. A paired t-test of percent increase in SNR value between results with auto-contrasted and original CSLO images formed by linearly polarized light failed a normality test. A signed rank test was performed instead ($p < 0.001$).

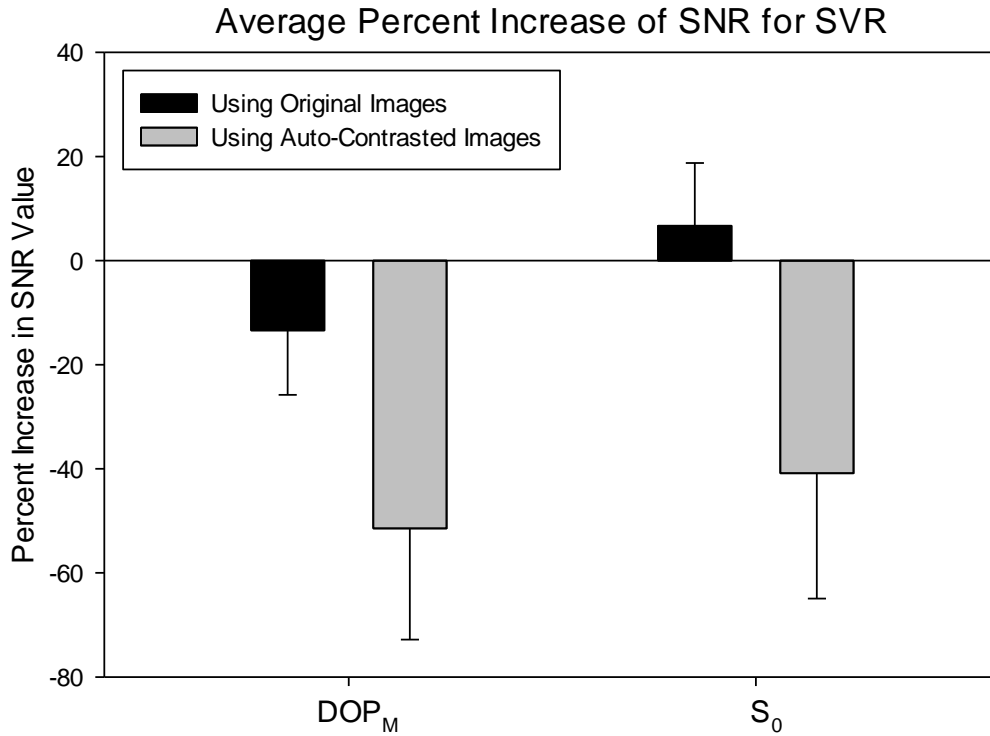


Figure 4.29: Average percent change in SNR value of SVR images when compared to original (black) and auto-contrasted (grey) CSLO images. Error bars shown are standard deviations of the percent change in SNR value across all participants.

When compared to the auto-contrasted image, average percent decrease in SNR for the DOP_M image dropped from -13% to -51% when compared to the best auto-contrasted CSLO image instead of the best original CSLO image ($p < 1 \times 10^{-9}$, paired t-test) (figure 4.29). The average percent change in SNR of the S_0 image fell significantly from 7% to -41% when compared to the best auto-contrasted CSLO image instead of the best original CSLO image ($p < 1 \times 10^{-9}$, paired t-test).

4.4.7 Correlation between Auto-contrasting and Entropy Image Quality Improvement

A particularly interesting result, when comparing performance of original and auto-contrasted images, is the disappearance the increase of the percentage change in entropy with age which was seen in entropy measurements of both Mueller matrix and Stokes vector reconstruction which is seen when original images are inputted. The reason MMR using entropy

shows increased performance with age when compared to original images (not auto-contrasted) may be due to the fact that image quality diminishes with age [Fujikado, 2004], [Kuroda, 2002] often resulting in darker, lower contrast images. Since older participants produce darker images, there is more room in terms of the dynamic range of the pixel intensity for the auto-contrast to effectively improve image quality.

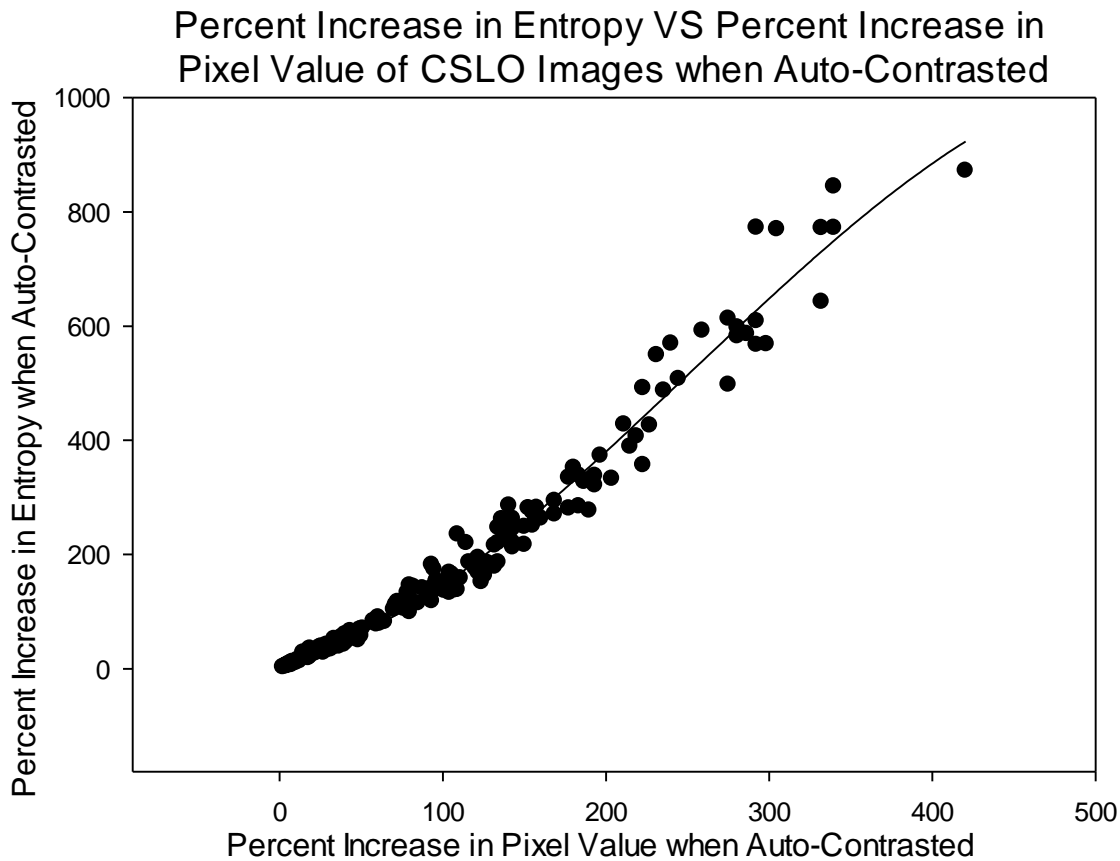


Figure 4.30: Correlation between percent increase in entropy of an image versus the percent increase in max pixel value of the same image when that image is auto-contrasted. A significant cubic fit is shown ($p < 0.0001$, $R^2 = 0.9762$).

To demonstrate this, consider the given graph of percent increase in entropy versus percent increase in pixel value when each image of the 176 CSLO images used in this study is auto-contrasted (figure 4.30). When fit with a cubic polynomial, the correlation is strongly significant ($p < 0.0001$, $R^2 = 0.98$). The R^2 value for a fit to a cubic term is greater than the R^2 value for the linear fit. The fit verifies that the more space there is to auto-contrast an image, the greater the increase in that image’s measured entropy value. Now consider the following graph of the

absolute difference in entropy value versus the absolute difference in pixel value when each image is auto-contrasted of all 176 images (figure 4.31). A significant relationship is observed ($p < 0.0001$, $R^2 = 0.78$).

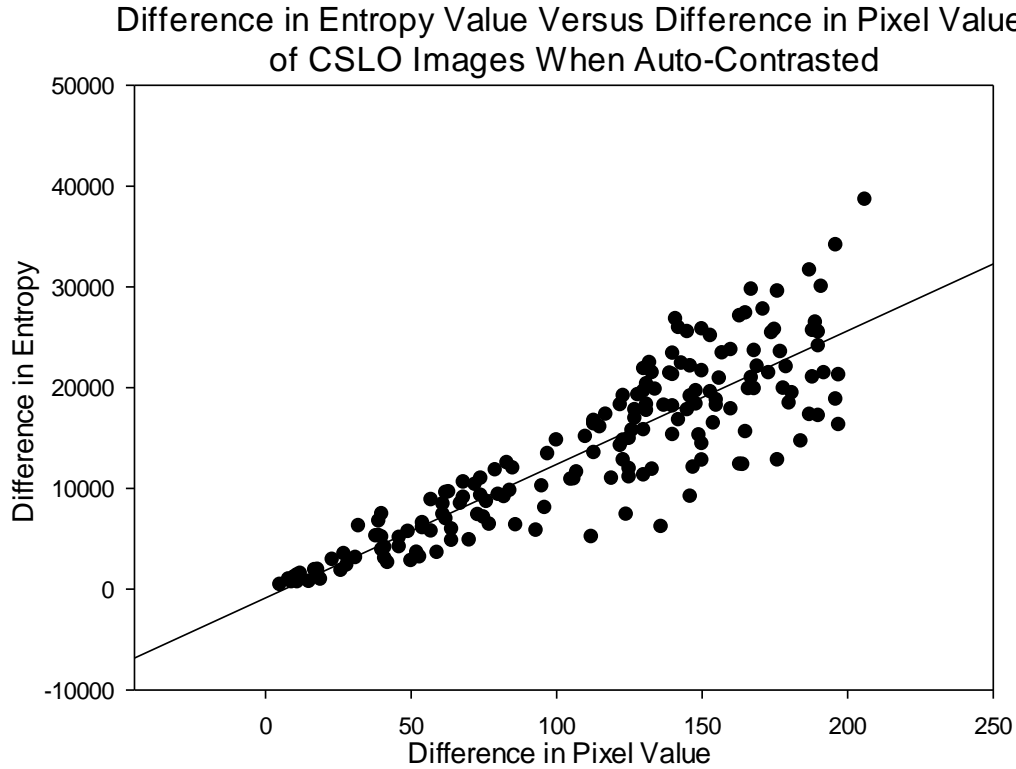


Figure 4.31: Difference seen in entropy value versus the difference in pixel value of an image when it is auto-contrasted. The fit shown is significant.

This graph shows that for some images, the increase in entropy can be near 40000 when an image is auto-contrasted with a mean entropy increase of 13944. This is substantial as the best CSLO image across all 176 images has an entropy value of 44471 with a mean of 25917 across all images.

Next, consider figure 4.32 which shows the significant decrease with age ($p = 0.01$, $R^2 = 0.59$) of the mean maximum pixel values averaged over across the 16 images acquired from each of the 11 participants. Recall that each participant had 4 images acquired for MMR and 4 images acquired for SVR at 2 imaging depths. This gives each participant a total of 16 CSLO images.

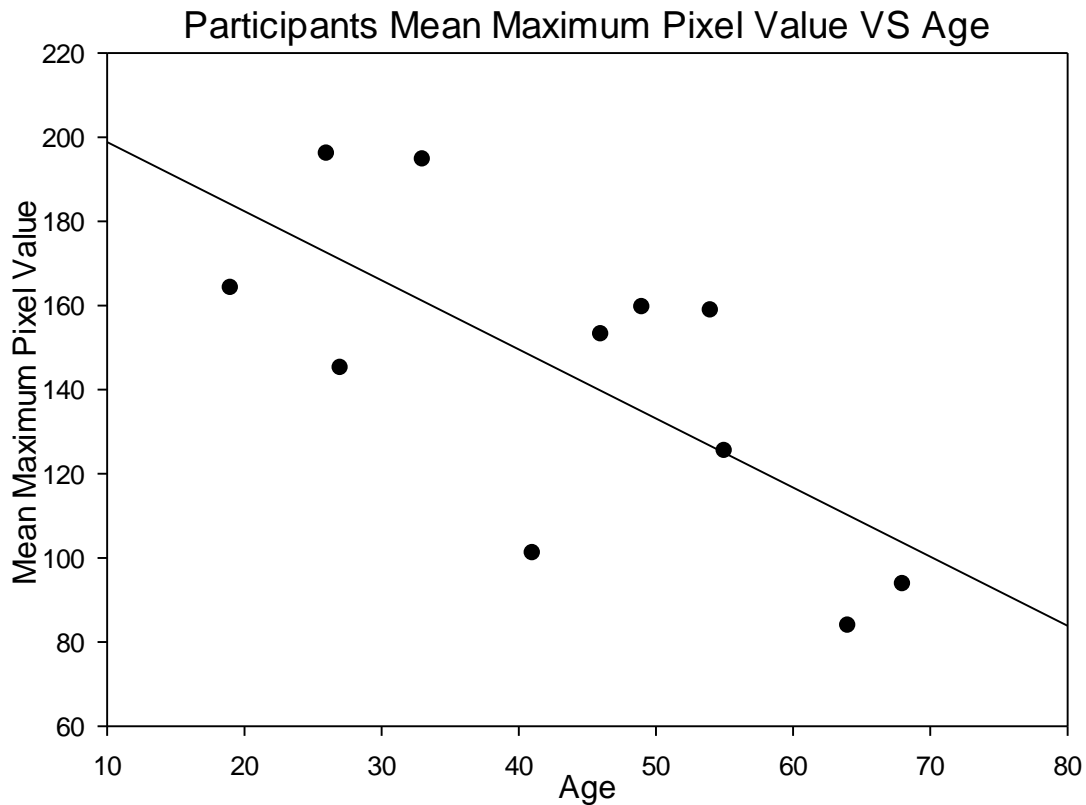


Figure 4.32: Mean maximum pixel value taken across each participant’s 16 CSLO images as a function of age. The fit shown is significant.

This graph shows a clear decrease in the average maximum pixel value as age increases. This leaves more dynamic range for an auto-contrasting to stretch the pixel values up to the maximum value of 255, allowing auto-contrasting of images to raise entropy values considerably with age.

Next, consider a plot of the mean change in pixel value when an image is auto-contrasted as a function of age (figure 4.33). This graph shows a significant correlation in the increase in pixel value when an image is auto-contrasted as a function of age ($p = 0.02$, $R^2 = 0.48$).

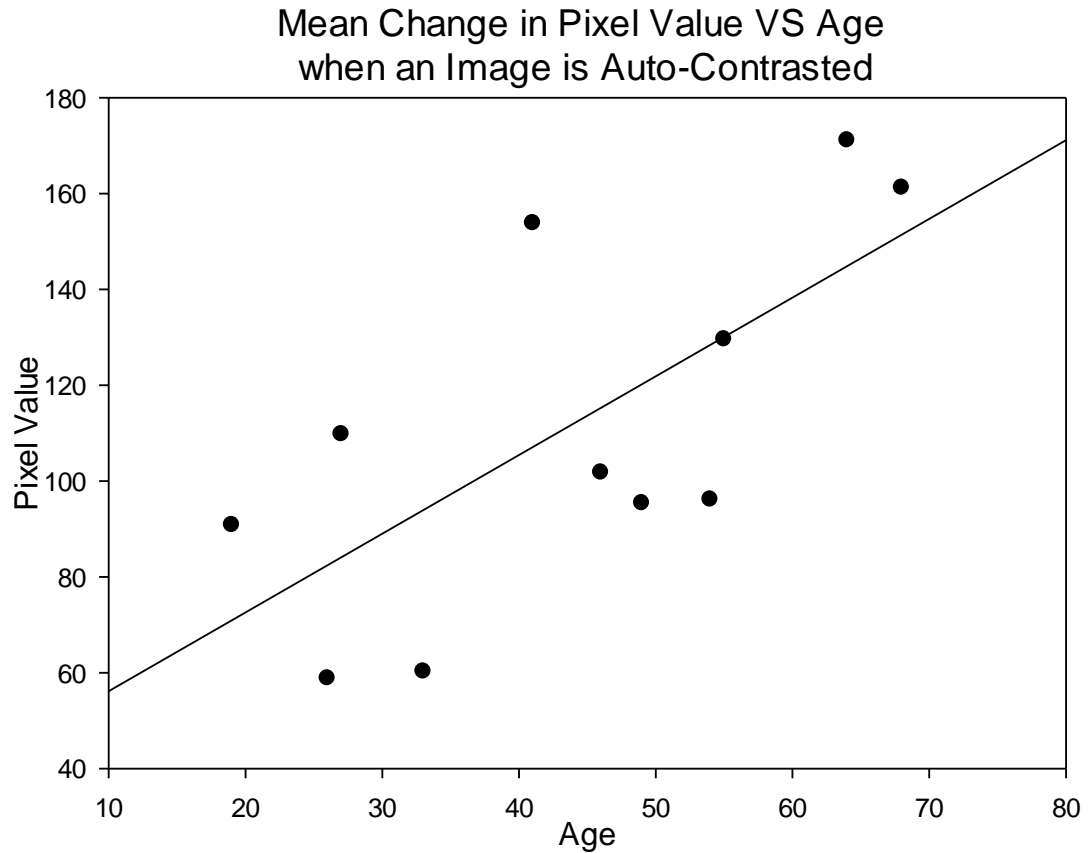


Figure 4.33: Increase in mean maximum pixel value when an image is auto-contrasted as a function of age. The fit shown is significant.

Finally, consider a plot of the mean change in absolute entropy value as a function of age when an image is auto-contrasted (figure 4.34).

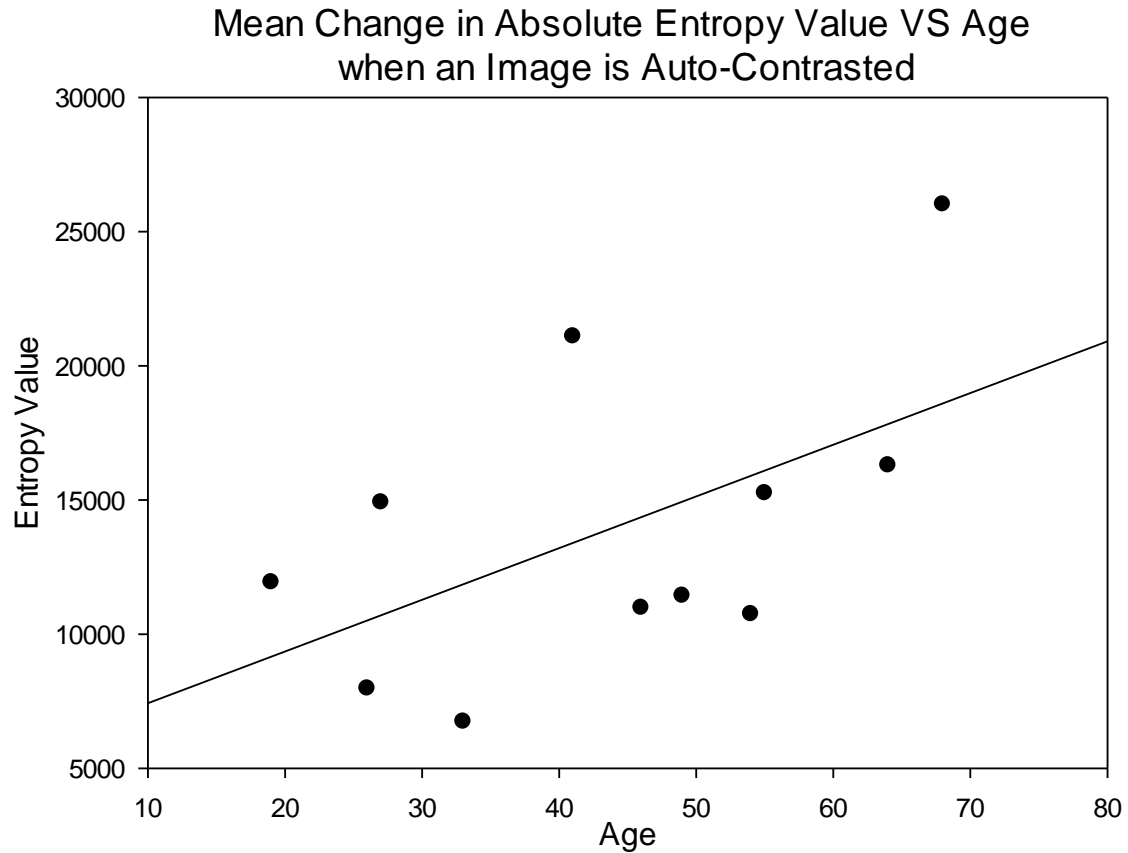


Figure 4.34: Increase in mean maximum pixel value when an image is auto-contrasted as a function of age. The fit shown is not significant.

The evidence for a mean increase in entropy value when an image is auto-contrasted as a function of age is not conclusive, the correlation is not significant ($p = 0.08$, $R^2 = 0.30$). A larger sample size may make this correlation significant since the power of this test was not high. In order to reach significance (power of 0.8), the sample size is estimated at 24 participants.

4.4.8 DOP*S₀ and DOP_M Comparison

Both the DOP_M and DOP*S₀ images produced similar SNR and entropy values (figure 4.35) as expected (equation 4.18). The DOP_M image when quantified yielded an SNR value of 1.74 while the DOP*S₀ image gave a value of 1.78. In terms of entropy, DOP_M gave a value of 29435 while the DOP*S₀ had a value of 27704. Therefore the performance of the two processing algorithms is similar and which image improves image quality the most is dependent on the metric chosen to quantify it.

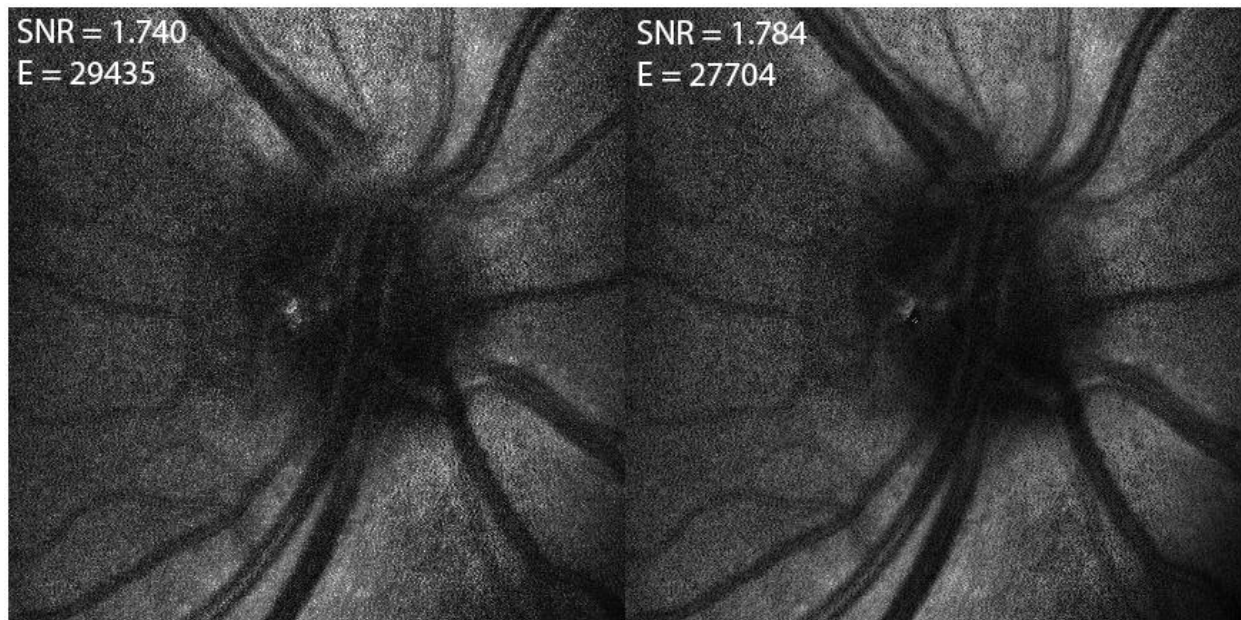


Figure 4.35: DOP_M image compared to DOP*S₀ image with SNR and entropy values.

4.5 Conclusions

Previous reports of these techniques applied to retinal images by Bueno et al. (2007, 2009b) and the image quality improvements quantified by entropy and SNR have shown increases in image quality using both metrics. It was also concluded that both S₀ and DOP_M showed increased image quality with age [Bueno, 2008], although further analysis has shown borderline significance for the participants in that study (personal communication). The increase in image quality of S₀ and DOP with age shown here was initially thought to be due to the methods

countering the degradation of image quality caused by increasing scatter with age [Bueno, 2008]. It may also be due to adjacent structures having differing depolarising [properties which are known to increase with age. In this work, original CSLO images (not auto-contrasted) were input into MMR and SVR enhancement algorithms and showed results similar to previous studies. As expected, reconstructed images from MMR and SVR showed strong improvements over the originals and dependence with age (in terms of entropy) that would be greatly beneficial to images of eyes in the aging population. Because of the low power of the test for mean improvements of DOP_M and S_0 as a function of age when original images are inputted, the sample size should be increased.

The MMR calculation normalizes images at the end of the algorithm. The SVR calculation normalizes S_0 and stretches S_1 , S_2 , S_3 using the maximum pixel value across the entire S_0 image and auto-contrasts DOP_M at the end of the algorithm. By normalizing the input images, one compensates for the reduced dynamic range in some of the images in the top row of the Mueller matrix and the reduction in the dynamic range of these images as a function of age. This compensation is not possible when calculating an explicit polarization property (like DOP or S_0) as the absolute relationship between intensity values for different Mueller matrix elements is lost. However, Bueno's SVR algorithm views auto-contrasted DOP and S_0 images. The auto-contrasting of the input images allowed a more direct comparison of their image quality and that of the final images which had been either auto-contrasted (SVR) or normalized (MMR).

In terms of image quality quantified by entropy, Mueller matrix reconstruction reconstruction significantly improved image quality of an average of 11% when compared to auto-contrasted CSLO images. - When compared to linearly polarized auto-contrasted images, MMR showed a larger significant improvement of 29% in image quality. MMR reconstruction with auto-contrasted images sometimes produced better and sometimes worse results than MMR with the original CSLO images. As far as possible, the dynamic range of the images should be increased when they are collected by increasing the incident light intensity.

The usefulness of Stokes vector reconstruction in terms of entropy when compared with auto-contrasted input images was not obvious with the DOP_M image having a negative average percent change for RNFL images and a borderline percentage change for LC images when measured by entropy. The entropy of the S_0 image had a non-significant percentage change for

both LC and RNFL images when compared to auto-contrasted initial images. This puts Stokes vector reconstruction at a significant disadvantage when compared to Mueller matrix reconstruction as each image would need to be checked to ensure that the final result is actually an improvement in image quality. In addition, SVR images always have reduced intensity versus images taken without an analyzer. However, Both DOP_M and S_0 images still have value as an image quality improvement technique, still improving image quality for some participants. Any improvement of image quality in entropy should not be ignored as studies have shown that clinician image preference correlates with images with higher entropy values [Hutchings, 2006].

In terms of SNR, MMR images when compared with auto-contrasted images showed a small significant increase in image quality enhancement while DOP_M and S_0 showed a significant decrease in image quality for the both the LC and RNFL images with a significant decline with age for the S_0 image when compared to auto-contrasted CSLO images. This is not surprising as even before auto-contrasting the CSLO images, Stokes vector reconstruction resulted in a significant increases in image quality when quantified with SNR only for S_0 measured for LC images.

Interestingly, MMR image quality enhancement showed an increase in absolute value of entropy and SNR when auto-contrasted images were input into the MMR algorithm compared to non auto-contrasted inputs for all participants for SNR and some participants for entropy. Mean SNR was increased significantly from 1.39 to 2.13 across all participants. It is recommended that the maximum SNR image always be found by inputting auto-contrasted CSLO images. Since entropy did not always produce an increase in value, it is recommended that the maximum entropy image be found using both original CSLO images and auto-contrasted images, and the image resulting in the highest metric value be chosen. As a future recommendation, it would be relevant to acquire images in the CSLO without holding the power constant at the eye but instead always maximizing the dynamic range of the system (that is, always adjusting the power (within the ANSI standard safety limits) so at least one pixel value equals 255 within the image). This has the potential to produce even better results than inputting auto-contrasting images as it will produce a similar result to auto-contrasting but with small step sizes between pixel values (since there is now no longer a need to stretch the pixel values from 0 to 255). Although maximum entropy images for both techniques produced image quality improvements, once MMR and SVR

were assessed against auto-contrasted images, any significant improvement found with age disappeared. This is hypothesized to be due to a correlation found between auto-contrasting and entropy as a function of age. While there is evidence to support this, the correlation of the change in entropy when images are auto-contrasted as a function of age was not significant ($p = 0.08$). This suggests that the sample size needs to be increased to determine whether this correlation exists. Using the original method without auto-contrasted CSLO images, MMR max entropy images showed a significant increase in image quality with age when compared to the best original image at the LC depth but not at the RNFL depth. When compared to the image formed using linearly polarized light, the fit did not show a significant linear relationship with age at the LC or RNFL depths. For DOP_M and S_0 , when compared to best original CSLO images, there was no significant relationship between increased image quality and age at the LC depth but a significant relationship was found at the RNFL depth. Again, an increased sample size might make the non-significant fits significant.

The comparison of DOP_M and $DOP * S_0$ produced interesting results, DOP_M yielded a slightly higher entropy value while $DOP * S_0$ yielded a slightly higher SNR value. The crucial difference between the two images is the scale factor S_0^{Max} used in the DOP_M equation. Since this scale factor lowered SNR but raised entropy, it would be worthwhile in future work to adjust this scale factor to see how it affects both image quality metrics.

Although the data implies the dependence with age may no longer exist for comparisons with auto-contrasted images, it may still be present with enough participants. Additionally, both MMR and SVR polarimetry methods have been shown to be useful tools for image quality improvement, particularly when quantified by entropy. MMR in particular always produces positive results and there is potential to gain even more improvement through maximizing the dynamic range of pixel values during acquisition of images. S_0 still showed improvement for some participants as did DOP_M for entropy but effects need to be assessed on an image set by image set basis as a percent increase in quantified image quality is not always observed.

Chapter 5 - Polarimetric Imaging of a Malaria Infected In Vitro Retina

5.1 Overview

Mueller matrix polarimetry was applied to imaging of malaria infected retinal vessels to determine the retardance image of malaria infected retinal blood vessel imaged through a confocal scanning laser microscope (CSLM) in an attempt to visualize hemozoin (a deposit of the malaria parasite) within the vessel. Image quality enhancement techniques were applied to the blood vessel and image quality improvement was quantified. Noise due to system vibration and polarimetric effects of the imaging system affected the images adversely but the retardance image still showed hemozoin qualitatively. Image quality enhancement techniques showed average increases of metric value for both MMR and SVR and better visualization of the blood vessel can be seen.

This data was previously presented by Dr. Melanie Campbell [Campbell, 2007]. I worked with Paul Constantinou and Savvas Damaskinos of BPI to custom fit polarizing optics in their CSLM and operated the imaging system. I aligned and toggled the polarizers within the MACROscope. I operated custom software written by BPI to choose appropriate regions of interest, laser frequency, and pinhole size along with Dr. Melanie Campbell during imaging sessions. I also registered, processed, and analysed all data acquired from the system. Mueller matrix and retardance calculation software used in this work was written by Dr. Juan Bueno. Samples were provided by Prof Valerie White.

5.2 Introduction

Malaria is a disease which has affected humanity throughout its history. Mal-aria which in Italian means “bad air” evolved long before humans as malaria parasites as old as 30 million years have been found in fossilized mosquitoes discovered in amber deposits [Poinar, 2005]. Preventative measures through research, medicine and physical barriers have been investigated for centuries. Currently used anti-malaria drugs are losing their effect due to the very quick life cycle and therefore rapid evolution of the parasite leading to drug resistance.

Malaria carrying mosquitoes have recently been eliminated from North America and Europe at high environmental cost by use of DDT and the draining of wetland areas. However, poorer

countries still suffer immensely from the effects of malaria, particularly sub-Saharan Africa where 90 percent of all malaria deaths occur. Malaria infects approximately 500 million people and kills about 1 million of those people every year, mostly young children [Finkel, 2007]. Due to lack of funds, most sub-Saharan Africans are unable to afford anti-malarial drugs. Worse still, people infected with malaria cannot work, further reducing the ability of the people to afford treatment, creating a vicious cycle for poverty stricken nations.

There has been growing resurgence of malaria within North America due to high volumes of travel and the mounting resistance to anti-malaria drugs [Kain, 1998]. Canada in particular has seen a steady increase in the number of reported malaria cases and this is thought to be underestimated because of many cases going unreported or misdiagnosed. With the number of cases rising, there is a growing need for development of new diagnosis techniques for malaria, even within safe regions like Canada and the United States.

Polarimetry has been shown to have potential for malaria parasite detection. Lawrence et al showed birefringence demonstrated in hemozoin (a by-product of the consumption of hemoglobin by the parasite) to be useful as a diagnostic tool for detection of malaria [Lawrence, 1986]. Romagosa used polarimetric techniques to increase the sensitivity of malaria detection from just over 50% to 98.1% in placenta samples [Romagosa, 2004]. Beare et al showed the potential for fundus photography to diagnose comatose children in Africa for severe malaria cases [Beare, 2006]. In this chapter, I will demonstrate a polarization technique with great potential for severe malaria diagnosis that could hopefully eliminate the uncertainty as to whether malaria has become cerebral. A polarimetric MACROscope is used to measure a high resolution two-dimensional Mueller matrix of a retinal sample known to have been contaminated with cerebral malaria parasites. Before delving into the methods, it is important to understand the life cycle of malaria and its relationship with the human body.

5.3 The Malaria Life Cycle

Malaria has a complicated life cycle (figure 5.1). A female mosquito bites a human host injecting sporozoites into the blood stream which make their way to the liver. In the liver, the parasite infects and grows schizonts containing many merozoites, inside liver cells. The schizonts explode and release merozoites into the blood stream which in turn infect red blood

cells. Once infected, red blood cells are called trophozoites. It is at this stage that hemozoin becomes visible as the parasite consumes hemoglobin [Weatherall, 2002]. This cycle repeats with exponential growth as merozoites infect more red blood cells and eventually burst out of the red blood cells to continue the cycle. In the blood infection stage, male and female gametocytes are produced which are transferred to an uninfected mosquito when it bites the human host. They reproduce in the mosquito breeding sporozoites which are passed to a new human host from the mosquito's salivary gland [Weatherall, 2002].

There are actually four types of malaria varying in seriousness; *plasmodium vivax*, *plasmodium malariae*, *plasmodium ovale*, and *plasmodium falciparum*. *Plasmodium falciparum* is well known to be the deadliest form of the parasite with most infection and deaths caused by *P. falciparum* with the other forms rarely resulting in serious complications or death [Weatherall, 2002]. Reliable early diagnosis of the disease is extremely important so it can be treated properly with anti-malarial drugs.

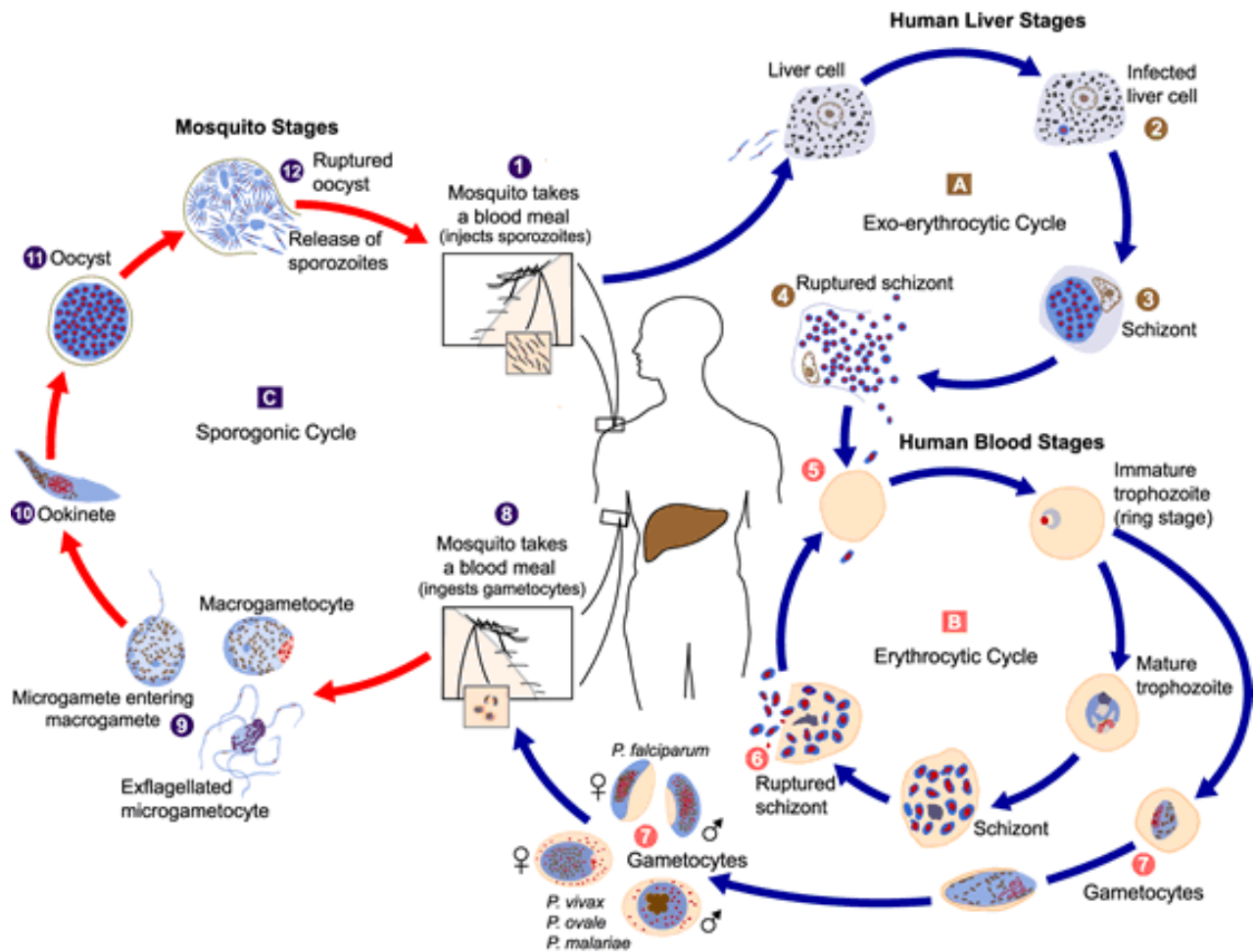


Figure 5.1: Life cycle of malaria (image was released into the public domain by Center for Disease Control - <http://phil.cdc.gov/phil/details.asp>).

5.4 Diagnosis

The gold standard for detection is still a simple blood smear slide viewed with an oil immersion white light microscope. Thin blood smears are used to assess which type of plasmodium is responsible for the infection. This is important because as mentioned earlier, *P. falciparum* is the cause of almost all deaths related to malaria. Thick blood smears are used in an attempt to quantify the degree of infection by revealing an estimate of parasite density although there have been some questions raised as to whether this method is accurate or if it actually underestimates density [Bejon, 2006]. Thick smears are not used for identification of the parasite

because the drying process of the blood can cause distortions in the morphology leading to misdiagnosis.

Before reaching the point of a blood smear however, there must first be clinical suspicion of infection. According to a Canadian study done by Kain et al, 59% of all reported malaria cases were initially misdiagnosed by a physician. Sixteen percent of all cases needed to see 3 or more doctors before a time consuming blood smear from the patient was implemented for a correct diagnosis [Kain, 1998]. This clearly demonstrates the need for new and more efficient diagnosis techniques not just within malaria zones, but around the globe.

5.5 Methods

5.5.1 The MACROscope

Polarization imaging was used to image entire slides of retinas flat mounted on a slide in a CSLM MACROscope at Biomedical Photometrics, Inc. (BPI) in Waterloo, Ontario in an attempt to visualize hemozoin in the sample tissue using polarimetric imaging with the future potential of visualizing hemozoin *in vivo* using a retinal imaging system. The MACROscope itself is fundamentally a confocal scanning laser microscope (CSLM) [Dixon, 2006]. The MACROscope was chosen for this work because it has the ability to image entire slides at high resolution (0.5 μ /pixel), up to 127 mm by 178 mm across. Normally, to retrieve images on such a large scale, many images are taken of various locations and they are stitched together using image registration when processing the images after acquisition. Single image acquisition is particularly beneficial to this work because being able to image the entire slide removes the need to search for and locate the best area for imaging, allowing for this to be done in the processing stage (figure 5.2).

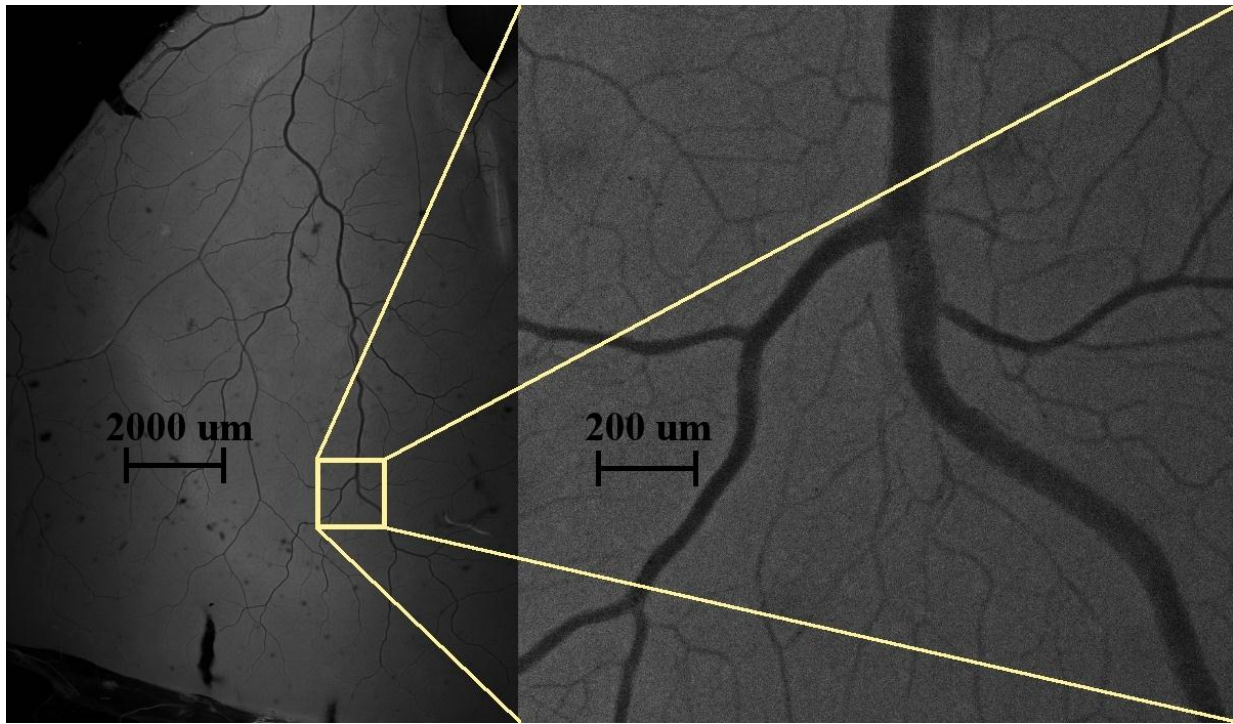


Figure 5.2: Image of a malaria infected retina taken on a Macroscope (left). Small ROI taken after acquisition (right).

The MACROscope also utilizes a number of scanning modes allowing for fluorescence, reflection, transmission, differential phase contrast, and hyperspectral imaging. The unique wide field imaging ability of the MACROscope has many potential biomedical and commercial applications. It has been used to image live and fixed biological tissue samples to examine cancerous cells, blood vessels, and tissue hypoxia (oxygen deprivation) [Wilson, 2005]. Dixon et al showed its ability to acquire high resolution fingerprint images from a variety of materials [Dixon, 1995]. The devices are used in the imaging of lithologies in lake and ocean sediment core samples. As well, high-resolution imaging for microfossil detection has been explored [Dixon, 2006]. The incorporation of polarimetry into microscopic imaging has been shown to increase the contrast of images, improving quality [Oldenbourg, 1995].

Images could be taken with one of two detectors, one that samples the light reflecting back from the sample and another that detects light transmitting through the sample. Due to physical limits within the system, Mueller matrix polarimetry could only be performed in reflection mode. The MACROscope was modified to fit a generator and analyzer unit into the pathway of a beam

incident on the retinal sample for reflected polarimetric imaging. Light from a 638 nm laser passes through a polarization state generator unit incorporated into the pathway collimated beam. The light then reflects from a galvanometer scanning mirror and is focused onto the sample through a 50 mm telecentric lens. The perpendicular scan is accomplished by movement of the stage holding the sample. After reflecting off of the sample and being descanned, the light passes through the polarization state analyzer unit and is collected by a photodetector.

5.5.2 Polarimetry

Using this setup, 16 images corresponding to independent combinations of generator and analyzer settings were acquired, registered and the Mueller matrix was calculated. All 16 images were taken at the same location on the same retina sample, positive for malaria. From the Mueller matrix, the retardation of the sample was calculated at each registered pixel to examine the potential birefringent properties of the sample.

Due to the massive size of the images obtained from the MACROscope, a smaller preferred section of the sample was chosen. A 1024x1024 pixel (0.25 mm²) section of the original sample was cropped and registered.

In addition, using the methods outlined in section 4.1.3, the top row of the Mueller matrix of the sample was used to find the output intensity image (S_0^{OUT}) for input polarization states covering the Poincare sphere, using the equation:

$$S_0^{OUT} = [m_{00} \quad m_{01} \quad m_{02} \quad m_{03}] \cdot \begin{bmatrix} 1 \\ S_0 \cos 2\chi \cos 2\psi \\ \cos 2\chi \sin 2\psi \\ \sin 2\chi \end{bmatrix} \quad (5.1)$$

Recall that the variables χ and ϕ are swept through 5° steps, sweeping through approximately all polarization states. The images yielding the highest values of entropy and SNR are labeled as the best images and then quantitatively compared to original CSLO images using image quality metrics SNR and entropy.

A subset of generator and analyzer positions also allowed for the calculation of the modified DOP_M and S_0 images with the generator unit set at -45° (circularly polarized light) and the

quarter-wave plate of the analyzer unit cycled through the four positions -45° , 0° , 30° , and 60° producing the output Stokes vector and allowing the DOP_M image calculation (see section 4.3.4).

Both MMR and SVR images were compared to the best auto-contrasted image produced by the MACROscope.

5.5.3 Registration

To ensure the images are registered by rotation and translation, the best Canny filter from Chapter 3 was used, each image was rotated through 0.5° in both directions by steps of 0.1° and through 15 pixels in all directions by steps of 1 pixel. This would move through an area of 31 by 31 pixels. For each step, the correlation function was calculated and the position yielding the maximum cross-correlation value was taken as indicating that the two images were registered.

From the registered images, the Mueller matrix of the sample was calculated at each pixel. The spatially resolved retardance was calculated for each pixel using the elements of the Mueller matrix. When inspected, Mueller matrix elements can be used to infer some polarization properties as well as being used to explicitly calculate the sample's polarization properties. A crossed polarization image was also acquired to take advantage of the birefringent properties of the hemozoin left behind by the malaria parasite.

5.6 Results

Displayed below (figure 5.3) are 16 0.25 mm^2 images of the same vessel cropped from the 16 different polarization state images.

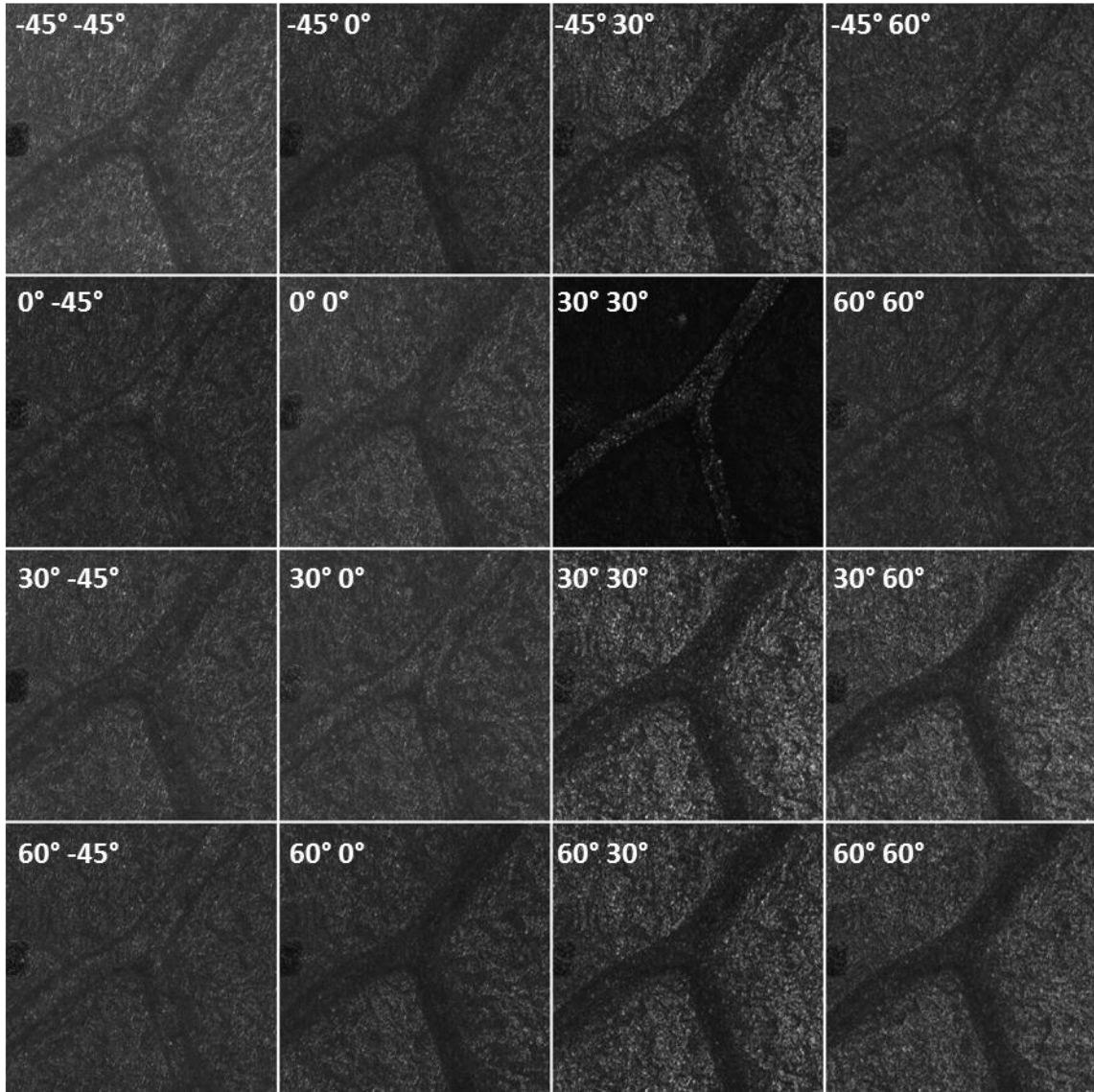


Figure 5.3: Small section (0.25 mm^2) of vessel from the retinal sample taken at 1μ resolution. In the top left corner of each image is the generator and analyzer setting, respectively.

Note how the reflection of light from the sample varies due to the configurations of the generator and analyzer units. In particular, notice how the signal level of the vessel and tissue vary relative to each other from image to image.

After registration, the Mueller matrix of the sample was calculated (figure 5.4). Due to physical restrictions in the MACROscope system, it was not possible to quantify the polarization within the imaging system itself. The assessment of the machine characteristics (Bueno, 2000)

required transmission mode but the spacing between the detector and the sample left no space for the analyzer unit. This means that the resulting Mueller matrix represents the polarization properties of the sample plus the MACROscope.

5.6.1 Mueller Matrix

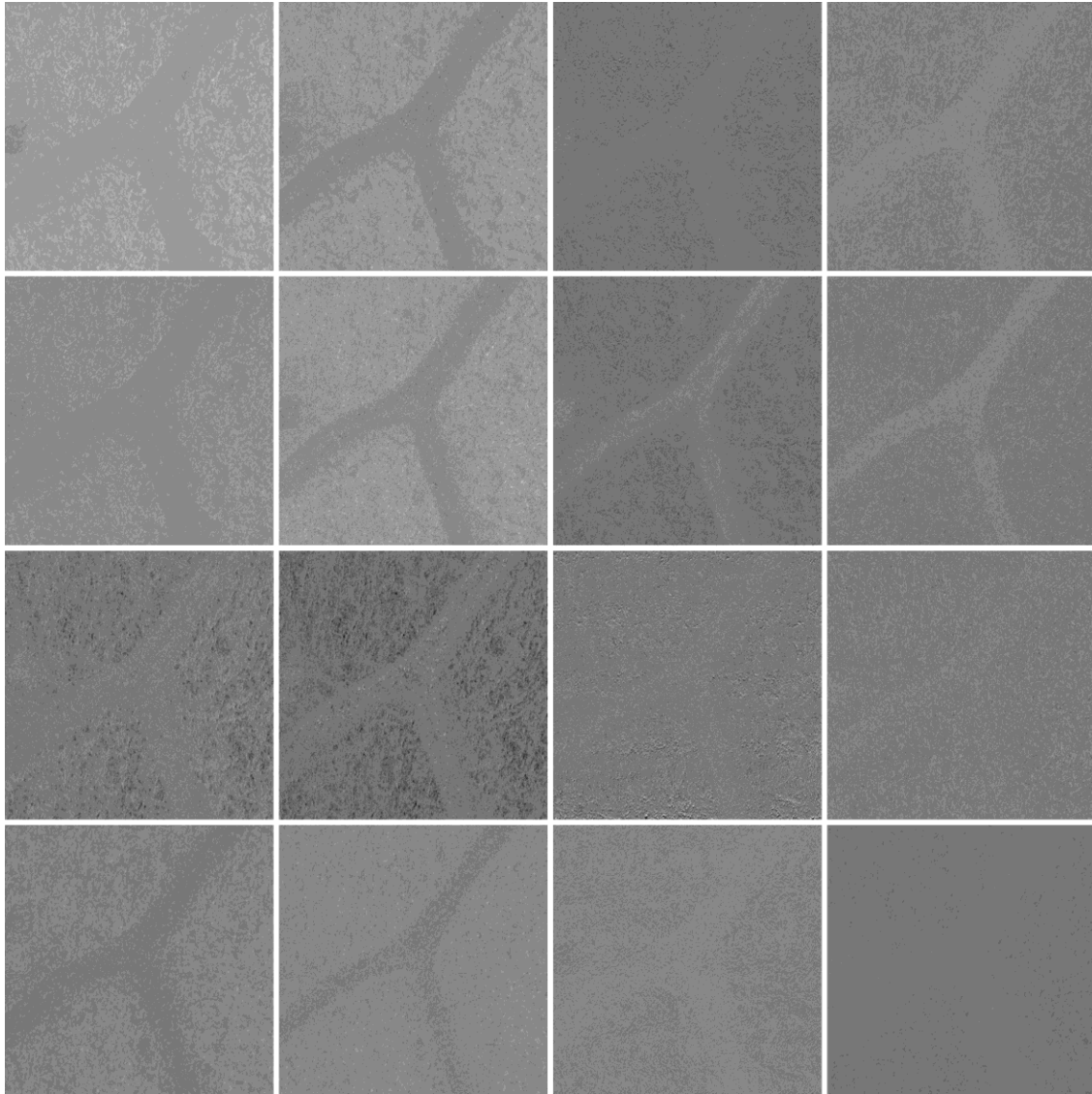


Figure 5.4: Mueller matrix maps of a small section (0.25 mm^2) of vessel from the retinal sample taken at 1μ resolution.

From the Mueller matrix, the retardance map of the sample qualitatively shows the birefringent properties of the hemozoin within the vessel. The noise in the image appears to come from vibrational noise. Quantitative values cannot be given since the values are affected by the polarization properties of the imaging system and the noise. However, the retardance map

still demonstrates the large relative difference between the retinal tissue and the hemozoin displayed assumed to be the dark spots found within the blood vessel (figure 5.5).



Figure 5.5: Total retardance map calculated from the Mueller matrix.

5.6.2 Crossed Polarizer Results

Under the crossed polarization setup, we were able to image birefringent hemozoin on a dark background (figure 5.6).

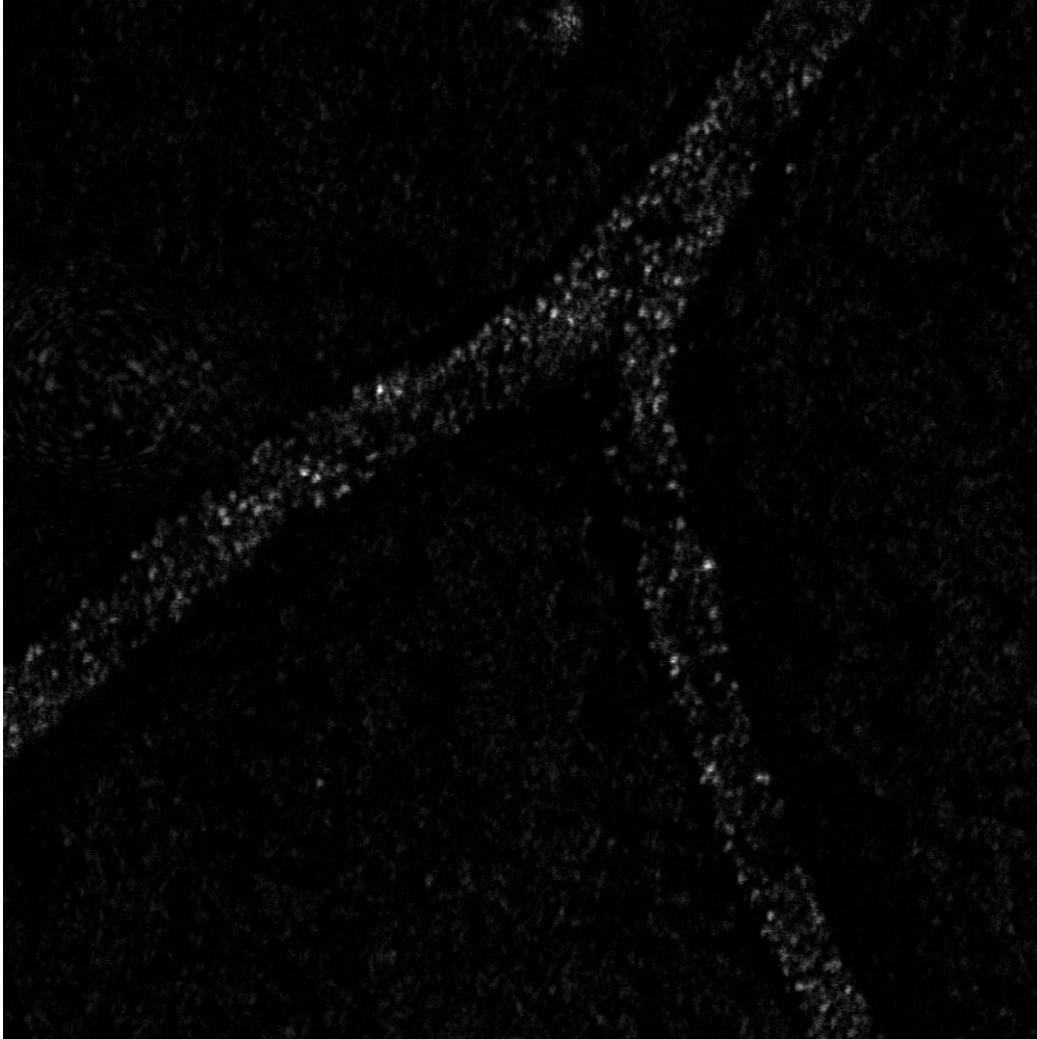


Figure 5.6: Malaria retinal sample in a near crossed polarizer setup.

The image shows bright spots which appear to be hemozoin deposited from the remains of red blood cells (7.5 μm) [Marieb, 2001] with hemozoin lighting up due to its linear birefringence.

5.6.3 Image Quality Improvement

Mueller matrix reconstruction provided improvements in terms of SNR and entropy metrics over original auto-contrasted images.

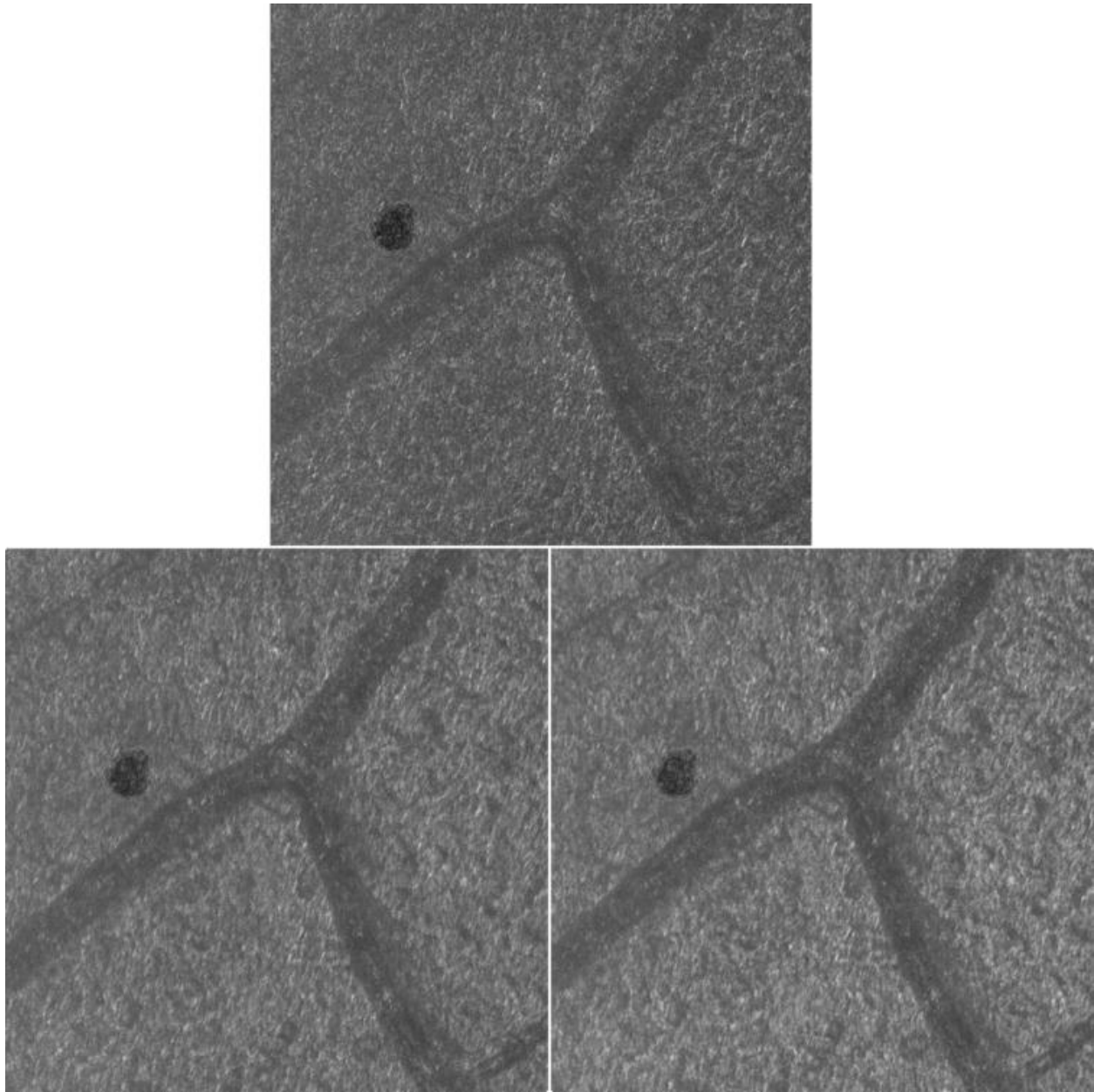


Figure 5.7: Original best auto-contrasted MACROscope image (top), MMR SNR image (bottom left), and MMR entropy image (bottom right).

The MMR image with maximum SNR yielded a percent increase of SNR of 15.3% when compared to the best MACROscope image and the MMR image with maximum entropy showed a percent increase of 19.7% when compared to the best MACROscope image.

Stokes vector reconstruction showed some quantitative improvement over the best auto-contrasted original image.

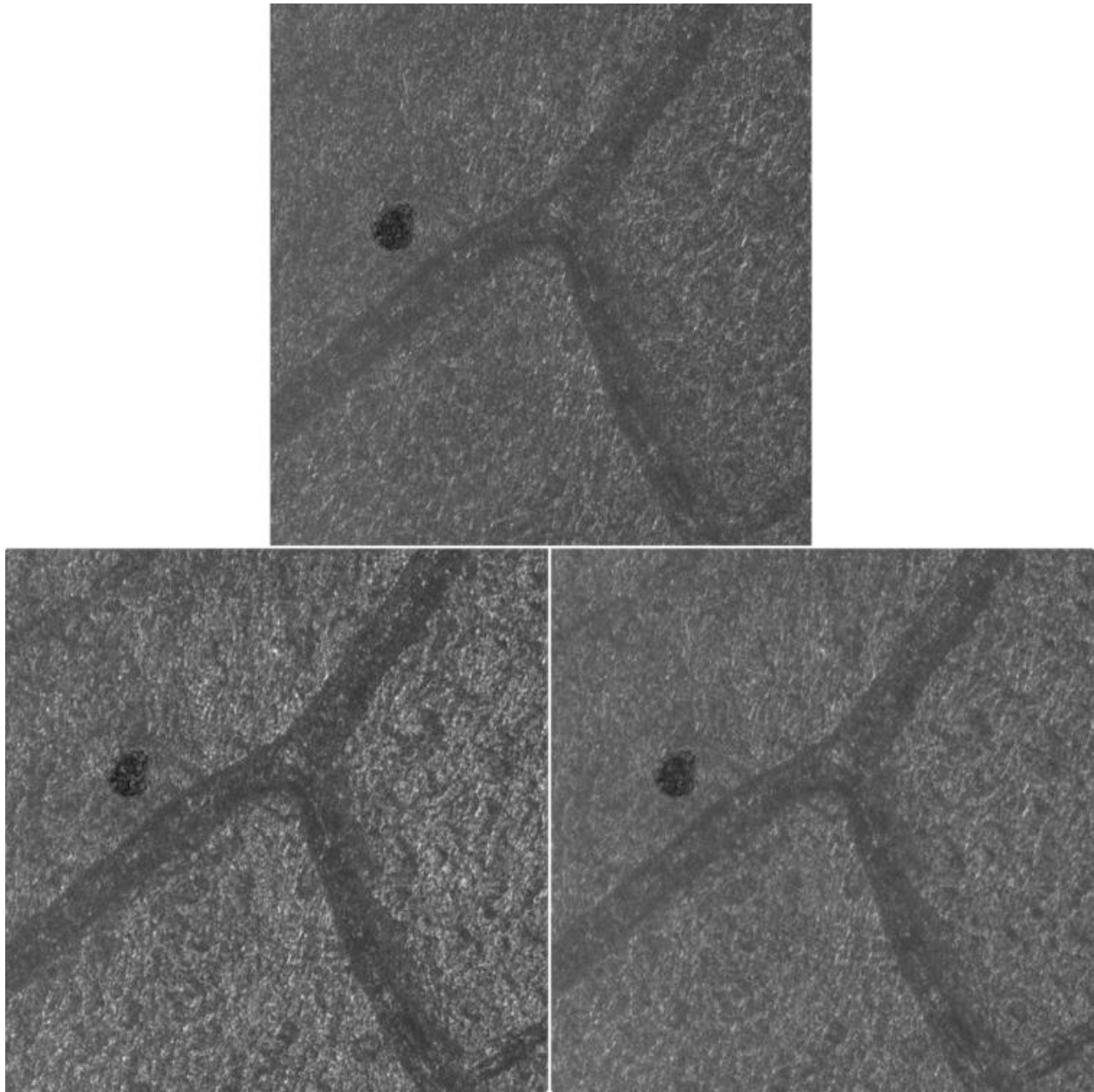


Figure 5.8: Original auto-contrasted MACROscope image (top), SVR DOP_M image (bottom left), and SVR S_0 image (bottom right).

In terms of SNR, the S_0 image yielded a percent change of 9.44% while the DOP_M image produced negative results with a percent change of -24.3%. In terms of entropy, both S_0 and the DOP_M gave positive results. The S_0 image had a percent change of 9.49% and the DOP_M image gave a percent change of 8.62%.

5.7 Discussion

Using an inverted image and thresholding techniques, the similarities between the retardance map and cross polarizer image can be clearly seen.

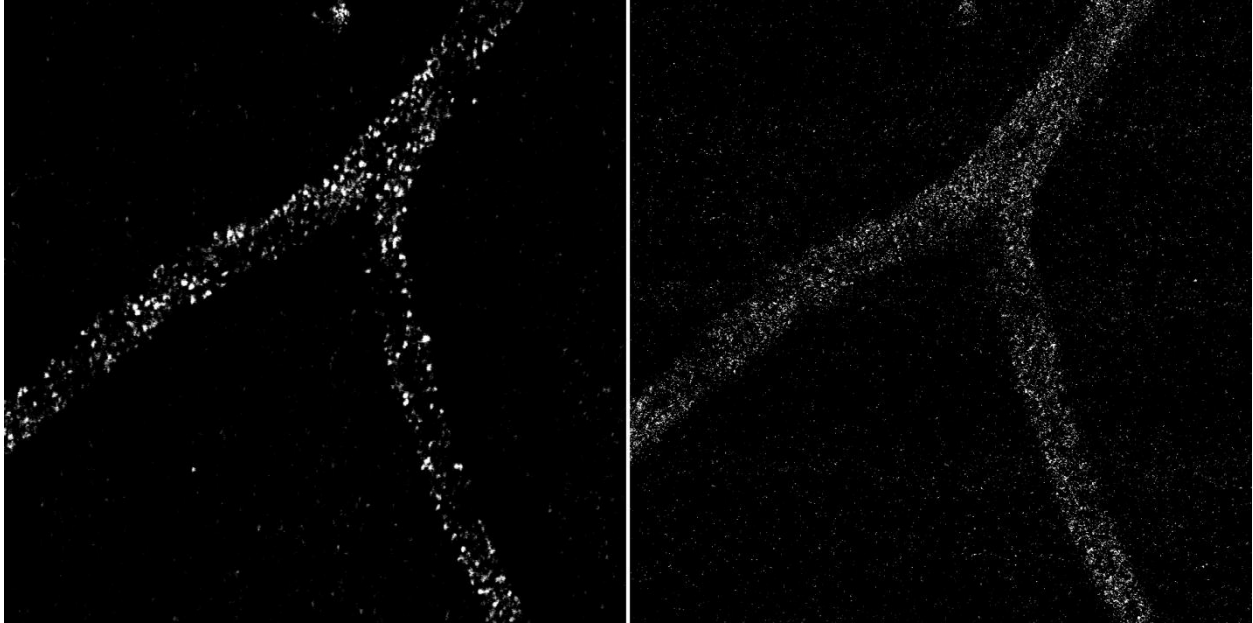


Figure 5.9: Thresholded crossed polarization map (left) compared to thresholded retardance map (right).

The intense regions of birefringence in the retardance map match that of the cross polarization map. Particularly, notice the intensity at the junction of the blood vessels and similar gaps in intensity directly below and above the vessel junction.

The most striking difference between the two maps is the spot size is much greater in the cross polarization image versus the retardance image. Spot size is expected to be about the size of a red blood cell because hemozoin is a by-product of haemoglobin ingestion by the parasite, which collects in clusters inside red blood cells (figure 5.10).

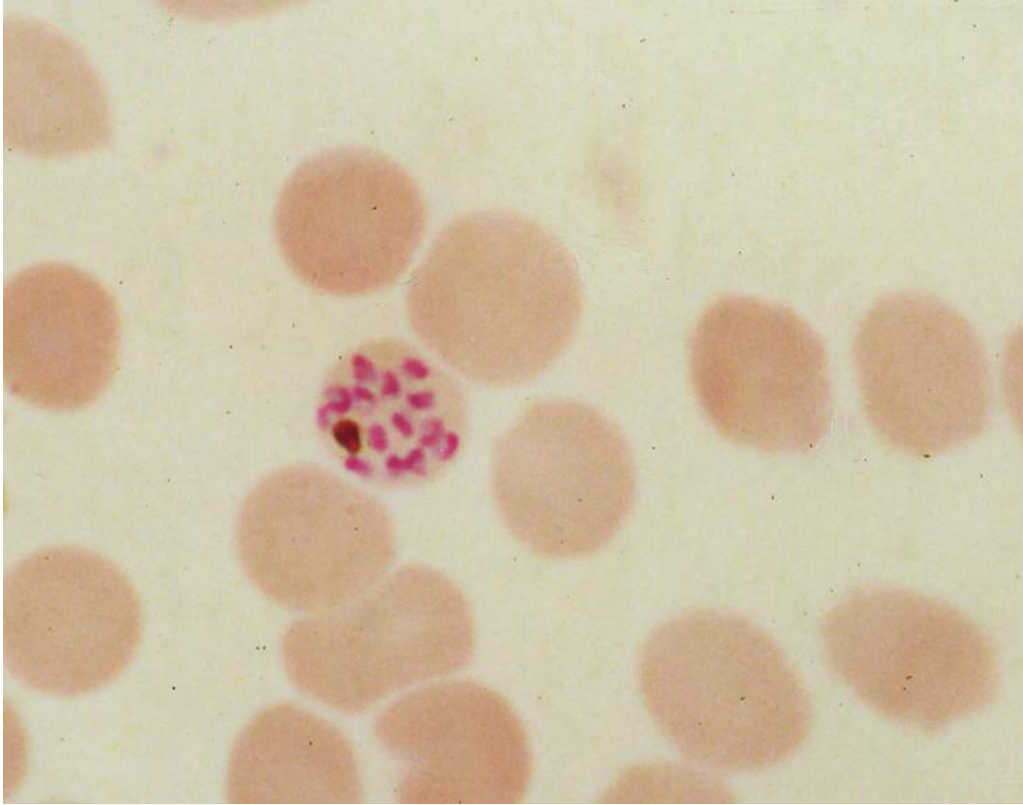


Figure 5.10: Hemozoin deposits left behind in a malaria infected red blood cell (public domain wikipedia image - http://en.wikipedia.org/wiki/File:P.falciparum_schizont.jpg)

Red blood cells infected by the parasite are also known to adhere to the vessel wall (Weatherall, 2002) which appears to be the case in our images, particularly along the bottom section of the large vessel (figure 5.9). The crossed polarization map shows expected spot sizes of $6-8\ \mu$, the width of a red blood cell [Marieb, 2001] while the retardance map shows smaller spots lighting up inside the blood vessel. This difference in spot size can be attributed to noise introduced by the imaging process because of small vibrations caused by the MACROscope itself. This introduced random aberrations into each image used to calculate the Mueller matrix, creating a noise like effect in the end result. Fortunately, the aberrations were small enough that evidence of birefringence in the retardance map was still visible.

In terms of image quality improvement, even with severe noise problems, both techniques showed overall improvement according to quantitative measures using SNR and entropy (figure 5.11). Most note-worthy was a clear increase in the visibility of blood vessel relative to the background tissue, consistent with initial reports on the MM technique.

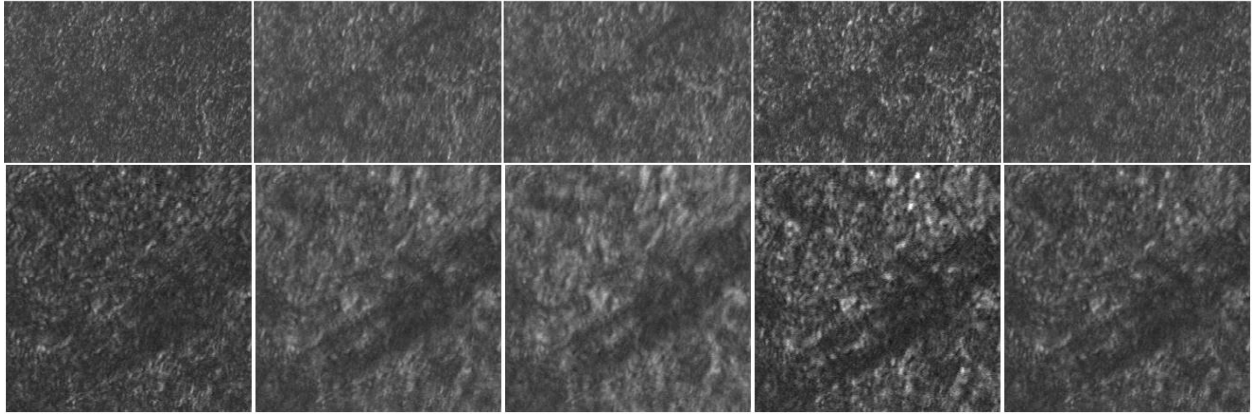


Figure 5.11: Improvement in blood vessel visualization for smaller (above) and larger (below) vessels. From left to right – Best auto-contrasted MACROscope image, MMR best SNR image, MMR best entropy image, SVR best DOP_M image, and best SVR S_0 image.

In terms of entropy, the MMR max entropy image yielded a percent increase of 19.7%, SVR DOP_M image saw a 8.62% percent increase, and the SVR S_0 image showed a 9.49% increase in image quality. For SNR, the MMR max SNR image increased image quality by 15.3%, the SVR DOP_M image showed a drop in image quality of 24.3%, and the SVR S_0 image yielded a percent increase of 9.44%.

5.8 Conclusion

We have demonstrated the ability to image birefringent hemozoin using a polarimetric MACROscope under cross polarization and by calculating the retardance map using the Mueller matrix of the retinal sample using polarization generator and analyser units. Both a simple crossed polarized image and Mueller matrix generated retardance map show potential for *in vivo* imaging of hemozoin in the living human retina. Although different methods were used, the bright areas indicating birefringence in the retardance image correspond closely with the areas seen to be birefringent in the cross polarization image, giving a strongly correlated result. Differences in size and shape between the bright spots in the crossed-polarized and retardance image are most likely due to significant vibrational noise in the system. Since the retardance map is found from the Mueller matrix which is calculated by 16 registered MACROscope images, the random vibrational noise found in all 16 images would misalign pixels randomly. Since

registration only globally rotates and translates the images, registration could not compensate for the vibrational noise and any misaligned pixels caused by it could not be corrected.

Image quality improvement using polarimetry also gave positive results with both quantitative improvements via image quality metrics SNR and entropy as well as qualitative improvements in visualization of blood vessels in the retinal sample. The methods also showed their ability to work in “harsh” conditions, improving metric values and visualization in the presence of strong vibrational noise. These visualization improvements could aid in diagnosis of retinopathy which is important for the study of malarial infection in both children and adults.

For future work on this project, it is important to perform experiments with this type of imaging device with the vibration tightly controlled using an anti-vibration table. This would produce a higher definition Mueller matrix which in turn affects the retardance map of the sample. A system must be chosen where the polarization properties of the system itself can be properly measured so that quantitative values of the retardance map may be obtained.

Disregarding vibration issues, both imaging methods have their strengths. The cross polarization method only requires two linear polarizers where the Mueller matrix method needs two linear polarizers and two quarter wave plates. Secondly, only 1 image is required under cross polarization as opposed to the 16 needed to compute the Mueller matrix. This results in reduced setup, acquisition and processing time while simultaneously reducing the cost of optical components which will be important for the technology to reach poorer regions. A cross polarizer setup eliminates the chance for error in the alignment portion of analysis due to local variations in brightness and contrast under polarized light imaging. Alignment is also a time consuming operation for a computer to perform, eliminating this step also greatly reduces analysis time, particularly if the analysis was to be performed on the entire MACROscope image. On the other hand, the Mueller matrix is much more versatile. One data set can perform many possible tasks as demonstrated by using the same set to isolate hemozoin as well as improve sample image quality.

Chapter 6 - Conclusions

In this thesis, I have shown the versatility of confocal scanning laser imaging systems (CSLO and MACROscope) combined with Mueller matrix polarimetry. Improvements were made to retinal image acquisition by the Waterloo CSLO and to image processing. Stepper motors were added that drove the rotation of the quarter-wave plates in the generator and analyzer units and were run from a computer. This reduced acquisition time significantly by 79% and suggested that registration times might decrease. Additional participants would strengthen the power of the tests for decreases in registration times.

In the processing stage, Fourier transform edge detection filters were incorporated into the registration process. This increased registration success from 70.7% to 93.3% for optic nerve head images and from 20% to 93.3% for fovea images. These techniques were also used on images acquired to reassess Mueller matrix and Stokes vector reconstruction methods increasing the number of successful registrations from 81.8% to 92.3%. Even unsuccessful registrations were only misaligned slightly. At least 3 of the 5 judgment points were always exactly aligned and the misaligned points were due to image warping, not an incorrect rotation or translation. If image warp correction within a frame was introduced, this could make registration success rate even better [Vogel, 2006], [Arathorn, 2007].

Further improvements could be made to illumination correction since the results of methods attempted to address this were mixed. An assessment of the complex noise introduced from the CLSO may be the key to a useful illumination correction and further noise reduction. While illumination correction was a key component in producing the best filter for the Canny filter combination, it failed to be useful in combination with Sobel or high pass filters.

Overall, the success rate of the registration process was vastly improved, but the computing time needed and warping remain as two major problems. Future work should focus on improvements in speed and to the registration process through warp correction.

6.2 Mueller Matrix Polarimetry

Once acquired, polarimetric images were used to perform Mueller matrix reconstruction on CSLO images. For Mueller matrix reconstruction (MMR) with original CSLO images, the mean

significant percent increase in entropy value was 158% and in SNR value was 4%. The improvement was even larger when compared to linearly polarized CSLO images. Auto-contrasted CSLO images were also input into the method and maximum entropy and maximum SNR images were compared to the best auto-contrasted CSLO image. This showed a significant decreased percent improvement for entropy but a significant increase in percent improvement for SNR. The mean percent increase in entropy value was 11% and in SNR value was 5%. When inputting auto-contrasted images, the mean absolute value of entropy and SNR of the MMR maximum entropy and maximum SNR images were increased by 29868 to 31093 and by 1 to 2, respectively. This indicates that inputting auto-contrasted images into the MMR algorithm actually improves the image quality of its reconstructed images. For either metric used to quantify image quality improvements, no increase in image quality as a function age was found when auto-contrasted images were input into MMR. This suggests that the dependence seen with age for the entropy metric was most likely due to auto-contrasting of the output image and not the MMR algorithm. However, a larger sample size could potentially make this correlation significant. The power of the regression was not high. In order to reach a power of 0.8, the sample size is estimated at 24 participants.

For Stokes vector reconstruction, image quality quantified by entropy showed significant improvement over the original images except for the entropy of the DOP_M images of the RNFL. SNR did not improve for either S_0 or DOP_M images. For the SVR algorithm quantified by entropy and SNR, the DOP_M and S_0 images failed to show a significant percent increase in image quality when compared to the best auto-contrasted CSLO images. Increased sample size could change these insignificant results which had low power.

Understanding the source of image quality improvements in the polarimetry methodology, is important. While the polarimetry methods still achieved improvement in image quality in terms of entropy when the final images were compared to auto-contrasted images, much of the improvement appeared to be due to the inclusion of auto-contrasting within each algorithm. Once compared to auto-contrasted images, improvement rates dropped substantially and improvement correlations with age disappeared. The correlation with age found when compared to non-auto-contrasted images cannot be attributed to the polarization enhancement method. The dependence of enhancement on the degree to which an image could be auto-contrasted is demonstrated by the

relationship between the percent increase in entropy and percent increase in pixel value and the change in entropy versus the change in pixel value when an image is auto-contrasted, coupled with the lower maximum pixel value found in original CSLO images (not auto-contrasted) as age increased. This in turn supports the role of auto-contrasting in the age dependence of image quality enhancement. Decreased optical quality and darker images resulting from poorer optical quality likely due to increased scattered light [Kuroda, 2002], in older participants, confounded with the safety limits on the amount of light that may be safely input into the eye (which are reached with older participants), are the most likely candidates for the age dependence seen using entropy as a metric for MMR and SVR image quality enhancement which includes auto-contrasting. It should be noted that our lab uses levels 10 times below recommend ANSI safety standards to ensure participant comfort and safety.

Although the image quality metric, SNR suggested poorer performance of the polarization methods, their performance in terms of entropy proves their usefulness for image quality improvement as entropy was found to be a more useful metric for the appearance of retinal images than SNR [Hunter, 2007].

When applied to the malaria images, a slightly more positive but similar outcome was found. MMR best entropy and best SNR images were found to have a 19% and 15% increase in metric performance compared to the best original CSLO images. SVR enhancement results were mixed. The S_0 image yielded a 9% improvement for both entropy and SNR. The DOP_M image gave an 8% percent increase in metric value for entropy but a 24% decrease in metric value for SNR. Qualitatively, the image enhancement techniques did very well in terms of better visualization of the blood vessels themselves in the images of malaria infected retina. If vibrational noise were eliminated, the results would only be sharper as the vibration blurred the images slightly because it affected registration.

While benefits may have been overstated in terms of percent increase in metric value, Mueller matrix reconstruction and Stokes vector reconstruction should still be considered useful tools for diagnostic retinal image quality improvement because individual participants still showed improvements.

The Mueller matrix itself was calculated on a section of retina infected with malaria and crossed polarization images were also acquired. The crossed polarizer image was very successful in localizing hemozoin within the infected blood vessels. The Mueller matrix reconstructed image could only be interpreted qualitatively, because unfortunately, the vibration in the system over 16 images combined with indefinable polarization within the MACROscope imaging system caused too much error to determine exact values of the polarization properties. However, qualitatively, the hemozoin could still be seen in the retardance map of the section of blood vessel. In future work, a Mueller matrix reconstruction approach may make it possible to quantify the load of hemozoin within a sample since an exact value of retardance can be calculated when using a system where the polarization of the system can be quantified and noise effects are not so devastating to the quality of the image. This would be similar to techniques used to measure the thickness of Henle's fiber layer in the diagnosis of early glaucoma where the phase retardance of the polarized wave indicates thickness [Burke, 2006]. The amount of phase retardance present in the measurement of hemozoin could potentially provide insight into the severity of infection.

In conclusion, the Mueller matrix is a powerful tool and when some or all spatially resolved elements are acquired, opens many possible avenues in the study of the retina. It has demonstrated applications in detecting and assessing retinopathy through image quality improvement, assessment of polarization properties, and localization of pathologically significant features. There is no doubt that Mueller matrix polarimetry will continue to push forward retinal diagnostic techniques and the general understanding of many retinal pathologies.

References

Ambirajan A, Look, DC. Optimum Angles for a Polarimeter: Part I. Optical Engineering Vol. 34, No. 6, pg. 1651-1655 (1995).

American National Standards Institute (2000) American National Standard for Safe use of Laser. Z136.1-2000, American National Standards Institute; Laser Institute of America, Orlando, FL.

Arathorn DW, Yang Q, Vogel CR, Zhang Y, Tiruveedhula P, and Austin Roorda. Retinally stabilized cone-targeted stimulus delivery, Optics Express, Vol. 15, Issue 21, pp. 13731-13744 (2007).

Beare NAV, Harding SP, Taylor TE, Lewallen S, Molyneux ME. Perfusion Abnormalities in Children Cerebral Malaria and Malarial Retinopathy. J. Infect. Dis. Vol. 199, No. 2, pg. 23-271 (2009).

Beare NAV, Taylor TE, Harding SP, Lewallen S, Molyneux ME. Malarial Retinopathy: A Newly Established Diagnostic Sign in Severe Malaria. Am. J. Trop. Med. Hyg. Vol. 75, No. 5, pg. 790-797 (2006).

Beare NAV, Southern C, Chalira C, Taylor TE, Molyneux ME, Harding SP. Prognostic Significance and Course of Retinopathy in Children With Severe Malaria. Arch. Ophthalmol. Vol. 122, pg. 1141-1147 (2004).

Bejon P, Andrews L, Hunt-Cooke A, Sanderson F, Gilbert SC, Hill AVS. Thick Blood Film Examination for Plasmodium Falciparum Malaria Has Reduced Sensitivity and Underestimates Parasite Density. Malaria Journal, 5:104 (2006).

Blanchet G, Charbit M. Digital Signal and Image Processing using MATLAB. ISTE Ltd. Ch. 7, pg. 247-272 (2006).

Bour LF. Polarized light and the eye. In: W. Neil Charman (editor). Visual optics and instrumentation. Hampshire and London. The Macmillan Press Ltd, pg. 310-325 (1991).

Bueno JM. Measurement of parameters of polarization in the living human eye using imaging polarimetry. Vision Res. **40**, 3791-3799 (2000).

Bueno JM and Artal P, "Double-pass imaging polarimetry in the human eye," Opt. Lett. 24, 64-66 (1999).

Bueno JM, Cookson CJ, Hunter JJ, Kisilak ML, Campbell MCW. Depolarization Properties of the Optic Nerve Head: the Effect of Age. *Ophthal. Physiol. Opt.* Vol. 29, pg. 247-255 (2009).

Bueno JM, Cookson CJ, Kisilak ML, Campbell MCW. Enhancement of Confocal Microscopy Images using Mueller-matrix Polarimetry. Vol. 235, pg. 84-93 (2009b).

Bueno JM, Cookson CJ, Hunter JJ, Kisilak ML, Campbell MCW. Imaging the Fundus of the Eye through Polarization: Dependence with Age, ARVO; Fort Lauderdale, FL. (2008).

Bueno JM, Hunter JJ, Cookson CJ, Kisilak ML, Campbell MCW. Improved Scanning Laser Fundus Imaging Using Polarimetry. *J. Opt. Soc. Am. A.* Vol. 24, No. 5, pg. 1337-1348 (2007).

Bueno JM, Vohnsen B. Polarimetric High-resolution Confocal Scanning Laser Ophthalmoscope. *Vision Research* Vol. 45, pg. 3526-3534 (2005).

Bueno, JM, Campbell, MCW. Confocal scanning laser ophthalmoscopy improvement by use of Mueller-matrix polarimetry. *Optics Letters* Vol. 27, No. 10, pg. 830-832 (2002).

Bueno JM, Jaronski J. Spatially Resolved Polarization Properties for *in vitro* Corneas. *Ophthal. Physiol. Opt.* Vol. 21, No. 5, pg. 384-392 (2001).

Burke MA, Khanna CJ, Miller A, Venkataraman ST, Hudson C The impact of artificial light scatter on scanning laser tomography. *Optom Vis Sci* Vol. 83, pg. 222-227 (2006).

Burns SA, Elsner AE, Mellem-Kairala MB, Simmons RB. Improved Contrast of Subretinal Structures using Polarization Analysis. *Investigative Ophthalmology & Visual Science* Vol. 44, No. 9, pg. 4061-4068 (2003).

Campbell MCW, Cookson CJ, Bueno JM, Seaman A, Kisilak ML. Confocal Polarimetry Measurements of Tissue Infected with Malaria, in *Frontiers in Optics 2007/Laser Science XXIII/Organic Materials and Devices for Displays and Energy Conversion*, OSA Technical Digest (CD) (Optical Society of America, 2007), paper FThK1.

Castleman KR *Digital image processing*. Prentice Hall, Englewood Cliffs, NJ (1996).

Cense, B, Chen, TC, Park BH, Pierce MC, de Boer JF. *In vivo* birefringence and thickness measurements of the human retinal nerve fiber layer using polarization-sensitive optical coherence tomography. *Journal of Biomedical Optics*, Vol. 9, No. 1, pg. 121-125 (2004).

Cherici C, Kuang X, Poletti N, Rucci M. Precision of Sustained Fixation in Trained and Untrained Observers. *Journal of Vision*, Vol. 12, No. 6, pg. 1-16 (2012).

Collett E. *Polarized Light: Fundamentals and Applications*. Marcel Dekker, Inc. v. 36 (1992).

Dixon AE, Damaskinos S, Beesley KM. Fingerprint Imaging with a Confocal Scanning Laser Microscope. *Journal of Forensic Sciences, JFSCA*, Vol. 40, No. 1, pg. 10-17 (1995).

Dixon AE, Damaskinos S, Tsintzouras G, Rack FR, Ribes AC. Applications of Confocal Microscope-Luminescence Imaging to Sediment Cores. *London Geological Society Special Publications*, vol. 267, pg. 141-150 (2006).

Dondorp AM, Ince C, Charunwatthana P, Hanson J, van Kuijen A, Faiz MA, Rahman MR, Hasan M, Yunus EB, Ghose A, Ruangveerayut R, Limathurotsakul D, Mathura K, White NJ, Day NPJ. Direct *In Vivo* Assessment of Microcirculatory Dysfunction in Severe Falciparum Malaria. *The Journal of Infectious Diseases* Vol. 197, pg. 79-84 (2008).

Finkel M. *Bedlam in the Blood: Malaria*. National Geographic, (2007).

Frosch T, Koncarevic S, Zedler L, Schmitt M, Schenzel K, Becker J, Popp J. *In Situ* Localization and Structural Analysis of the Malaria Pigment Hemozoin. *J. Phys. Chem. B*. Vol. 111, pg. 11047-11056 (2007).

Fujikado T, Kuroda T, Ninomiya S, Maeda N, Tano Y, Oshika T, Hirohara Y, Mihashi T. Age-related Changes in Ocular and Corneal Aberrations. *Am J Ophthalmol* 138, pg. 143-146 (2004).

Goldberg DE, Slater AFG, Cerami A, Henderson GB. Hemoglobin Degradation in the Malaria Parasite *Plasmodium Falciparum*: An Ordered Process in a Unique Organelle. *Proc. Natl. Acad. Sci.* Vol. 87, pg. 2931-2935 (1990).

Grigorescu C, Petkov N, Westenberg MA. Contour and Boundary Detection Improved by Surround Suppression of Texture Edges. *Image and Vision Computing* Vol. 22, No. 8, pg. 609-622 (2004).

Guyot S, Anastasiadou M, Delechelle E, De Martino A. Registration scheme suitable to Mueller matrix imaging for biomedical applications. *Optics Express*, Vol. 15, No. 12 (2007).

Hauge PS, Mueller Matrix Ellipsometry with Imperfect Compensators. *J. Opt. Soc. Am.* **68**, 1519 (1978).

Hanschied T, Egan TJ, Grobusch MP. Haemozoin: From Melatonin Pigment to Drug Target, Diagnostic Tool, and Immune Modulator. *Lancet Infect. Dis.* Vol. 7, pg. 675-685 (2007).

Hecht E. *Optics*. San Francisco, CA, USA. Addison Wesley (2002).

Hidayat AA, Nalbandian RM, Sammons DW, Fleischman JA, Johnson TE. The Diagnostic Histopathologic Features of Ocular Malaria. *Ophthalmology* Vol. 100, No. 8, pg. 1183-1186 (1993).

Hunter JJ. Image Quality in Ocular Development and Fundus Imaging. Ph.D. Thesis. Waterloo University, Canada (2006).

Hunter JJ, Cookson CJ, Kisilak ML, Bueno JM, Campbell MCW. Characterizing Image Quality in a Scanning Laser Ophthalmoscope with Differing Pinholes and Induced Scattered Light. *J. Opt. Soc. Am. A* Vol. 24, No. 5, pg. 1284-1295 (2007).

Hutchings N, Cookson CJ, Hunter JJ, Kisilak ML, Liang Q, Bueno JM, Campbell MCW. (2006) Subjective Evaluation of Polarisation Images of the Optic Nerve Head and Retinal Structures. *Invest. Ophthalmol. Vis. Sci.*, 47, E-Abstract 4060 (poster).

Kain KC, Harrington MA, Tennyson S, Keystone JS. Imported Malaria: Prospective Analysis of Problems in Diagnosis and Management. *Clinical Infectious Diseases*, Vol. 27, No. 1, pg. 142-149 (1998).

Kuroda T, Fujikado T, Ninomiya S, Maeda N, Hirohara Y, Mihashi T. Effect of aging on Ocular light scatter and higher order aberrations. *J Refract Surg* 18:S598-602 (2002).

Lawrence C, Olson JA. Birefringent Hemozoin Identifies Malaria. *American Journal of Clinical Pathology* Vol. 86, No. 3, pg. 360-363 (1986).

Lowell J, Hunter A, Steel D, Basu A, Ryder R, Fletcher E, Kennedy L. Optic Nerve Head Segmentation. *IEEE Transactions on Medical Imaging* Vol. 23, No. 2, pg. 256-264 (2004).

Lu SY, Chipman RA. Interpretation of Mueller Matrices based on polar decomposition. J. Opt. Soc. Am. A. Vol. 13, No. 5, pg. 1106-1109 (1996).

Marieb EN. Human Anatomy and Physiology: Chapter 18 – Blood. 5th Ed. Pearson Education, Inc. (2001).

Maude RJ, Dondopr AM, Sayeed AA, Day NPJ, White NJ, Beare NAV. The eye in Cerebral Malaria: What Can it Teach Us? Trans. R. Soc. Trop. Med. Hyg. Vol. 103, No. 7, pg. 661-664 (2009).

McGready R, Brockman A, Cho T, Levesque MA, Tkachuk A, Meshnick SR, Nosten F. Haemozoin as a Marker of Placental Parasitization. Transactions of the Royal Society of Tropical Medicine and Hygiene Vol. 96, pg. 644-646 (2002).

Miura M, Elsner AE, Weber A, Cheney MC, Osako M, Usui M, Iwasaki T. Imaging Polarimetry in Central Serous Chorioretinopathy. American Journal of Ophthalmology Vol. 140, No. 6, pg. 1014-1019 (2005).

Nee SF. Error Analysis of Null Ellipsometry with Depolarization. Applied Optics, Vol. 38, pg. 5388-5398 (1999).

Oldenbourg R. & Mei, G. New polarized light microscope with precision universal compensator, J. Microsc. Vol. 180, pg. 140-147 (1995).

Padiál MM, Subirats M, Puente S, Lago M, Crespo S, Placios G, Baquero M. Sensitivity of Laser Light Depolarization Analysis for Detection of Malaria in Blood Samples. Journal of Medical Microbiology Vol. 54, pg 449-452 (2005).

Pedrotti LS, Pedrotti FL S.J. Optics and Vision. Upper Saddle River, New Jersey, USA. Prentice Hall (1998).

Pezzaniti JL, Chipman RA. Imaging Polarimeters for Optical Metrology. Proceedings of the Society of Photo-Optical Instrumentation Engineers (SPIE). Vol. 1317, pg. 280-294 (1990).

Poinar G. *Plasmodium dominicana* n. sp. (Plasmodiidae: Haemospororida) from Tertiary Dominican Amber. Systematic Parasitology. Vol. 61, pg. 47-52 (2005).

Quillen DA Common causes of vision loss in elderly patients. *Am Fam Physician* Vol. 60, pg. 99-108 (1999).

Romagosa C, Menendez C, Ismail MR, Quinto L, Ferrer B, Alonso PL, Ordi J. Polarisation Microscopy Increases the Sensitivity of Hemozoin and Plasmodium Detection in the Histological Assessment of Placental Malaria. *Acta Tropica* Vol. 90, pg. 277-284 (2004).

Simandjuntak RA, Suksmono AB, Mengko TLR, Sovani I. Development of computer-aided diagnosis system for early diabetic retinopathy based on micro aneurysms detection from retinal images. Enterprise networking and Computing in Healthcare Industry. HEALTHCOM 2005. Proceedings of 7th International Workshop on 23-25, pg. 364 - 367 (2005).

Semwogerere D, Weeks ER. Confocal Microscopy. *Encyclopedia of Biomaterials and Biomedical Engineering*, Taylor & Francis (2005).

Sullivan AD, Nyirenda T, Cullinan T, Taylor T, Lau A, Meshnick SR. Placental Haemozoin and Malaria in Pregnancy. *Placenta* Vol. 21, pg. 417-421 (2000).

Taylor TE, Fu WJ, Carr RA, Whiteen RO, Mueller JG, Fosiko NG, Lewallen S, Liomba NG, Molyneux ME. Differentiating the Pathologies of Cerebral Malaria by Postmortem Parasite Counts. *Nature Medicine*, Vol. 10, No. 2, pg. 143-145 (2004).

Twietmeyer KM, Chipman RA, Elsner AE, Zhao Y, and VanNasdale D. Mueller matrix retinal imager with optimized polarization conditions. *Optics Express*, Vol. 16, Issue 26, pp. 21339-21354 (2008).

van Blokland GJ, "Ellipsometry of the human retina in vivo: preservation of polarization," *J. Opt. Soc. Am. A* **2**, 72-75 (1985).

VanNasdale DA, Elsner AE, Kohne KD, Peabody TD, Malinovsky VE, Haggerty BP, Weber A, Clark CA. Foveal Localization in Non-exudative AMD Using Scanning Laser Polarimetry. *Optometry and Vision Science* Vol. 89, No. 5, pg. 667-677 (2012).

Vogel CR, Arathorn DW, Roorda A, and Parker A. Retinal motion estimation in adaptive optics scanning laser ophthalmoscopy, *Optics Express*, Vol. 14, Issue 2, pp. 487-497 *Optics Express*, Vol. 14, Issue 2, pp. 487-497 (2006).

Weatherall DJ, Miller LH, Baruch DI, Marsh K, Doumbo OK, Casals-Pascual C, Roberts DJ. Malaria and the Red Cell. American Society of Hematology, pg. 35-57 (2002).

Webb RH, Hughes GW, Delori FC. Confocal Scanning Laser Ophthalmoscope. Applied Optics Vol. 26, No. 8 (1987).

Webb RH, Hughes GW. Scanning laser ophthalmoscope. IEEE Transactions on Biomedical Engineering 28: 488-492 (1981).

R. N. Weinreb , “Scanning laser polarimetry to measure the nerve fiber layer of normal and glaucomatous eyes,” Am. J. Ophthalmol. 119, 627-636 (1995).

White VA, Lewallen S, Beare NAV, Molyneux ME, Taylor TE. Retinal Pathology of Pediatric Cerebral Malaria in Malawi. PLoS ONE Vol. 4, No. 1, e4317.doi:10.1371/journal.pone.0004317 (2009).

White VA, Lewallen S, Beare NAV, Kayira K, Carr RA, Taylor TE. Correlation of Retinal Haemorrhages with Brain Haemorrhages in Children Dying of Cerebral Malaria in Malawi. Transactions of the Royal Society of Tropical Medicine and Hygiene Vol. 95, pg. 618-621 (2001).

Wilson BC, Damaskinos S, Hedley DW, Nicklee T, Constantinou P. A High-Resolution MACROscope With Differential Phase Contrast, Transmitted Light, Confocal Fluorescence, and Hyperspectral Capabilities for Large-Area Tissue Imaging. IEEE Journal of Selected Topics in Quantum Electronics, Vol. 11, No. 4 (2005).

Wilson BK, Behrend MR, Horning MP, Hegg MC. Detection of Malarial Byproduct Hemozoin Utilizing its Unique Scattering Properties. Optics Express, Vol. 19, No. 13, pg. 12190-12196 (2011).

Wood BR, Hermelink A, Lasch P, Bambery KR, Webster GT, Khiavi MA, Cooke BM, Deed S, Naumann D, McNaughton D. Resonance Raman Microscopy in Combination with Partial Dark-field Microscopy Lights up a New Path in Malaria Diagnostics. Analyst Vol. 134, pg. 1119-1125 (2009).

Zheng J, Tian J, Deng K, Dai X, Zhang X, Xu M. Salient Feature Region: A New Method for Retinal Image Registration. IEEE Transactions on Information Technology in Biomedicine, Vol. 15, No. 2, (2011).